Universitat Autònoma de Barcelona

Array of microfluidic beam resonators for mass sensing applications - Design, Fabrication and Testing

Salomón Elieser Marquez Villalobos

Universitat Autònoma de Barcelona

Doctorat en Enginyeria Electrònica

Departament D'Enginyeria Electrònica

Array of microfluidic beam resonators for mass sensing applications - Design, Fabrication and Testing

Doctoral Thesis – July 2016

Salomón Elieser Marquez Villalobos
Author

Prof. Laura M. Lechuga Gómez
Director

Dr. Mar Álvarez Sánchez
Co-director

Dr. David Jiménez Jiménez
Tutor

CSIC
Consejo Superior de Investigaciones Científicas

ICN2
Institut Català de Nanociència i Nanotecnologia
Excelencia Severo Ochoa

Abstract

In the pursuit of more efficient diagnosis tools, micro- and nanomechanical biosensors have shown promising impact due to its high sensitivity, fast interaction and small size. Under this premise, the present Doctoral Thesis has the ultimate objective of integrating a mass sensor based on Micro-Electro-Mechanical Systems (MEMS) resonators into a Lab-on-a-Chip platform for the simultaneous detection of different analytes in real-time. The sensor technology follows the idea of fabricating microfluidic channels into doubly clamped microbeam resonators, namely Hollowed Microbeam (HMB), to enhance the sensitivity and to reduce damping and viscous drag produced by the surrounding media. The microresonators are consecutively arranged with reduced separation distances and slightly variations on their effective lengths to display extremely close resonant frequency peaks. In this way, each HMB resonator will enable the detection of a specific analyte flowing through its inner microchannel with a frequency response that can be differentiated from the remaining resonating elements.

The first part of the Thesis includes a theoretical analysis of the mechanical and microfluidic behaviour of the hollowed microstructures in an array configuration when different dimensions and structural materials come into play. Finite element simulations (FEM) in Comsol Multiphysics have been employed to: i) validate and complement the theoretical analysis, ii) investigate the fluid-structure interaction of the HMB devices and iii) evaluate two filling configurations (in-line and H-shaped) for the suitable exchange of fluids inside the microchannels. Once the design was optimized, three microfabrication schemes were developed at cleanroom facilities including bulk and surface micromachining processes and implementing a three layer sandwich approach by which a sacrificial layer was embedded into two structural layers. The first generation of HMB devices produced silicon nitride structures with coupled resonant frequencies due to an over-etching effect. Although this fabrication did not build hollowed resonators, this approach provided new insights for mass sensing applications through the study of highly localized vibration modes displayed on those arrays of coupled resonators. On the other hand, the second scheme successfully fabricated hollowed polycrystalline silicon structures. With the integration of high aspect ratio polymer-based microchannels, the HMB devices measured the mass density and viscosity of different sample solutions and alcoholic drinks demonstrating a mass responsivity of 7.4 Hz/pg and a viscosity range between 1 cP to 2.6 cP with a resolution of 0.15 cP. Finally, the third fabrication dealt with incorporating on-chip polymer microfluidic channels using lamination techniques. Also, the polysilicon structural layer of the resonators was oxidized to improve the hydrophilic properties of the microchannels.

The characterization of the HMB devices was performed by an optical readout interferometer for automatically capturing the out-of-plane movement of the resonators with a displacement sensitivity of $0.12\ \mathrm{pm}/\sqrt{Hz}$. Also, the devices were actuated through a sweep frequency methodology enhancing the Q-factor and thus the frequency resolution of the system using a piezoceramic crystal.

Resumen

En la búsqueda de herramientas de diagnóstico más eficientes, los dispositivos biosensores basados en resonadores micro y nanoelectromecánicos han demostrado un gran impacto en este ámbito debido a su alta sensibilidad, tamaño miniaturizado y su rápida respuesta a una interacción. Bajo esta premisa, el presente trabajo de Tesis doctoral tiene como objetivo principal integrar un microsensor de masa basado en dispositivos microelectromecánicos en una platarforma Lab-on-a-Chip para la detección simultánea y en tiempo real de diferentes analitos. La tecnología del sensor se sustenta en la idea de fabricar canales de microfluídica en resonadores micromecánicos tipo puente, denominados dispositivos HMB (del acrónimo Hollowed Microbeam) para mejorar la sensibilidad del dispositivo y reducir el efecto de amortiguamiento y resistencia de la viscosidad del medio. Los microresonadores están colocados consecutivamente con reducidas distancias de separación y con ligeras variaciones en sus longitudes efectivas para mostrar picos de frecuencias de resonancia muy próximos. De esta forma, cada resonador HMB permitirá la detección de un analito específico mientras este es transportado a través del canal de microfluídica al mostrar una frecuencia de resonancia fácilmente diferenciable del resto de los resonadores. La primer parte de esta Tesis doctoral se ha centrado en un análisis teórico del comportamiento mecánico y fluídico de un array de micropuentes huecos considerando diferentes dimensiones y materiales structurales. Se han empleado simulaciones de elemento finito (FEM) en el programa multifísico Comsol para: i) validar y complementar el análisis teórico, ii) investigar la interacción fluído-estructura de los dispositivos HMB y iii) evaluar dos configuraciones de llenado (en línea y forma H) para el adecuado intercambio de líquidos dentro de las cavidades. Una vez que el diseño es optimizado, se desarrollaron tres esquemas de microfabricación en instalaciones de Sala Blanca incluyendo tanto procesos superficiales y a nivel de sustrato, como una aproximación tipo sándwich, la cual integra una capa sacrificial entre dos capas estructurales. La primera generación de dispositivos HMB produjo estructuras de nitruro de silicio con frecuencias de resonancia acopladas debido a un efecto de sobreataque. Aunque no se consiguieron estructuras huecas, esta aproximación proporcionó nuevos conocimientos útiles para aplicaciones de sensado de masa mediante el estudio de modos de vibración altamente localizados en algunas configuraciones acopladas de micropuentes. Por otra parte, la segunda fabricación permitió alcanzar exitosamente estructuras de polisilicio huecas. Con la integración de canales de polímero de elevada relación de aspecto, la densidad y viscosidad de varias soluciones así como de bebidas alcohólicas fueron evaluadas, mostrando una respuesta en masa de 7.4 Hz/pg en un rango de viscosidades entre 1 cP y 2.6 cP con una resolución de 0.15 cP. Finalmente con la tercera fabricación se trató de mejorar la integración de canales de polímero a nivel de oblea usando técnicas de laminado. Asimismo, la capa estructural de polisilicio fue oxidada para mejorar la mojabilidad de los microcanales. La caracterización de los dispositivos HMB se realizó ópticamente mediante un interferómetro para la adquisición automática de la respuesta de cada resonador con una sensibilidad de 0.12 $\mathrm{pm}/\sqrt{Hz}$. Además, los resonadores fueron excitados por medio de un barrido en frecuencias usando un transductor piezocerámico para mejorar el factor de calidad y, por tanto, la resolución en frecuencia del sensor.

Acknowledgments

Table of contents

Abstract ..... **i**

Resumen ..... **iii**

Acknowledgments ..... **iv**

Table of contents ..... **v**

Motivation and Objectives ..... **xi**

Thesis structure ..... **xiii**

Chapter 1 Introduction **1**

1.1 How MEMS devices are manufactured? 4

1.2 How MEMS devices are detected and actuated? 10

1.3 Suspended Microchannel Resonators 12

1.4 Array of Hollowed Microbeams Resonators 18

References **21**

Chapter 2 Design and Simulation of HMB devices **29**

2.1 Physics and dynamic mode response of vibrating structures 30

2.1.1 Resonant frequency 30

2.1.2 Quality factor 33

2.2 Physics and dynamic mode response of HMB devices 34

2.2.1 Resonant properties 34

2.2.2 Quality factor 35

2.2.3 Mass responsivity 36

2.2.4 Proposed design of the device 38

2.3 Mechanical simulations of HMB devices 42

2.3.1 Eigenfrequency analysis 42

2.3.2 Calculation of the spring constant 45

2.3.3 Calculation of the mass responsivity 46

2.3.4 Sweep mode analysis 47

2.4 Microfluidic simulations of HMB devices 51

2.4.1 Theory 51
2.4.2 Stationary study of microchannels 52
2.4.3 Fluid-structure interaction analysis 55
2.4.4 Filling study of microchannels 58
2.5 General conclusions about the design of the HMB devices 75
References 77
Chapter 3 Fabrication of HMB devices 79
3.1 Fabrication process of HMB devices of the first generation 80
3.1.1 Mask design 80
3.1.2 Fabrication process at cleanroom facilities 83
3.1.3 General overview and evaluation of the fabrication process 90
3.2 Fabrication process of HMB devices of the second generation 93
3.2.1 General overview and evaluation of the fabrication process 100
3.2.2 Oxidation schemes 102
3.3 Fabrication process of HMB devices of the third generation 111
3.3.1 Mask design 111
3.3.2 Fabrication process at cleanroom facilities 117
3.3.3 Fluidic integration with polymers 127
3.3.4 Bulk micromachining of devices 130
3.3.5 General overview and evaluation of the fabrication process 139
References 141
Chapter 4 Chip packaging and optical readout 143
4.1 Fluid delivery system integration: polymer-based bonding strategies 144
4.1.1 PDMS packaging 146
4.1.2 SU-8 based packaging 151
4.2 Experimental setup implementation 153
4.2.1 Chip packaging: electrical and microfluidic interconnections 153
4.2.2 Interferometric readout 157
4.2.3 Actuation and acquisition schemes 159
4.2.4 Signal processing and graphical user interface 162
4.2.5 Noise analysis and responsivity of the experimental setup 164

References **167**

Chapter 5 Results and discussion **169**

5.1 Characterization of 1st generation of HMB devices 169

5.1.1 Resonant frequency and Q-factor of uncoupled devices 170

5.1.2 Mechanically coupled devices 173

5.2 Characterization of 2nd generation of HMB devices 187

5.2.1 Filling of embedded microchannels 187

5.2.2 Resonant frequency and Q-factor 190

5.2.3 Density and viscosity evaluation of alcoholic drinks 197

5.3 Characterization of 3rd generation of HMB devices 199

References **202**

Chapter 6 Conclusions and Future Perspectives **203**

Annex 1 ..... **207**

Annex 2 ..... **209**

Abbreviations and Acronyms

µ-TAS	Micro Total Analysis Systems
ABV	Alcohol By Volume
AFM	Atomic Force Microscope
BHF	Buffered Hydrogen Fluoride
BioMEMS	Biomedical Micro-Electro-Mechanical Systems
BW	Bandwidth
CAD	Computer-Aided design
CCD	Charge Coupled Device
CMOS	Complementary Metal-Oxide-Semiconductor
CNC	Computer Numerical Control
DAE	Defreckling Aluminum Etchant
DNA	Deoxyribonucleic acid
DRIE	Deep Reactive Ion Etching
EBV	Electron Beam Evaporation
FEM	Finite Element Modelling
FFT	Fast Fourier Transform
HMB	Hollow Microbeam
HPLC	High-Performance Liquid Chromatography
KOH	Potassium hydroxide
LIGA	Lithographie, Galvanoformung, Abformung
LOD	Limit of Detection
LPCVD	Low Pressure Chemical Vapour Deposition
MEMS	Micro-Electro-Mechanical Systems
MFS	Minimum Feature Size

NEMS	Nano-Electro-Mechanical Systems
NEP	Noise Equivalent Power
PDMS	Polydimethylsiloxane
PEB	Post-Exposure Bake
PECVD	Plasma Enhanced Chemical Vapour Deposition
PEEK	Polyether Ether Ketone
PET	Polyester
PGMEA	Propylene Glycol Methyl Ether Acetate
PMMA	Polymethyl-methacrylate
POC	Point of Care
PSD	Position Sensitive Detector
PSG	Phosphorous Silicate Glass
QCM	Quartz Crystal Microbalance
RF	Radio Frequency
RIE	Reactive Ion Etching
SDS	Sodium Dodecyl Sulfate
SEM	Scanning electron Microscope
SLA	Stereolithography
SMR	Suspended Microchannel Resonator
SNR	Suspended Nanochannel Resonator
SPM	Scanning Probe Microscopy
SPR	Surface Plasmon Resonance
TEOS	Tetraethyl Orthosilicate
TFDS	Thick Film Dry Sheets
TMAH	Tetramethylammonium hydroxide
UV	Ultraviolet light

Publications and Conference contributions

[1] D. Fariña, M. Álvarez, S. Márquez, C. Domínguez, and L. M. Lechuga, 'Sensitivity analysis for improving nanomechanical photonic transducers biosensors', J. Phys. Appl. Phys., vol. 48, no. 33, p. 335401, 2015.

[2] S. Márquez, M. Álvarez, D. Fariña, C. Domínguez, and L. M. Lechuga, 'Simulation and characterization of hollow microbridge resonators for label-free biosensing', Proc. SPIE, Bio-MEMS and Medical Microdevices II, vol. 9518, 2015

[3] D. Fariña, M. Álvarez, S. Márquez, C. Domínguez, and L. M. Lechuga, 'Out-of-plane single-mode photonic microcantilevers for integrated nanomechanical sensing platform', Sens. Actuators B Chem., vol. 232, pp. 60–67, 2016.

[4] S. Márquez, M. Álvarez, D. Fariña, A Homs-Corbera, C. Domínguez and L.M Lechuga, 'Array of microfluidic beam resonators for density and viscosity analysis of liquid phase analytes', *Submitted to Sens. Actuators B*, 2016

[5] V. Solís-Tinoco, S. Márquez, B. Sepúlveda and L.M Lechuga, 'Fabrication of well-ordered silicon nanopillars embedded in a microchannel via metal-assisted chemical etching: A route towards an opto-mechanical biosensor', *Submitted to RSC Advances,* 2016.

[6] S. Márquez, M. Álvarez, J.A. Plaza, C. Domínguez and L.M Lechuga, 'Effect of the coupling strength of a mistuned array of coupled resonators for mass sensing', [*In preparation*].

[7] S. Márquez, M. Álvarez, D. Fariña, C. Domínguez, and L.M. Lechuga, 'Array of microbridge resonators for the development of BioMEMS platforms', VI Int. Conf. Surf. Mater. Vac. Mérida, México, Septiembre 2013.

[8] S. Márquez, M. Álvarez, D. Fariña, C. Domínguez, and L. M. Lechuga, 'Towards a biosensing multiple platform based on an array of hollow microbridge resonators', IEEE SENSORS 2014 Proceedings, pp. 329–331, 2014.

Motivation and Objectives

The emerging need for having highly sensitive diagnostic methods and reliable detection technologies has led to the development of alternative tools and solutions, as is the case of biosensor devices. Biosensor devices represent an ideal analytical tool able to provide more reliable and effective diagnosis compared with current techniques and monitoring tools due to their high sensitivity, specificity, miniaturization, relatively low cost and easy handling. However, a major drawback of biosensor devices is the ability to detect multiple analytes simultaneously, mainly related to the complexity in the number of required sensors along with a microfluidic subsystem for fluid sample delivery and a robust electronic instrumentation for data acquisition of the entire system.

Micro- and nanoelectromechanical resonators have become one of the most promising tools for the development of high sensitive and multiplexed biosensors. The main reasons are related to their miniature size, low mass, fast response, and their suitability for integration in Lab-on-a-Chip platforms at low cost. However, in spite of their demonstrated high sensitivity, biosensors based on mechanical resonators still present several limitations that need to be solved before achieving an easy to use and competitive multiplexed biosensor device. Explicitly, when a mechanical sensor is immersed in a fluid environment, which commonly happens while evaluating biological samples, the sensitivity of the sensor is degraded and thus, a rapid dissipation of energy occurs due to the overdamped response of the resonator. A few years ago, an innovative approach was proposed to solve the above limitation by integrating a fluidic channel into a suspended microchannel resonator.

Since micro- and nanoscale resonators with embedded microchannels emerged as an alternative label-free method respect to other mass sensing methodologies as are the Surface Plasmon Resonance (SPR) or the Quartz Crystal Microbalance (QCM), this technology has shown promising advances in mass spectrometry. Recent breakthroughs involve a wide range of applications to characterize biomolecular signatures and nanoparticles in solution, particularly in the biological field. However, the developed technology has been focused on increasing the sensitivity of the devices by downscaling their dimensions. While a single device is eligible for identification of individual reagents with high sensitivity, a device approach that includes an array of embedded microchannels can enable the detection of multiple analytes in solution and can enhance the statistics of the measurement in a single run reducing analysis time. In this regard, optical read-out schemes are good candidates because of their demonstrated high sensitivity and broadband operation looking for detecting, in a simultaneous way, the overall response of the set of resonators.

Henceforth, the development of a biosensor platform based on an array of nanomechanical sensors with embedded microchannels will have a strong potential impact for elaborating more efficient diagnosis tools. This can have important implications for providing real-time monitoring of chemomechanical processes with low volume consumption and with high feasibility to handle more than one single agent without requiring large or expensive electronic instrumentation.

Under this assumption, this Thesis work is primarily focused on developing a novel technology based on an array of hollowed MEMS resonators with the final scope of integrating a Lab-on-a-chip platform for the efficient and simultaneous detection of different analytes in solution in real-time. The project will technologically explore the feasibility and compatibility to build these complex mechanical structures employing materials commonly used for the fabrication of MEMS devices, as is polycrystalline silicon and doped silicon oxide, to fully integrate a functional array of suspended microchannels with on-chip microfluidics. The particular objectives of the project are detailed as follows:

- To perform a theoretical study of the physics and microfluidics for a doubly clamped beam resonator with embedded microchannel in an array configuration.
- To compute finite element simulations (FEM) to analyse the structural mechanics and microfluidic behaviour of the proposed technology since the morphology and topology of the microchannels present subtle variations in their dimensions.
- To establish a robust fabrication methodology using polycrystalline silicon and silicon nitride as structural materials and to analyse their compatibility with standard surface and bulk micromachining.
- To explore new packaging methodologies that allow the integration of on-chip microfluidics using polymer-based structures.
- To search for optical transduction methodologies with high sensitivity for detecting nanoscale displacements and with the capacity to measure an array of resonators simultaneously.
- To investigate the feasibility to fill channels with micro-scale dimensions regarding their structural material and fluidic properties.
- To investigate the capability of the sensors to monitor and track mass density and viscosity changes while transporting different fluidic samples.

Thesis structure

The content of this thesis is outlined as follows:

Chapter 1 - Introduction. This chapter describes the principal motivation to develop the Ph.D. research project. It provides a description of the state-of-the-art and the technological background that supports the implementation of hollow micromechanical resonators for mass sensing applications. It also describes both the general and particular objectives aiming to the design, simulation, fabrication, characterization and application of the proposed technology.

Chapter 2 - Design and Simulation of HMB devices. This chapter studies the governing physics and microfluidic behaviour of the HMB devices. By using the Euler-Bernoulli beam theory, the frequency response of the resonators in respect of their dimensions is provided. Also, finite element simulations (FEM) are performed to extend the analytical theory knowledge on the specific design and dimensions of the HMB devices. In this way, sweep mode analyses explain the interplay between the height, width, and length of the devices to determine their elastic constant, frequency of operation in vacuum and mass responsivity. In the second part of this chapter, an exhaustive study of the governing microfluidics inside the embedded microchannels is computed through FEM. Under this rationale, the effects of the hydrostatic pressure over the microchannel walls are addressed. Finally, several fluid filling schemes are studied to grant complete fluid exchange inside the resonators.

Chapter 3 - Fabrication of HMB devices. This chapter is one of the main pieces of the Thesis as it reports three fabrication schemes carried out in the clean room facilities. The first approach consists of fabricating the first generation of HMB devices using silicon nitride and doped silicon oxide as structural and sacrificial materials, respectively. This methodology provides a general overview of the main constraints involved in the fabrication process, studies the feasibility to obtain operational devices and estimates the time to end of a fabrication process based on the proposed steps. Afterwards, a second fabrication scheme is proposed, but polycrystalline silicon and doped silicon oxide are employed as main materials to integrate the second generation of HMB devices. Finally, the last fabrication approach includes the experience acquired to integrate polymer-based microfluidics into a new design of the third generation of HMB devices. Furthermore, an oxidation process is carried out to improve the hydrophilic properties of the microchannels facilitating their filling.

Chapter 4 - Chip packaging. This part of the thesis deals with two main tasks: implementation of a fluid delivery system and chip packaging, and construction of the experimental setup to acquire the response of the sensors. The first section reports on two strategies using polymers to integrate fluid delivery microchannels with the second generation of HMB devices to grand fluid exchange inside the resonators. As follows, two methodologies are presented to assemble the electrical and microfluidic interconnections aiming to control the temperature of the system, drive the resonators acoustically and perform vacuum extraction. The second main task corresponds to the optical

readout setup, which consists of a Michelson interferometer system eligible for detecting small displacements in the out-of-plane of micro- and nanoscale structures. Also, a sweep frequency methodology is applied to drive into resonance the response of the devices. Collected data is acquired and processed using a Labview interface.

Chapter 5 - Results and discussion. In this section, the characterization of fabricated devices from the first, second and third generation is experimentally performed. First, the performance of the first generation of devices is outlined demonstrating the capabilities of the experimental setup to detect the frequency response of the resonators. Explanation and advice are provided for silicon nitride resonators that yielded a coupled response caused by the undercut effect during the fabrication process. FEM simulations support these outcomes. As follows, the ability to transport fluids inside the second generation of devices is studied using the two polymer-based microfluidic approaches presented in the previous chapter. After that, the capability for detecting other types of samples such as different solvents, organic solutions, and also commercially alcoholic beverages is demonstrated; density and viscosity measurements in a flow-through detection mode support the proof of concept of the devices. Finally, a discussion regarding the third generation of devices is introduced addressing the trade-offs and compatibility when integrating on-chip microfluidics during fabrication procedures.

Chapter 6 - Conclusions and Future Perspectives. This chapter enumerates the overall conclusions of the thesis project along with the perspectives and future related work.

Chapter 1 Introduction

Through the history, humankind has invested considerable efforts in trying to know and understand quantitatively the physical world. The necessity to measure emerged as a valuable tool for determining intrinsic properties associated with a particular object or any physical phenomena. Weighing scales are a good example of this need. During the unfolding of commerce in the antiquity, merchants needed a way to estimate the value of goods instead of simply trading or counting them by pieces. For instance, the most ancient relics of weighing scales, which date back to 2000 B.C., used a balance to compare the weight of two objects simply until equilibrium was reached. In the 17th century, Archimedes came up with a new method to recognize the purity of gold. The word "Eureka" (from heuriskein 'find') was articulated thanks to the successful determination of the density of gold based on the calculation of the volume and weight of irregular shaped objects. Henceforth, the capability to measure a physical property of a given material yielded new insights to determine its nature and value regarding other materials.

To date, recent advances in scientific research and engineering have contributed to the knowledge and interpretation of physical variables such as mass, force, displacement, time, temperature and pressure among others, through the development of sensor devices. A sensor is an element that transduces a form of energy into another energy domain, commonly the electrical one. For instance, state-of-the-art mobile phones include a whole range of sensors that enable the detection of weather conditions, provide localization, monitor vital signs and even can be used as microscope devices. The broad category of sensors is associated with a transduction principle, which can be chemical, optical, physical, and mechanical. In this way, sensors that include movable parts, known as **mechanical sensors**, have expanded the possibility to quantify and characterize small quantities of matter beyond the most traditional sensing methods.

Similarly, actual breakthroughs in the technology and fabrication processes have enabled the miniaturization of macro-scale mechanical sensors, which is of interest to many scientific fields. As much as the size of the sensor device can be reduced, the better performance in sensitivity will be displayed because the sensor will match directly to the dimensions of the physical variable in question, allowing faster interaction, less energy consumption and also less influence to external vibrations. For example, single cells are very sensitive entities, and thus sensors with nanoscale parts can be used to interrogate new findings of their interaction with the surrounded media. Besides, the fabrication cost will be obviously reduced when devices with smaller elements are involved, which facilitates their manufacturability in batch processes. The technological field specialized in the manufacture and operation of small objects that include movable parts of micro-

scale dimensions is named MEMS; the acronym MEMS stands for Micro-Electro-Mechanical Systems. MEMS devices have produced a pronounced impact in many disciplines and emerging technologies present in our daily life including inkjet printing, microphones, ultrasonic transducers, accelerometers for electronic control and automotive air-bag systems, automatic control of drones using gyroscopes, energy harvesting devices, and pressure sensors to mention a few of them, as depicted in

Fig. 1–1. Microscale technology has also dramatically pushed the knowledge of the biology of organs through the discovering of compatible biomaterials and microfabrication strategies attempting to have a better control of cell environments and use smaller assays for tissue engineering [1].

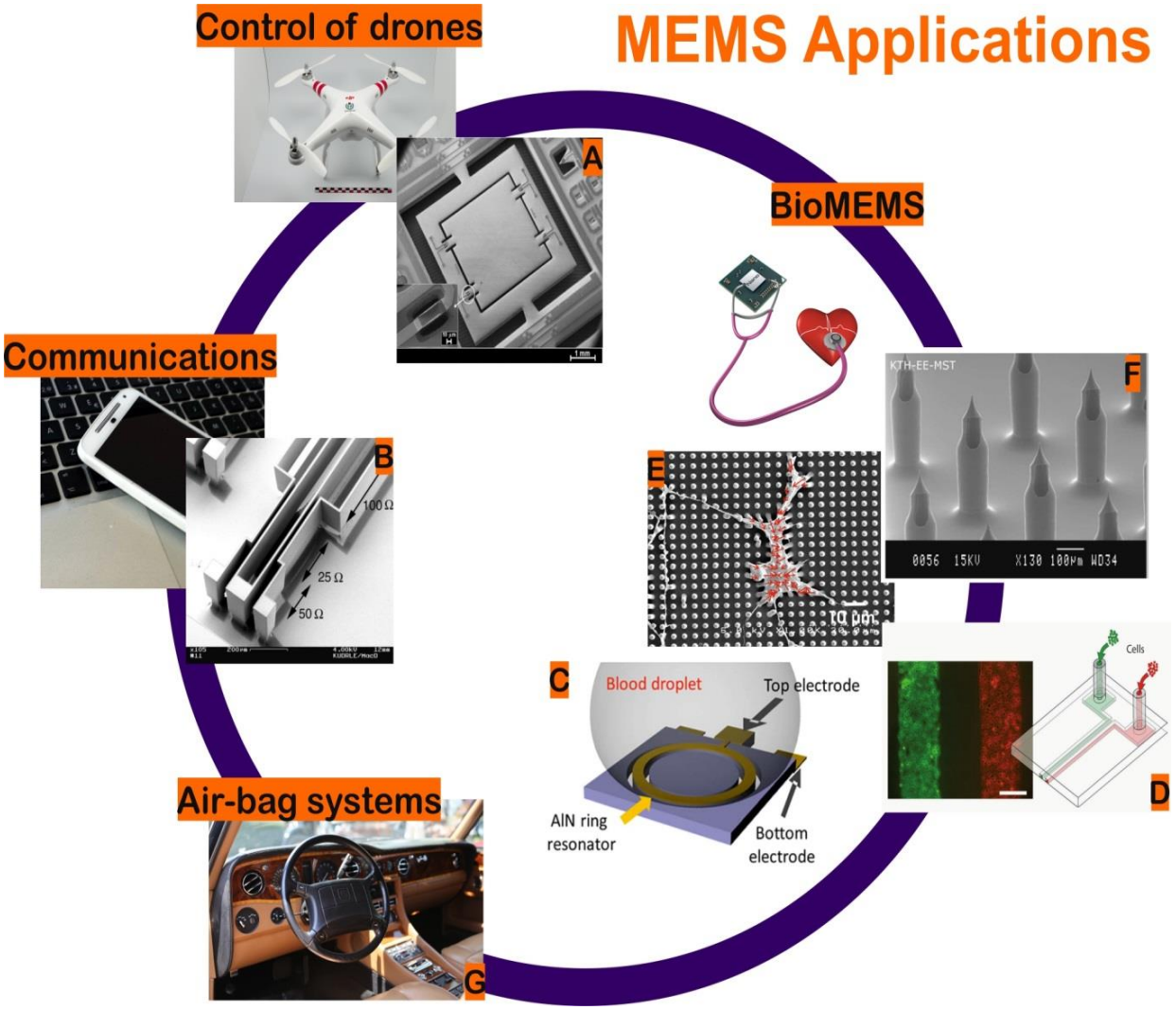

Fig. 1–1. Some of the broad applications of MEMS devices include: A) accelerometers for inertial force detection in controlled systems and robotics [2], B) wave phase shifters employed in RF communications and information technology [3], C) real-time monitoring of whole blood coagulation [4], D) biological applications using microfluidic devices [5], E) study of cellular

microforces [6], F) drug delivery and screening using microneedles [7] and even in G) automotive air-bag systems.

Particularly, one sector that has benefited owing to device miniaturization corresponds to mass sensing applications using MEMS resonators. Micro and nanomechanical resonators have quantified the mass of single particles attaining detection limits down to individual atoms due to their high sensitivity. For example, unprecedented mass measurements have been achieved using carbon nanowires with yoctogram mass resolution ($10^{-24}g$) enabling the detection of interactions at atomic level [8]. Nanomechanical technology has proven effectiveness for spectrometry of biological entities such as viruses [9] and even for detection of cancer biomarkers in serum [10]. Besides, mechanical resonators have found favourably scope for mass detection of gases [11], and viscosity and density estimation of fluids [12]–[14]. The most commonly used mechanical element to quantify these mass measurements has been the cantilever, which is a beam with micro- or nanoscale dimensions attached to a single end, as Fig. 1–2 shows. Generally, the transduction principle is based on measuring the resonance frequency of the beam when a mass load is attached to its surface, and so, the interrogated analyte is characterized in terms of the variations of the beam's frequency. The work of this thesis follows this baseline by fabricating novel mechanical microresonators for mass sensing applications.

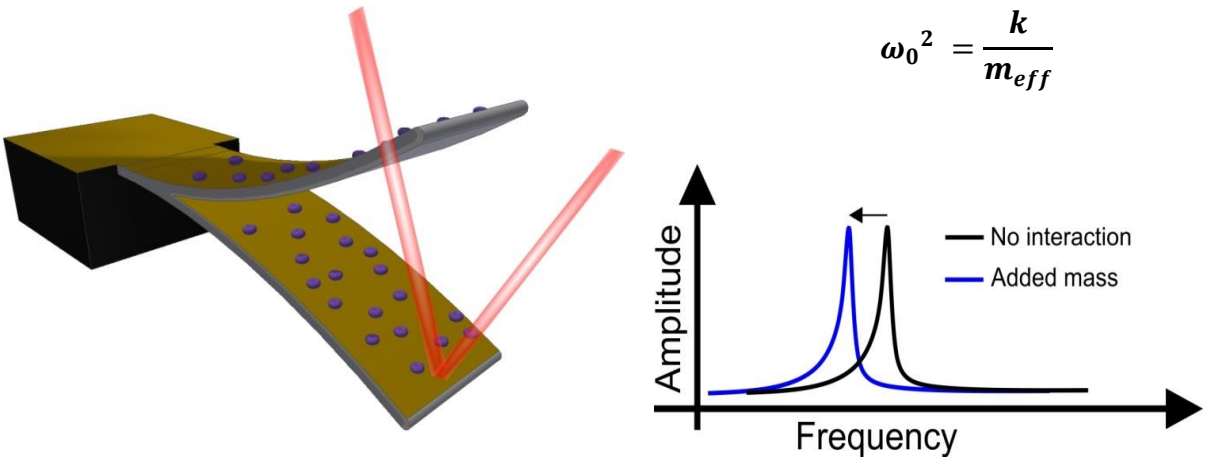

Fig. 1–2. Mass sensing principle using a single clamped beam (microcantilever) based on the dynamic operational mode in which the mass of the sample is interrogated regarding the resonant frequency response of the beam. The transduction principle is an optical-based detection method.

At the same time, the density and rheological parameters of fluids, such as viscosity, have been other sub-classes for mass sensing applications with outstanding progress. Rheological settings of fluids have been fundamental not only in the evaluation of physical properties of fluidic samples but also in ascertaining the composition of low concentrated analytes in a myriad of industrial and medical applications. Some of the conventional methods and sensors for determining viscosity and density of fluids include resonating tubes [15], tuning fork tubes [16], [17], U-shaped tubes [18] and surface acoustic waves devices [19]. Nevertheless, these methodologies require large volume

samples, need long evaluation times and have limited sensitivity range. Henceforth, MEMS devices have become one of the most promising tools for the development of high sensitive rheological sensors due to their miniature size, low mass, and high suitability for integration in CMOS (complementary metal-oxide semiconductor) technologies. The scope of applications of MEMS devices in this field includes detection of DNA in solutions [20], viscoelastic properties of blood and plasma coagulation [21], [22], viscosity measurements of hydrocarbons, silicon oils, oil/fuel mixtures [23]–[25] and gases [26], characterization of polymer solutions [27], concentration of sugar mixtures [28] and ethanol solutions [29], [30], among others.

Likewise, the interrelation of MEMS devices with other fields, such as microfluidics, has actively encouraged the development of novel biosensor platforms with the capability to acquire, analyse, process and interpret biomolecular interactions in biology and medicine. As a result, new technological and research fields have been incorporated, as is the case of BioMEMS, Micro Total Analysis Systems (μTAS), Lab-on-a-Chip devices and lately, Point-of-Care devices (POC). These eminent biosensor platforms aim to revolutionize large and expensive analytical systems into something that may fit in the palm of one's hand to provide a fast diagnostic with respect to conventional lab tests. Consequently, biosensor devices based on mechanical sensors have pushed the development of new methodologies for drug screening [31], cell biology and molecular study [6], [32], quantification of nanoparticles in solution [33], detection of protein biomarkers in blood [10],[34] and, identification of reagents and molecular signatures [35]–[38] to mention a few of them, with the purpose of granting early diagnosis of diseases, and thus for improving the human health care.

1.1 How MEMS devices are manufactured?

When the MEMS technology emerged, the first devices utilized silicon as based substrate because of its electrical and thermal throughput properties and crystallographic orientation. Since the materials and strategies used in CMOS technology are compatible with MEMS, the manufacturability of this microscale technology can be accomplished by integrating additive and subtractive processes to remove amounts of materials precisely in the form of layers on the surface of a silicon wafer [39]. Under this assumption, the fabrication of MEMS devices based on silicon technology involves specific step-by-step tasks including two main types of processes: bulk and surface micromachining.

Bulk micromachining focuses on manufacturing the based substrate to build up microstructures. Usually, the desired microstructure pattern is transferred into the substrate by photolithography while the pattern is defined by etching processes in the substrate. The photolithography is an optical technique that stamps a 2D design printed on a quartz crystal photomask by means of UV light exposition into a photosensitive resist deposited onto the silicon substrate. Once the photoresist is chemically modified and removed with a developer agent to undercover those areas on the substrate to be manufactured, the exposed material can be removed with dry or wet etching methods. The

most commonly known dry etching process is the reactive ion etching (RIE), which selectively removes the exposed material by the action of ion bombardment. If however, a wet etching step is carried out, the whole substrate is immersed in an etchant solution to eliminate those materials with poor selectivity to the etchant solution. Depending on the crystallographic properties of the substrate, two categories of wet etching processes can be employed: isotropic and anisotropic. Moreover, the appropriate selection of the material is paramount to achieve a high yield of microstructures with well-defined dimensions. Typical materials employed as protective masks include photoresists, silicon oxide and silicon nitride depending on the ongoing etching procedure.

Surface micromachining follows sequential fabrication steps on the substrate surface. Conventionally, the microstructures are made using a combination of a sacrificial and structural material. For that, thin-films of both materials are consecutively deposited to constitute a three-layer sandwich structure that alternates between the structural and sacrificial materials. Afterwards, using photolithography and dry etching processes the microstructures are patterned. For either obtaining released or hollowed microscale structures, the embedded sacrificial layer is usually removed by wet etching.

Another important step in MEMS micromachining involves the packaging of devices whenever protection from external noise sources, moisture or vacuum extraction is required to improve the response and performance of the devices. Packaging is highly recommended, for example, in accelerometers and gyroscopes chips that usually operate under vacuum conditions or in microstructures with high aspect ratios, which are highly susceptible to external vibrations. MEMS packaging is carried out at wafer-level commonly using three bonding strategies: by directly fusing a silicon wafer to the based substrate, by anodic soldering of a glass wafer or by using an intermediate layer between both parts using silk-screen printing, for example.

Fig. 1–3a shows a microfabrication approach that combines both surface and bulk micromachining to build suspended microchannel resonators. The main surface micromachining processes include: i) composition of a three-layer microchannel that confines a polycrystalline silicon sacrificial layer into a silicon nitride structure by subsequent thin-film coating, ii) isotropic wet etching of the polycrystalline silicon sacrificial layer with KOH solution and iii) definition of the fluidic inlets and outlets to match the effective dimensions of the resonators. In here, the isotropic wet etching has proven useful for etching long microchannels with lengths up to 1 mm. Meanwhile, the bulk micromachining processes incorporate iv) burying the microchannel into the substrate using RIE and v) releasing the resonator from the silicon substrate and defining access through holes for liquid injection into the microchannels by an anisotropic wet etching. The KOH solution preferably etches the silicon material at higher etching ratios for the crystallographic planes (100) and (110), but the plane (111) is instead etched more slowly, see Fig. 1–3a-b. In this way, the integrity of the design is preserved avoiding undercut of the resonators. Finally, using an intermediate layer and a glass frit bonding strategy, the packaging of the resonators is implemented.

On the other hand, MEMS devices with high aspect ratios can be fabricated by other procedures that include UV-LIGA technology, deep RIE processes in silicon [40], soft lithography [41], [42], CNC micromachining [43] and laser writing [44]. Among them, UV-LIGA technology is a non-

silicon based microfabrication technique eligible for creating high aspect ratio microstructures from a few microns to several millimeters with high-resolution. The strategy employs an x-ray radiation from a synchrotron source to constitute well-defined microstructures with vertical sidewalls. The high-penetration deep of the x-rays reduces diffractions effects and facilitates the fabrication of complex 3D patterns using long working distances [45]. The fabrication technique consists of spinning an photosensitive x-ray resin, commonly polymethyl-methacrylate (PMMA), yet SU-8 is also compatible, onto a conductive substrate.

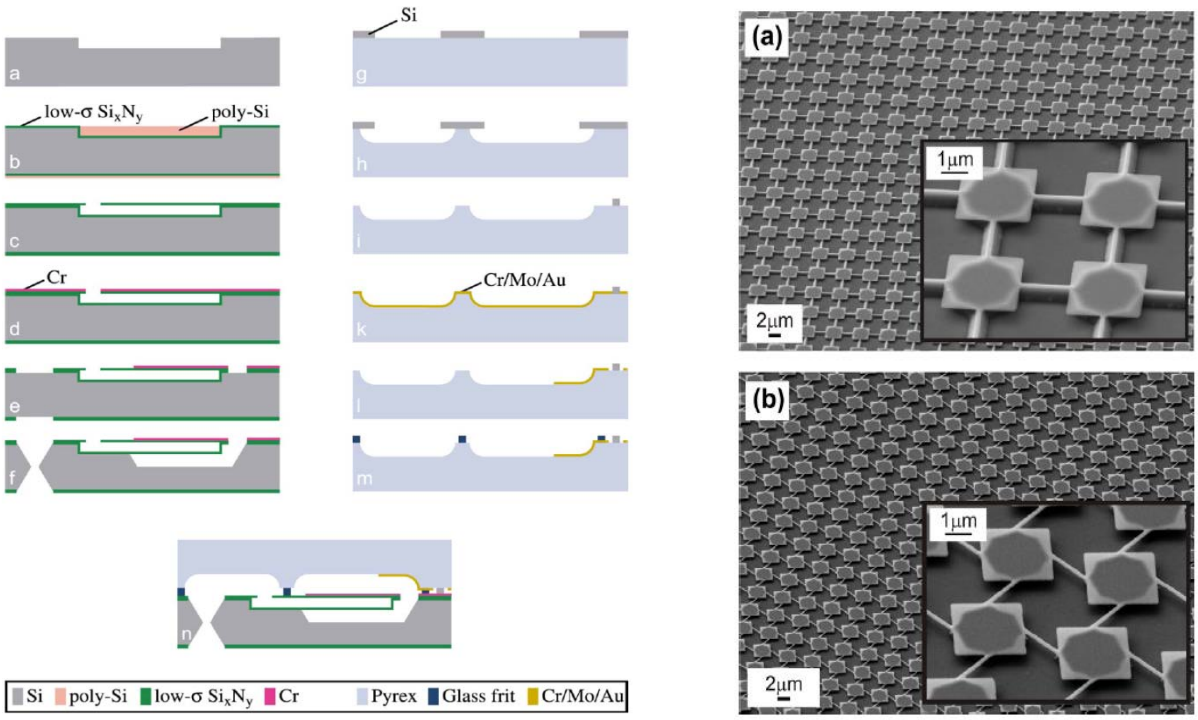

a) b)

Fig. 1–3. a) A microfabrication process that includes both surface and bulk micromachining steps for outlining of a suspended resonator with a silicon nitride structural layer and a sacrificial layer of polysilicon [46]. After etching the sacrificial layer and releasing the resonator, a glass frit bonding is carried out with a Pyrex wafer for packaging. b) Another example of bulk micromachining for releasing doubly clamped beams based on the crystallographic orientations of the silicon substrate [47].

Then the photoresist is exposed to the x-ray radiation using a special X-ray mask to transfer the desired design. By using a developer agent, the chemically modified photoresist is further removed from those irradiated areas. Afterwards by using micromolding or electroplating techniques, a metallic material is deposited on the uncovered areas. Typically, nickel is used as filler material. Finally, the remaining photoresist is removed leaving a metallic insert mould as shown in Fig. 1–4a. The applicability of this microfabrication technique can be extended to other low-cost fabrication strategies for replica moulding of other materials such as polymers using the final mould as a

template. The microfabrication technology, however, is not cost-effective because access to a synchrotron facility and a special custom photomask are required for X-ray light exposition.

Another versatile and multifunctional micromachining tool for fabricating microscale devices is the focused ion beam technique as it encompasses interesting characteristics such as high-resolution imaging, flexible micromachining, and the possibility to deposit thin-film layers onto a polymer substrate, see Fig. 1–4b. It consists of a highly ion focused beam generated by a liquid metal ion source (LMIS) that preferably uses Gallium as the main element because of its low melting temperature, low-pressure vapour and low volatility [48].

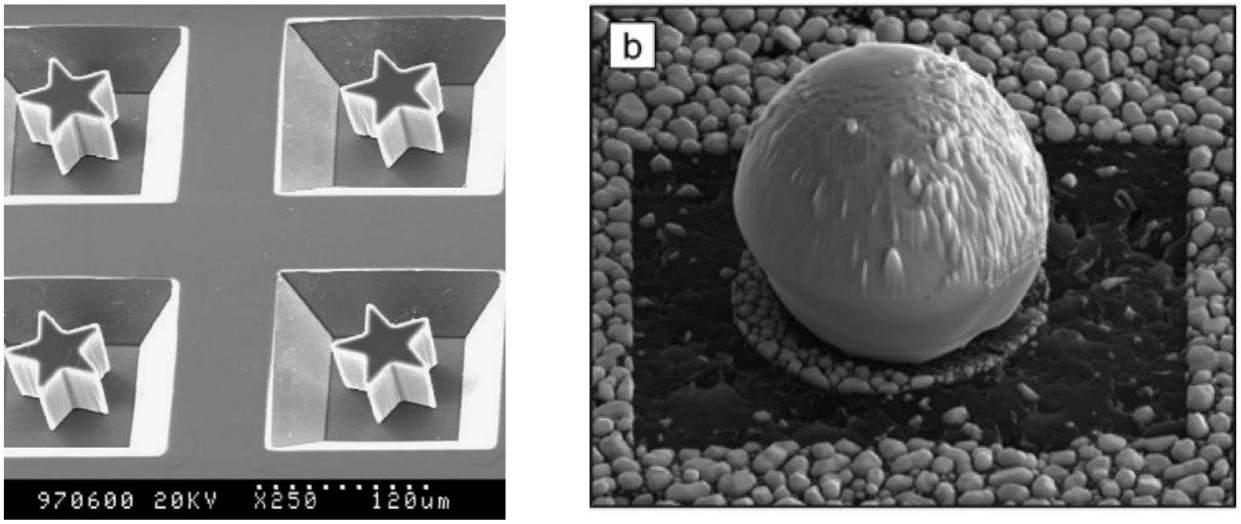

a) b)

Fig. 1–4. a) A combined microfabrication technique that creates high-aspect ratio metal stars using the UV-LIGA technology into silicon trenches produced by bulk micromachining [49] and b) SEM image of a large Sn sphere surrounded by Sn droplets sputtered by a 30 keV Ga focused Ion beam [48].

The high-milling resolution is obtained by focusing tightly the ion beam using electrostatic lenses and a small-sized field ionization source of the order of 5 nm [48]. Hence, the smaller the spot size is, the higher is the current density for milling the sample. Importantly, this microfabrication technique can directly sputter the sample without needing a photomask with an energy operation range between 10 to 200 keV [50]. The gas injection capabilities inside the chamber can enhance the etching of materials and enable the deposition of a nanometric layer of materials as well. Nevertheless, the low current density of ions causes a slow manufacturability time in comparison with other micromachining techniques.

The hot embossing is a fast and cost-effective microfabrication technique for replicating soft materials with high aspect ratios using a solid microscale mould as a template. The strategy is suitable for micromolding of complex patterns in polymer materials, which has significant

implications for the biomedical sector looking for the ability to manipulate low sample volumes with cost-effective and reproducible devices, see Fig. 1–5. The mould insert that contains the negative features of the design is embossed with a polymer substrate. For this, the temperature of the system is elevated up to the glass transition temperature of the polymer and using hard contact forces, the features of the mould insert are stamped into the polymer under vacuum conditions for avoiding air traps between the bonded materials. Afterwards, the material is cooled down and de-moulded at room temperature [51]. The insert mould should have low surface energy, low adhesion capabilities, and low friction coefficient to facilitate the de-embossing of both parts [52]. The major disadvantage of this technique is that some imperfections as is the roughness, lifetime and usage, and surface degradation of the master mould can impel the suitable replication of the polymer devices.

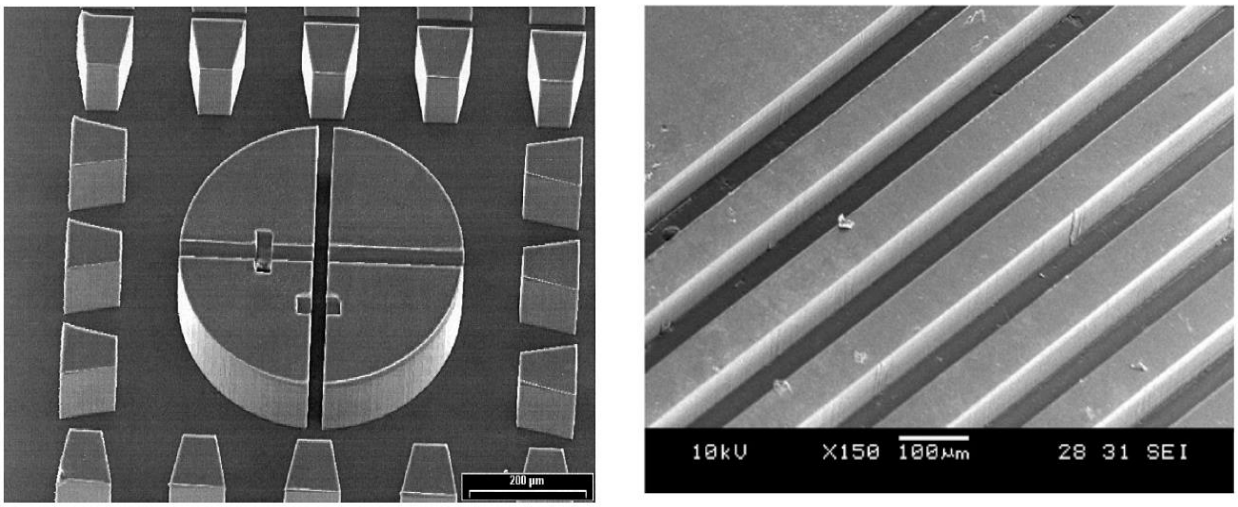

a) b)

Fig. 1–5. Examples of polymer structures manufactured by the hot embossing microfabrication technique. a) A test structure with high-aspect ratio made of polycarbonate (PC) [53] and b) COC (Topas-6017) polymer replica with well-defined microchannels [52].

Alternative fabrication methodologies have been explored for rapid prototyping of microdevices as a convenient way to address typical drawbacks involved in MEMS fabrication methods. The aim is to reduce expensive equipment at specialized clean-room facilities and save time to obtain a final device for fast testing and evaluation. Polymer based-structures fabricated by 3D printing methodologies have already been implemented as a potential future tool to design and build microfluidic devices. Microfluidics is an entire branch of MEMS technology that handles and manipulates low volumes of fluids towards the development of chemical and biological applications. By employing user-friendly software, the 3D computer-aided design (CAD) of microfluidic designs can be directly translated into polymer substrates by a typical layer-by-layer printing process without requiring intermediate steps. For instance, Moore et al. [54] prototyped a microfluidic valve and found out a comparable performance with those fabricated by conventional

microfabrication strategies. The most important 3D printing methodologies include stereolithography (SLA), fused deposition modelling (FDM) and selective laser sintering (SLS). Among them, the most promising with high-resolution capabilities is the mask projection microstereolithography, yet its spreading into the commercial market is still in progress [55], see Fig. 1–6a. Furthermore, other fabrication methods have undergone remarkable progress due to their unique capabilities to manufacture materials at small scale: laser-based lithographic writing and two-photon polymerization [56]. For instance, the latter one has been successfully employed to build and characterize a polymer suspended microchannel in a single manufacturing step [57], see Fig. 1–6b.

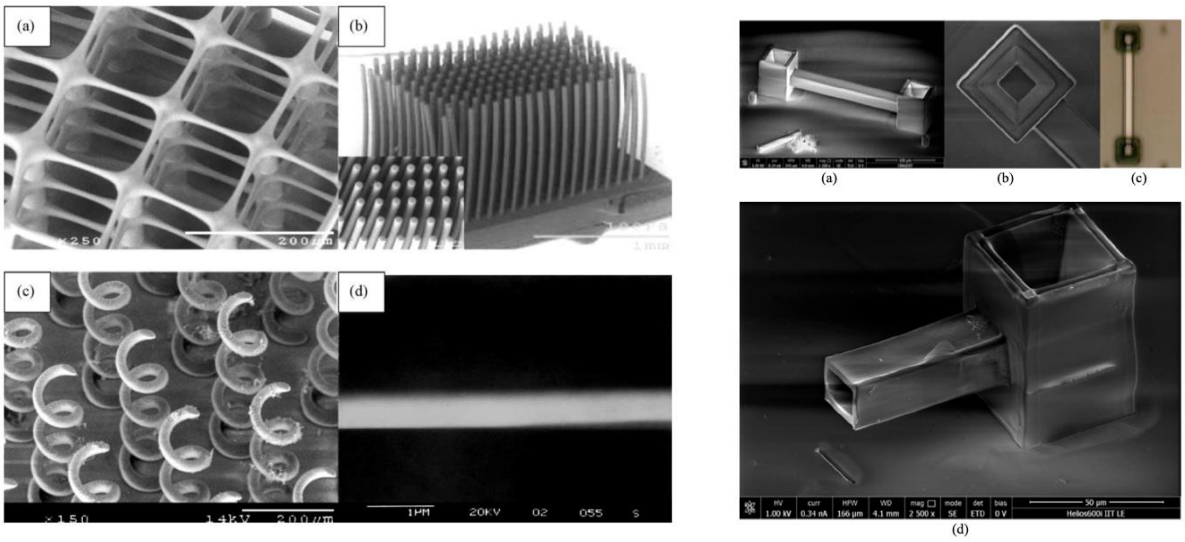

A) B)

Fig. 1–6. A) A SEM micrograph illustrates complex polymer microstructures that can be fabricated by the stereolithography technique such as arrays of high-aspect ratio: a) microbeams, b) microrods, c) coils, and d) thin suspended beams [58]. B) A polymer suspended microchannel made of SU-8 resin with wide microfluidic inlets manufactured with the two-photon lithography strategy [57].

Despite these endeavouring advantages, there is still a gap that needs to be narrowed for the acceptance of polymer materials for their utility in common MEMS applications. Downscaling the actual resolution size and layer thickness of 3D printing methods from 500-1000 μm into a 1-10 μm range will be paramount [55]. Future directions should also consider new polymer materials with higher compatibility with the chemical, biological or medical ongoing applications. Besides, polymer materials with good conductive properties, improved adhesion and, reduced porosity will render the possibility to directly integrate packaging methodologies at wafer-level scale for devices that require partial or full vacuum extraction and external electric interconnections.

1.2 How MEMS devices are detected and actuated?

Essentially, there are two operational modes for MEMS devices: static and dynamic. The static mode translates a surface stress shift due to induced changes on one of its surfaces by any molecular interaction or mass deposition. Whereas for the dynamic operational mode, the variation of the effective mass of the sensor is transduced into a shift of the resonance frequency of the resonator assuming that changes in the elastic constant are negligible. Conventionally, there are several approaches to acquiring the response of MEMS devices that are working under dynamic operational mode, among them we can find capacitive [59], [60], piezoresistive [61]–[63], optical [64]–[67] and piezoelectric [68], [69] methods. Table 1-1 shows the displacement sensitivity for MEMS devices using these detection methods. Although all of them have been proven useful, their implementation strongly depends on the fabrication process, materials, facilities and final application, as shown in Fig. 1–7.

Table 1-1. Comparison of the displacement sensitivity of commonly used detection methods for MEMS devices in dynamic mode

Detection method	Device dimensions $L \times W \times H$ μm	Displacement Sensitivity	Technology
Optical-lever [63]	210 x 28.5 x 12	0.20 pm/$\sqrt{Hz}$	Suspended Microchannel Resonators
Piezoresistive [63]	210 x 28.5 x 12	72 pm/$\sqrt{Hz}$	Suspended Microchannel Resonators
Michelson Interferometry [Present work]	270 x 10 x 4	0.12 pm/$\sqrt{Hz}$	Hollow Microbeam Resonators
Capacitive [70]	8 x 0.2 x 0.12	~0.4 fm/$\sqrt{Hz}$	Doubly clamped nanomechanical beam
Piezoelectric [71]	9 x 0.47 x 0.21	0.52 pm/$\sqrt{Hz}$	Doubly clamped nanomechanical beam

The optical detection method has particularly been an attractive solution for a wide variety of real-time biosensor and lab-on-a-chip devices due to its robustness and ultrasensitive features. For example, optical detection schemes have successfully been used for parallel readout of micro- and nanocantilevers [72], [73]. The ability to perform a non-contact measurement on the sample as well as to have a higher working distance range makes optical detection a sensitive and straightforward method to implement. In the optical detection methods, we can identify three main configurations with high sensitivity and robustness that can be employed to measure nanometric displacements: optical-lever technique, Michelson interferometer and Fabry-Perot interferometer. The optical-lever technique has been widely used for detection of microcantilever displacements given its high sensitivity and easy implementation. In here, a laser beam is reflected off the cantilever onto a

position sensitive photodiode (PSD) [74]. In the Michelson interferometry configuration, the probe beam interferes with a reference beam upon the photodetector. The interference will be constructive or destructive, depending on the phase of the arriving waves [75]. Finally, in the Fabry-Perot interferometry, the power fluctuations in the probe beam are monitored as the resonator moves. In this case, the probe beam interferes with a signal reflected from a reference substrate located underneath the structure; both highly reflective surfaces form an optical cavity that produces the interference pattern [76]. Despite the effectiveness and differences between the optical schemes, practically the three configurations detect the out-of-plane surface motion of the resonators based on either a change in the amplitude or the phase of the laser beam.

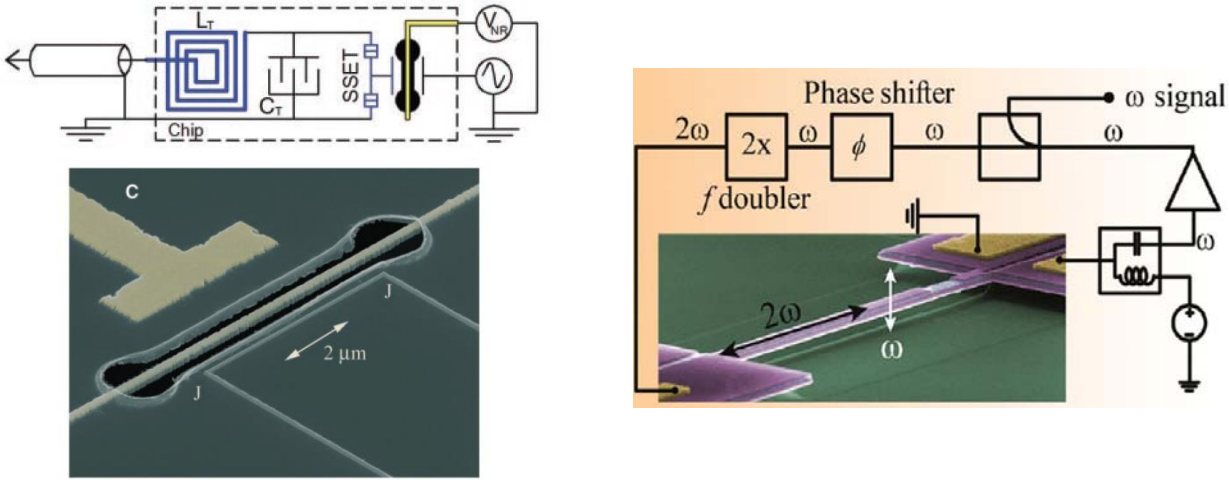

a) b)

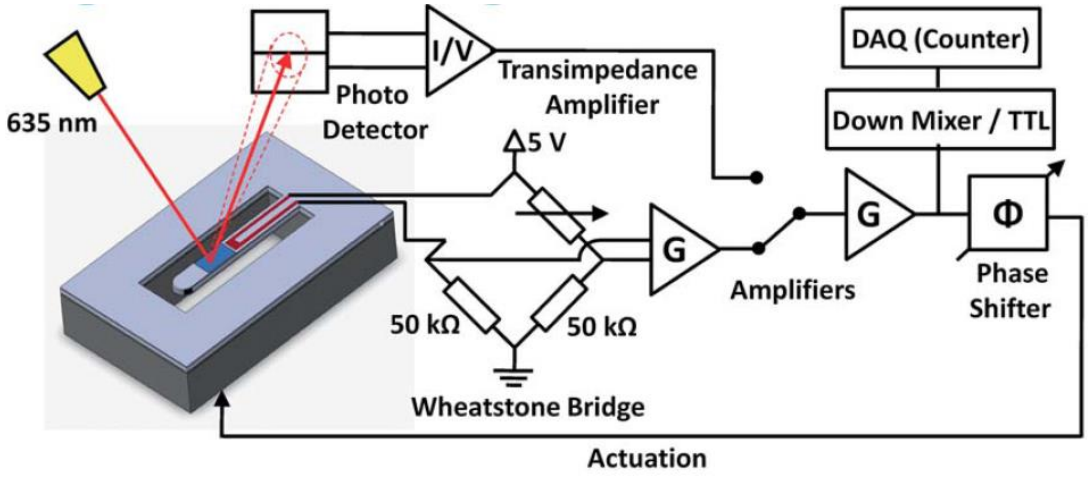

b)

Fig. 1–7. a) Examples of MEMS detection methods. a) Capacitive displacement detection of a nanomechanical beam with a single-electron transistor (SET) [70]. b) Piezoelectric detection of a doubly clamped nanomechanical beam using a parametric feedback oscillator method (PFO) [71]. c) Optical and piezoresistive detection of the out-of-plane response of SMR devices [63].

In scientific and engineering contexts, many systems exhibit resonance behaviours when a small excitation signal is applied producing large vibration amplitudes. In MEMS devices, such resonance phenomena can be exploited to transduce the effects of the resonance frequency and quality factor of the devices for various purposes including mass sensing applications [77], viscosity sensing [78] and even for energy harvesting [79]. The quality factor measures the ability of a mechanical system to store energy. Henceforth, for such applications, it is paramount to perform repeatable and reliable measurements of the resonance frequency and quality factor of the resonators. The resonant frequency and quality factor of MEMS devices can be measured with and without active excitation to improve the stability and resolution of the peak frequency response. For instance, when no active actuation is performed, the resonant frequency and quality factor of devices is obtained by acquiring the thermomechanical noise of the resonator. For active actuation of MEMS devices, it is feasible to elicit large response amplitudes by typically exciting the mechanical system into resonance by employing a time-periodic signal. This force can be applied by using either a frequency sweep or a direct impulse drive; in this case, resonance will be exhibited when the frequency of the excitation signal commensurates with the natural frequency of the resonator. MEMS devices can be actuated differently based on the transduction of the excitation drive signal. For instance, thermomechanical [80], [81], electrostatic [82], [83], magnetically [78], [84], [85], piezoresistive [62], [63] and piezo-ceramic [25], [33] are commonly actuation methods employed. It is reasonable to assume that the resonance frequency is determined consistently regardless of the actuation scheme applied unless the actuation scheme changes some of the intrinsic features of the resonator [86].

1.3 Suspended Microchannel Resonators

The sensitivity of smaller mechanical resonators, however, may be undermined due to several issues. In the pursuit of higher sensitivities, the effective mass of the beams has significantly been diminished. By downscaling the dimensions of the sensor, not only its mechanical stiffness increases, but also its natural frequency response and, as a consequence, new challenges have to be addressed for implementing high-throughput transduction systems. Importantly, there is another critical factor that attenuates the mechanical sensor performance in a fluid environment. When a resonator is immersed in a viscous liquid, an overdamped response of the resonator produces a rapid dissipation of energy, which degrades the frequency resolution and sensitivity of the sensor related to the viscosity of the medium, as shown in Fig. 1–8. An innovative approach to solving the above limitation was proposed by Burg et al. [87]. This method involved integrating a fluidic channel into a suspended microcantilever, namely suspended microchannel resonator (SMR), thereby avoiding damping and viscous drag produced by the fluid environment, as shown in Fig. 1–9. This mechanical mass sensor emerged as an alternative label-free detection method in comparison to other mass sensing methodologies as the Surface Plasmon Resonance (SPR) and the Quartz Crystal Microbalance (QCM).

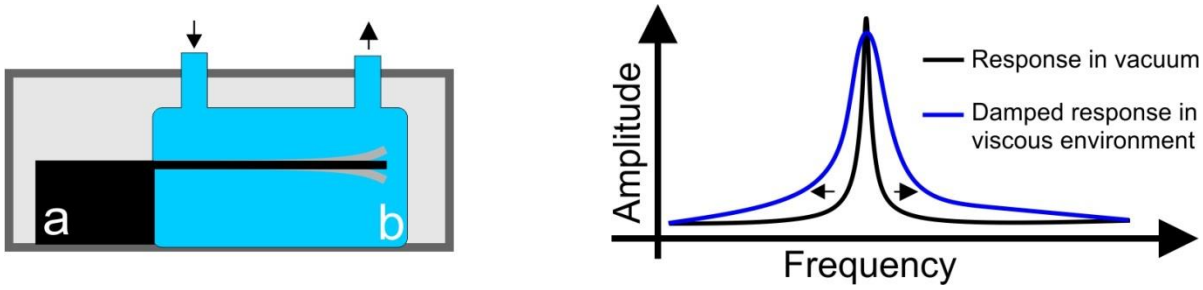

Fig. 1–8. A microcantilever beam (a) oscillating in a liquid environment (b) demonstrates the effect of viscous drag. As a result, the response of the beam in the frequency domain is overdamped, broadening the frequency peak and degrading the frequency resolution of the system.

The main objective was to offer an advanced sensing platform towards a smaller volume consumption of samples, an increased sensitivity and the ability to scale down the technology to extend their utility to other bioanalytical applications. In general, a SMR device can work in two operational modes: affinity-based and flow-through detection mode. The affinity-based detection includes previous biofunctionalization procedures that provide specific capture of molecules onto the inner microchannel walls while continuously replenishing the microchannel. Alternatively, the flow-through detection allows identification of fluids and small entities that are streaming through the microchannel. In both cases, the sensitivity is proportional to the resonant frequency, which in turn is inversely proportional to the square root of the effective mass of the sensor.

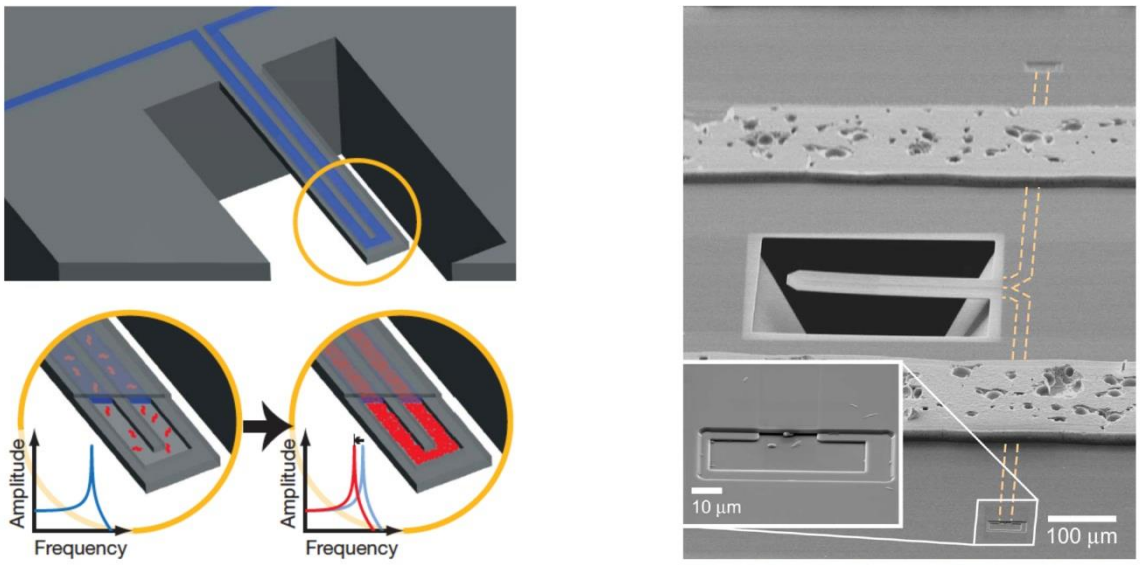

Fig. 1–9. Functionality principle of a suspended microchannel resonator (SMR). The resonator consists of an embedded channel into a microcantilever resonator that tracks the frequency shifts caused by the mass changes events inside the cavity [88]. b) The SEM picture illustrates a fabricated device 300 μm long with a channel cross-section of 1 x 20 μm in which a glass frit bonding strategy is implemented for hermetic packaging [46].

Since the first functionality principle of SMR devices was demonstrated, subsequent efforts were made to improve their frequency response and resolution technologically and obtain better responsivities for mass spectrometry applications. In 2006, the SMR devices were operated under vacuum conditions with the addition of a glass frit bonding for hermetic packaging [46]. For pressures of $\sim 1\ Torr$, the measured Q-factor was five times better than the one measured in air (Q = 90). Also, the frequency resolution was improved by using a feedback control for the electrostatic actuation of the resonators. As a result, the recognition of biomolecules with this technology (0.01 ng/cm^2) outperformed the adsorbed mass resolution of contemporary label-free sensors. A year later, the SMR technology successfully weighted single gold nanoparticles, bacterial cells (*E. coli* and *B. subtilis*) and adsorbed proteins in a flow-through detection mode [88]. To achieve this, the resonators were designed to sustain higher natural frequencies (around 220 KHz in air) by diminishing their dimensions (L x W x H: 200 μm x 33 μm x 7 μm). Also, very thin frequency spectrums were depicted by incorporating a getter layer into the packaging of the devices, which improved the frequency stability and resolution of the detection system. Furthermore, Lee et al. [89] studied the uncertainties of mass particle sensing caused by the position of the particles near the tip of the resonator. In this methodology, they analysed the second flexural bending mode to circumvent the dependence of the location of the particles along the microchannels.

Under this premise, the SMR devices opened the gate for a broad range of biological applications for measuring the mass, density and size of polystyrene particles, *Escherichia coli* bacteria and human red blood cells with a resolution down to $10^{-4}\mathrm{g/cm^3}$ [32]. In 2010, femtogram detection of the growing rates of individual cells such as *Bacillus subtilis*, *Escherichia coli*, *Saccharomyces cerevisiae* and even mouse lymphoblasts was achieved by using a buoyant mass methodology with SMR devices [90]. This approach implemented an accurate pressure control of the sample delivery system to allow consecutive buoyant mass measurements of a single cell, see Fig. 1–10a. On the other hand, improvements on the surface functionalization of the embedded microchannels of SMR devices potentiated their utility for detecting biomarkers in undiluted serum. The authors [34] used a surface-binding assay (superlow fouling surface) based on zwitterionic polymers and a reference microcantilever to detect Activated Leukocyte Cell Adhesion Molecules (ALCAM) in undiluted serum with a limit of detection of 10 ng/mL. Moreover, Grover et al. [91] brought new insights in the understanding of cell states during drug delivery treatments. In their methodology, a single-cell was weighted in two fluids of different density. By applying the Archimedes principle, the linear relationship between the buoyant mass and the fluid density could predict the mass, volume and density of a single-cell at a ratio of 500 cells per hour with a density precision of 0.001 g/mL. The buoyant mass of cells was also measured using alternative SMR configurations. Bryan et al. proposed a dual SMR resonators for determining the mass, volume and density of a single cell based on the Archimedes method [92]. In contrast to the previous approach [91], the devices incorporated a serpentine fluidic channel to interconnect both SMR devices. In this way, the single cells were weighted in the two devices during a single sample injection reducing the time for diffusing the second fluid with the interrogated sample.

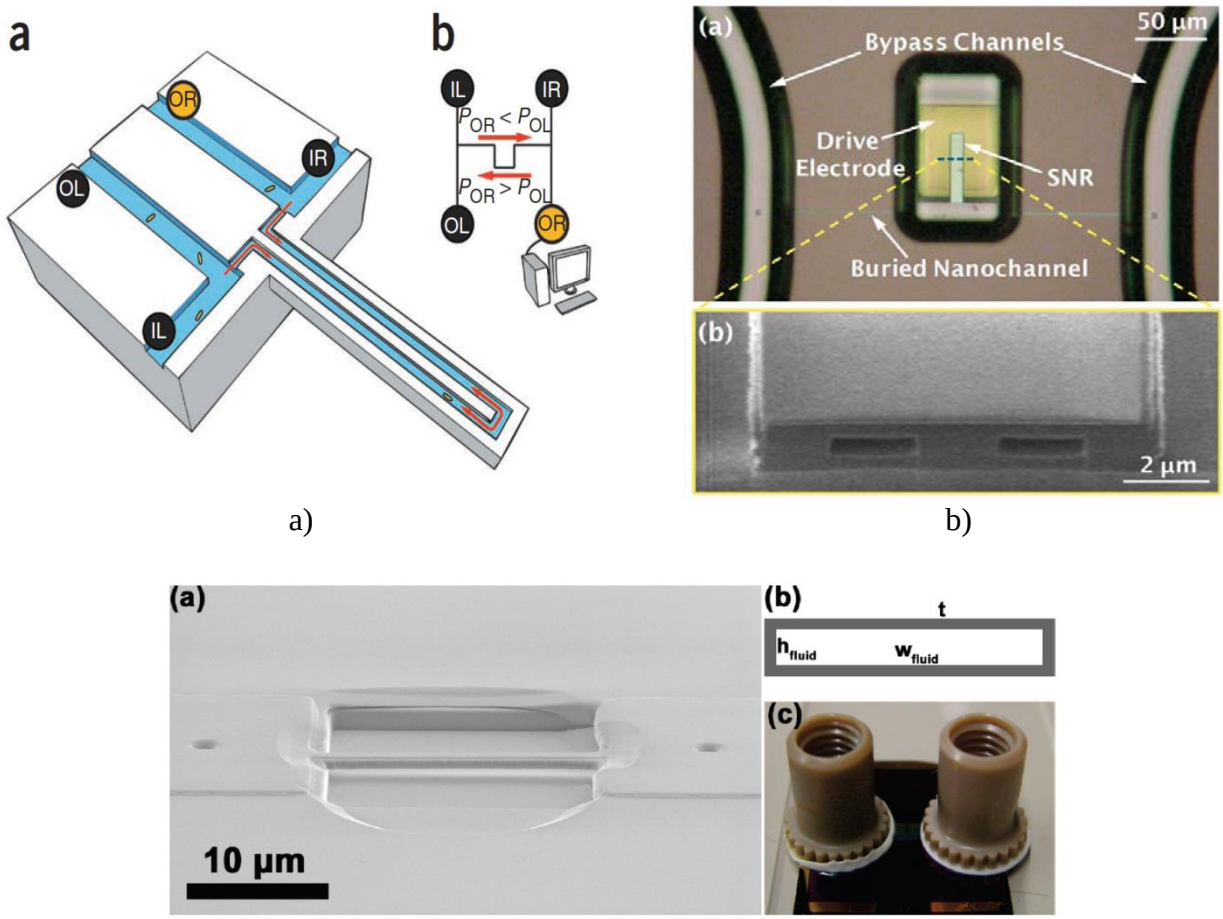

a) b)

c)

Fig. 1–10. a) A SMR device for dynamic trapping of single cells with a precise control for fluid sample delivery [90]. b) SEM micrograph of a suspended nanochannel resonator (SNR) with a buried channel of 2 µm wide and 700 nm height for gold nanoparticle detection in flow-through mode [93]. c) A suspended and hollowed doubly clamped nanobeam resonator fabricated by conformably coating a Si_3N_4 material over a polysilicon sacrificial layer. Nanofluidic ports were incorporated for capillary filling of the nanochannels [94].

The possibilities to reduce the dimensions of SMR devices increased due to the advances of the micro- and nanoscale fabrication methodologies. In 2010, Lee et al. introduced a cantilever design with 50 μm long, 10 μm wide and 1.3 μm thick containing an embedded channel of 2 μm wide and 700 nm height [93]. The new device was named suspended nanochannel resonator (SNR), had a resonance frequency of 630 KHz with Q-factors around 8000 in air, as can be seen in Fig. 1–10b. This approach showed promising advantages toward attogram mass resolution of gold nanoparticles in solution because it increased the averaging time for weighting the nanoparticles. Basically, the centrifugal forces derived from the vibration of the resonator trapped the particles in the apex of the cantilever microchannel increasing their residence time. Similarly, other authors took the challenge of fabrication devices with nanoscale dimensions [94]. SNR devices with less than 100 pg in mass were built by conformably coating a structural silicon nitride material onto a polysilicon sacrificial layer with a doubly clamped topology, see Fig. 1–10c. The frequency of operation was around 25

MHz with Q-factors of 800 in vacuum conditions. As proof of concept, the device was filled by capillary forces with liquids of varying densities yielding a mass responsivity of 100 Hz/fg. SMR devices were also compatible with other sensing platforms. Dextras et al. [37] expanded the application of SMR devices by producing a microsystem containing a SMR device with a nanofluidic concentrator. The aim was to measure the concentration of samples (in bovine serum albumin solution) prepared by the nanofluidic concentrator using the SMR devices as a densitometer.

Until this point, the resonant frequency shift of SMR devices was the principal parameter used to resolve for mass changes inside the microchannels, however, in some circumstances, the quality factor of SMR devices also showed subtle variations depending on the viscosity of the samples. This behaviour captured the attention of some researchers for studying and understanding the energy dissipation of suspended microchannels. In this way, Sader et al. [95], [96] proposed a comprehensive study of the effect of the Poisson's ratio of the structural material of SMR devices and the governing mechanisms of fluid inertia based on the Q-factor. As a result, SMR devices were used to characterize the dynamic viscosity of fluids with a resolution close to 0.035 cP [97]. In this approach, two methodologies were employed to measure the viscosity of samples in a low viscosity regime (< 10 cP). The first was an amplitude-based method that tracked the amplitude of the resonant frequency spectrum, whereas the second one was based on tracking changes in the quality factor of the spectrum. Both methodologies showed a bilinear effect when working with lower (1- 4 cP) and higher fluid inertia domains (4 - 8 cP). However, the amplitude-based showed an enhanced time response within 1 ms in contrast to the Q-factor methodology that took about 30 s.

The feasibility to integrate SMR devices with other detection methods was also interrogated by Lee et al. [63]. SMR devices with integrated piezoresistive sensors enabled the characterization of the mass of budding yeast cells and polystyrene beads with comparable mass resolutions (3.4 fg in a 1 KHz bandwidth) to the conventional optical-lever detection method, as shown in Fig. 1–7c. In this way, new insights were considered for implementing an array of SMR for multiplexed biosensing. Moreover, in 2011 a new concept of the mass sensor was proposed by Agache et al. [77] based on embedding microchannels in plate Lamé resonators to exhibit higher frequency responses and Q-factor values without the need for hermetic packaging as can be seen in Fig. 1–11a. The frequency of operation of these devices was around 78 MHz showing Q-factors within 1500 - 3500 in the air and the large surface-to-volume ratio of the resonators yielded a mass responsivity of 864 fg/KHz. Besides, various sources of energy dissipation were investigated for plate Lamé resonators with embedded rectangular microchannels primarily focusing on the channel design, vibration amplitudes and flow conditions [98]. An alternative fabrication method of SMR devices was proposed by Khan et al. [99], see Fig. 1–11b. In this approach, a SMR device was fabricated using silicon-rich-nitride (SRN) to facilitate the visual inspection of processes taking place inside the channels to further conduct density and viscosity measurements in liquid phase reagents. The SRN material had higher Young's modulus, and the topology of the microchannel protruded out from the based substrate by implementing surface micromachining processes. This technology was also implemented to measure the density and viscosity of liquid phase reagents including oil samples [25] and to detect molecular signatures in picoliter sample fluids using a bimetallic cantilever with an embedded microchannel with a wavelength dependence under infrared light (IR) [100]. More

recently, an embedded nanochannel with a cross-section of 865 nm width and 470 nm height was monolithically integrated with CMOS technology for extending the detection alternatives and capabilities of SMR devices [101], as shown in Fig. 1–11.

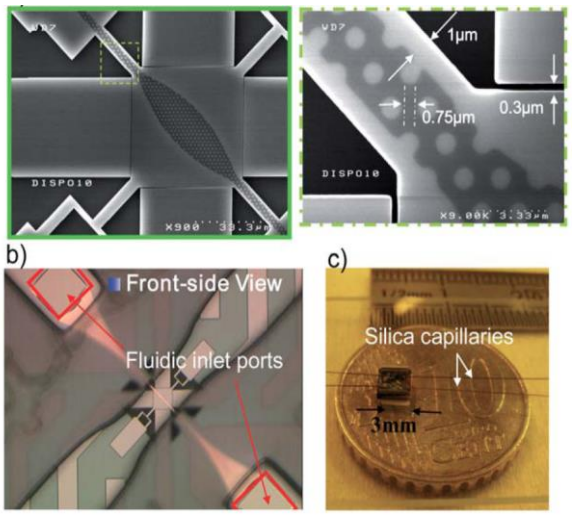

a)

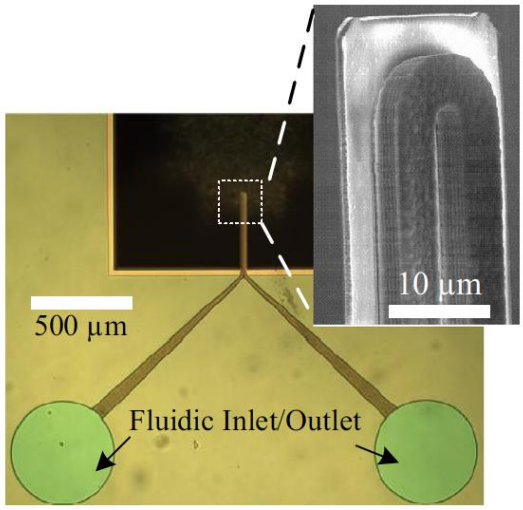

b)

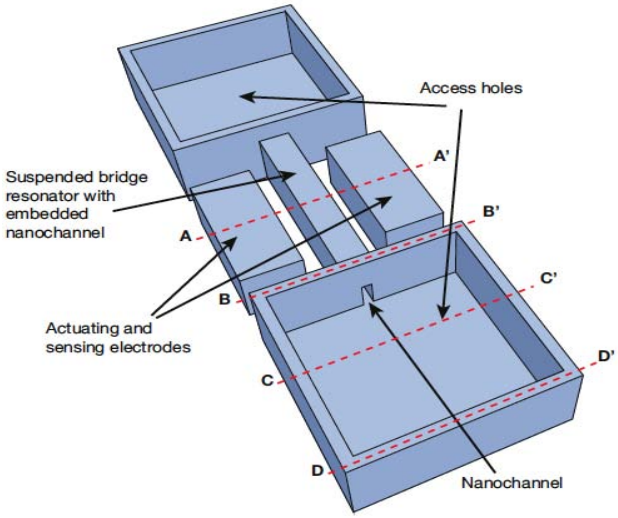

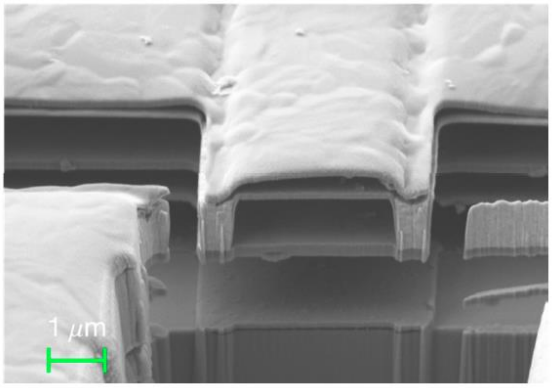

c)

Fig. 1–11. a) Suspended resonators based on embedded microchannels in plate Lamé resonators to exhibit higher frequency responses and Q-factor values without the need for vacuum and packaging [77]. b) Transparent SMR device made of rich SiN with a protruded out topology that simplifies the visual inspection of samples [99]. c) A 6 fL capacity suspended nanochannel resonator monolithically integrated with CMOS technology for electrostatic actuation and capacitive detection on-chip [101].

Finally, recent efforts of this technology showed promising advances in mass spectrometry to characterize biomolecular complexes, small organelles and nanoparticles in solution by extending the dynamic range of SMR devices using correlation analysis [102], precise quantification of nanoparticles down to 10 nm with a throughput of more than 18,000 particles per hour [33] and measurement of the aggregation kinetics of proteins into amyloid fibrils [103].

1.4 Array of Hollowed Microbeams Resonators

The proposed mass sensing platform in this Thesis work consists of a set of resonators with embedded microfluidic channels inside. The design incorporates arrays of closely spaced doubly clamped microbeams having slightly different effective lengths introduced by a tilt angle at both clamped supports. In this configuration, every resonator is characterized by unique properties such as resonant frequency, elastic constant, quality factor, and sensitivity. The principle of operation of the HMB sensor consists of evaluating the shifts in the resonant frequency of each resonator due to changes in their effective masses when a sample fluid or analyte of specific density or viscosity is streaming through the embedded microchannels as Fig. 1–12 shows.

The doubly clamped configuration of the resonators provides more flexibility for fabricating straight microchannels with different dimensions to facilitate the input and output of liquid phase solutions. Also, clogging of the microfluidic channels will be reduced since a U-shaped microfluidic channel design is not necessary. The design of the set of resonators will be robust enough to withstand higher pumping pressures without achieving material failure. Although several approaches have already demonstrated the use of suspended resonators to characterize liquid phase analytes [25]-[94], an array format of hollow doubly clamped beams has not been reported before. Furthermore, the fabrication of devices would be relatively straightforward since no external connections are needed as it is the case with other measurement methods, which integrate built-in capacitive [59],[60] or piezoresistive [104],[105] sensors on-chip increasing the fabrication complexity and cost.

Although the doubly clamped configuration will constrain the mechanical motion of the resonators, and hence the dynamic range will not be high, the high-frequency range of the resonators (1 MHz) will be advantageous aiming for improved sensitivities and for reducing background low-frequency noise. For this reason, highly sensitive transduction methodologies such as those based on optical detection schemes come into play, as a Michelson Interferometer, to measure the nanometric displacements of HMB resonators oscillating at higher resonant frequencies. The optical readout will enable the measurement of several resonators simultaneously in a single acquisition line. In this way, the captured interferometric signal from the set of resonators will be processed to interpret the response of each resonator by applying computational routes, as is the real-time deconvolution.

On the other hand, it is noteworthy that reducing the mass and size of the resonators with embedded microchannels to achieve very sensitive transducers complicates their fabrication process. Also, the maximum volume of fluid that can flow through the microchannels and the maximum achievable

flow rates to optimize detection times can be limited by downscaling the fluidic channel dimensions since kinetics plays a major role in these devices [106]. Hence, we have proposed embedded microchannels with higher depths for biological applications wherein cells or bacteria of large sizes can be involved, as is the case of red blood cells. Also by constraining the fluidic samples inside of the microresonators the applicability range of the sensor can be extended to fluids that are not transparent as whole blood without interfering with the optical detection method.

Last but not least, micromechanical mass sensors integrating embedded microchannels have the potential to impact on a broad range of applications in which accurate and repeatable mass measurements may be required. Particularly, this technology may be feasible to evaluate in real-time not only the physical properties of fluids but also in ascertaining analytes present at low concentrations for quality testing and performance purposes which are essential for the industrial and medical sectors. As a result, HMB resonators could be integrated into Lab-on-a-Chip systems as a valuable and low-cost assessment tool for bioanalytical applications making possible the replacement of currently used analytical methods that generally require large volume samples, need long evaluation times and have limited sensitivity range.

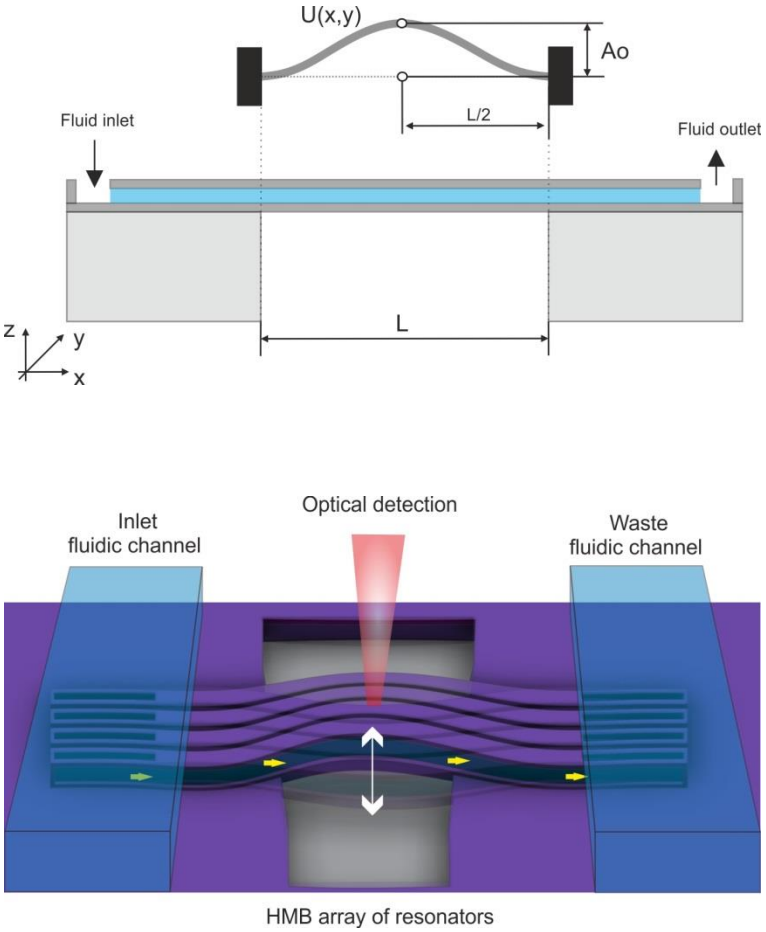

Fig. 1–12. Working principle of the HMB device. The fluid sample is contained in a microchannel embedded in a doubly clamped resonator. The response of the sensor is measured in dynamic operation to track the changes in the resonance frequency response when streaming sample solutions of different densities and viscosities. $\mathrm{U}(\mathrm{x},\mathrm{y})$ corresponds to the displacement function of the resonator and A_0 corresponds to the maximum displacement measured at the midspan of the beam $L/2$.

References

[1] A. Khademhosseini, R. Langer, J. Borenstein, and J. P. Vacanti, 'Microscale technologies for tissue engineering and biology', *Proc. Natl. Acad. Sci.*, vol. 103, no. 8, pp. 2480–2487, Feb. 2006.

[2] H. Campanella, J. A. Plaza, J. Montserrat, A. Uranga, and J. Esteve, 'High-frequency sensor technologies for inertial force detection based on thin-film bulk acoustic wave resonators (FBAR)', *Microelectron. Eng.*, vol. 86, no. 4–6, pp. 1254–1257, Apr. 2009.

[3] Kudrle T D, Neves H P, Rodger D C and MacDonald N C, 'A microactuated millimeter wave phase shifter', *Tech Dig. 10th Int Conf Solid-State Sens. Actuators*, pp. 1276–9, 1999.

[4] W. Xu, J. Appel, and J. Chae, 'Real-Time Monitoring of Whole Blood Coagulation Using a Microfabricated Contour-Mode Film Bulk Acoustic Resonator', *J. Microelectromechanical Syst.*, vol. 21, no. 2, pp. 302–307, Apr. 2012.

[5] A. Folch, A. Ayon, O. Hurtado, M. A. Schmidt, and M. Toner, 'Molding of Deep Polydimethylsiloxane Microstructures for Microfluidics and Biological Applications', *J. Biomech. Eng.*, vol. 121, no. 1, pp. 28–34, Feb. 1999.

[6] K. A. Addae-Mensah, N. J. Kassebaum, M. J. Bowers, R. S. Reiserer, S. J. Rosenthal, P. E. Moore, and J. P. Wikswo, 'A flexible, quantum dot-labeled cantilever post array for studying cellular microforces', *Sens. Actuators Phys.*, vol. 136, no. 1, pp. 385–397, May 2007.

[7] N. Roxhed, T. C. Gasser, P. Griss, G. A. Holzapfel, and Gö. Stemme, 'Penetration-Enhanced Ultrasharp Microneedles and Prediction on Skin Interaction for Efficient Transdermal Drug Delivery', *J. Microelectromechanical Syst.*, vol. 16, no. 6, pp. 1429–1440, Dec. 2007.

[8] J. Chaste, A. Eichler, J. Moser, G. Ceballos, R. Rurali, and A. Bachtold, 'A nanomechanical mass sensor with yoctogram resolution', *Nat. Nanotechnol.*, vol. 7, no. 5, pp. 301–304, May 2012.

[9] J. J. Ruz, J. Tamayo, V. Pini, P. M. Kosaka, and M. Calleja, 'Physics of Nanomechanical Spectrometry of Viruses', *Sci. Rep.*, vol. 4, Aug. 2014.

[10] P. M. Kosaka, V. Pini, J. J. Ruz, R. A. da Silva, M. U. González, D. Ramos, M. Calleja, and J. Tamayo, 'Detection of cancer biomarkers in serum using a hybrid mechanical and optoplasmonic nanosensor', *Nat. Nanotechnol.*, vol. advance online publication, Nov. 2014.

[11] M. T. Boudjiet, J. Bertrand, F. Mathieu, L. Nicu, L. Mazenq, T. Leïchlé, S. M. Heinrich, C. Pellet, and I. Dufour, 'Geometry optimization of uncoated silicon microcantilever-based gas density sensors', *Sens. Actuators B Chem.*, vol. 208, pp. 600–607, Mar. 2015.

[12] C. Riesch, E. K. Reichel, A. Jachimowicz, J. Schalko, P. Hudek, B. Jakoby, and F. Keplinger, 'A suspended plate viscosity sensor featuring in-plane vibration and piezoresistive readout', *J. Micromechanics Microengineering*, vol. 19, no. 7, p. 075010, Jul. 2009.

[13] I. Etchart, H. Chen, P. Dryden, J. Jundt, C. Harrison, K. Hsu, F. Marty, and B. Mercier, 'MEMS sensors for density–viscosity sensing in a low-flow microfluidic environment', *Sens. Actuators Phys.*, vol. 141, no. 2, pp. 266–275, Feb. 2008.

[14] B. A. Bircher, L. Duempelmann, K. Renggli, H. P. Lang, C. Gerber, N. Bruns, and T. Braun, 'Real-Time Viscosity and Mass Density Sensors Requiring Microliter Sample Volume Based on Nanomechanical Resonators', *Anal. Chem.*, vol. 85, no. 18, pp. 8676–8683, Sep. 2013.

[15] D. Sparks, R. Smith, V. Cruz, N. Tran, A. Chimbayo, D. Riley, and N. Najafi, 'Dynamic and kinematic viscosity measurements with a resonating microtube', *Sens. Actuators Phys.*, vol. 149, no. 1, pp. 38–41, Jan. 2009.

[16] J. Zhang, C. Dai, X. Su, and S. J. O'Shea, 'Determination of liquid density with a low frequency mechanical sensor based on quartz tuning fork', *Sens. Actuators B Chem.*, vol. 84, no. 2–3, pp. 123–128, May 2002.
[17] Y. Liu, R. DiFoggio, K. Sanderlin, L. Perez, and J. Zhao, 'Measurement of density and viscosity of dodecane and decane with a piezoelectric tuning fork over 298–448K and 0.1–137.9MPa', *Sens. Actuators Phys.*, vol. 167, no. 2, pp. 347–353, Jun. 2011.
[18] P. Enoksson, G. Stemme, and E. Stemme, 'Fluid density sensor based on resonance vibration', *Sens. Actuators Phys.*, vol. 47, no. 1–3, pp. 327–331, Mar. 1995.
[19] A. J. Ricco and S. J. Martin, 'Acoustic wave viscosity sensor', *Appl. Phys. Lett.*, vol. 50, no. 21, pp. 1474–1476, May 1987.
[20] P. Rust, D. Cereghetti, and J. Dual, 'A micro-liter viscosity and density sensor for the rheological characterization of DNA solutions in the kilo-hertz range', *Lab. Chip*, vol. 13, no. 24, pp. 4794–4799, Nov. 2013.
[21] L. Müller, S. Sinn, H. Drechsel, C. Ziegler, H.-P. Wendel, H. Northoff, and F. K. Gehring, 'Investigation of Prothrombin Time in Human Whole-Blood Samples with a Quartz Crystal Biosensor', *Anal. Chem.*, vol. 82, no. 2, pp. 658–663, Jan. 2010.
[22] O. Cakmak, C. Elbuken, E. Ermek, A. Mostafazadeh, I. Baris, B. Erdem Alaca, I. H. Kavakli, and H. Urey, 'Microcantilever based disposable viscosity sensor for serum and blood plasma measurements', *Methods*, vol. 63, no. 3, pp. 225–232, Oct. 2013.
[23] M. Youssry, N. Belmiloud, B. Caillard, C. Ayela, C. Pellet, and I. Dufour, 'A straightforward determination of fluid viscosity and density using microcantilevers: From experimental data to analytical expressions', *Sens. Actuators Phys.*, vol. 172, no. 1, pp. 40–46, Dec. 2011.
[24] J. Toledo, T. Manzaneque, J. Hernando-García, J. Vazquez, A. Ababneh, H. Seidel, M. Lapuerta, and J. L. Sánchez-Rojas, 'Comparison of quartz tuning forks and AlN-based extensional microresonators for viscosity measurements in oil/fuel mixtures', 2013, p. 87630L.
[25] M. F. Khan, S. Schmid, P. E. Larsen, Z. J. Davis, W. Yan, E. H. Stenby, and A. Boisen, 'Online measurement of mass density and viscosity of pL fluid samples with suspended microchannel resonator', *Sens. Actuators B Chem.*, vol. 185, pp. 456–461, Aug. 2013.
[26] S. Boskovic, J. W. M. Chon, P. Mulvaney, and J. E. Sader, 'Rheological measurements using microcantilevers', *J. Rheol. 1978-Present*, vol. 46, no. 4, pp. 891–899, Jul. 2002.
[27] N. McLoughlin, S. L. Lee, and G. Hähner, 'Temperature dependence of viscosity and density of viscous liquids determined from thermal noise spectra of uncalibrated atomic force microscope cantilevers', *Lab. Chip*, vol. 7, no. 8, p. 1057, 2007.
[28] M. Hennemeyer, S. Burghardt, and R. W. Stark, 'Cantilever Micro-rheometer for the Characterization of Sugar Solutions', *Sensors*, vol. 8, no. 1, pp. 10–22, Jan. 2008.
[29] N. McLoughlin, S. L. Lee, and G. Hähner, 'Simultaneous determination of density and viscosity of liquids based on resonance curves of uncalibrated microcantilevers', *Appl. Phys. Lett.*, vol. 89, no. 18, p. 184106, 2006.
[30] R. Paxman, J. Stinson, A. Dejardin, R. A. McKendry, and B. W. Hoogenboom, 'Using Micromechanical Resonators to Measure Rheological Properties and Alcohol Content of Model Solutions and Commercial Beverages', *Sensors*, vol. 12, no. 5, pp. 6497–6507, May 2012.
[31] E. Nuxoll, 'BioMEMS in drug delivery', *Adv. Drug Deliv. Rev.*, vol. 65, no. 11–12, pp. 1611–1625, Nov. 2013.
[32] M. Godin, A. K. Bryan, T. P. Burg, K. Babcock, and S. R. Manalis, 'Measuring the mass, density, and size of particles and cells using a suspended microchannel resonator', *Appl. Phys. Lett.*, vol. 91, no. 12, pp. 123121–123121–3, Sep. 2007.

[33] S. Olcum, N. Cermak, S. C. Wasserman, K. S. Christine, H. Atsumi, K. R. Payer, W. Shen, J. Lee, A. M. Belcher, S. N. Bhatia, and S. R. Manalis, 'Weighing nanoparticles in solution at the attogram scale', *Proc. Natl. Acad. Sci.*, p. 201318602, Jan. 2014.

[34] M. G. von Muhlen, N. D. Brault, S. M. Knudsen, S. Jiang, and S. R. Manalis, 'Label-Free Biomarker Sensing in Undiluted Serum with Suspended Microchannel Resonators', *Anal. Chem.*, vol. 82, no. 5, pp. 1905–1910, Mar. 2010.

[35] L. M. Lechuga, J. Tamayo, M. Álvarez, L. G. Carrascosa, A. Yufera, R. Doldán, E. Peralías, A. Rueda, J. A. Plaza, K. Zinoviev, C. Domínguez, A. Zaballos, M. Moreno, C. Martínez-A, D. Wenn, N. Harris, C. Bringer, V. Bardinal, T. Camps, C. Vergnenègre, C. Fontaine, V. Díaz, and A. Bernad, 'A highly sensitive microsystem based on nanomechanical biosensors for genomics applications', *Sens. Actuators B Chem.*, vol. 118, no. 1–2, pp. 2–10, Oct. 2006.

[36] M. Alvarez and L. M. Lechuga, 'Microcantilever-based platforms as biosensing tools', *The Analyst*, vol. 135, no. 5, p. 827, 2010.

[37] P. Dextras, K. R. Payer, T. P. Burg, W. Shen, Y.-C. Wang, J. Han, and S. R. Manalis, 'Fabrication and Characterization of an Integrated Microsystem for Protein Preconcentration and Sensing', *J. Microelectromechanical Syst.*, vol. 20, no. 1, pp. 221–230, Feb. 2011.

[38] M. F. Khan, S. Kim, D. Lee, S. Schmid, A. Boisen, and T. Thundat, 'Nanomechanical identification of liquid reagents in a microfluidic channel', *Lab. Chip*, vol. 14, no. 7, pp. 1302–1307, 2014.

[39] M. J. Madou, *Manufacturing Techniques for Microfabrication and Nanotechnology*. CRC Press, 2011.

[40] D. Nilsson, S. Jensen, and A. Menon, 'Fabrication of silicon molds for polymer optics', *J. Micromechanics Microengineering*, vol. 13, no. 4, p. S57, 2003.

[41] A. del Campo and C. Greiner, 'SU-8: a photoresist for high-aspect-ratio and 3D submicron lithography', *J. Micromechanics Microengineering*, vol. 17, no. 6, p. R81, Jun. 2007.

[42] S. Belligundu and P. S. Shiakolas, 'Study on two-stage hot embossing microreplication: silicon to polymer to polymer', *J. MicroNanolithography MEMS MOEMS*, vol. 5, no. 2, pp. 021103–021103–8, 2006.

[43] J. Chae, S. S. Park, and T. Freiheit, 'Investigation of micro-cutting operations', *Int. J. Mach. Tools Manuf.*, vol. 46, no. 3–4, pp. 313–332, Mar. 2006.

[44] P. Couceiro, S. G. Pedro, and J. Alonso-Chamarro, 'All-ceramic analytical microsystems with monolithically integrated optical detection microflow cells', *Microfluid. Nanofluidics*, pp. 1–8, Aug. 2014.

[45] C. K. Malek and V. Saile, 'Applications of LIGA technology to precision manufacturing of high-aspect-ratio micro-components and -systems: a review', *Microelectron. J.*, vol. 35, no. 2, pp. 131–143, Feb. 2004.

[46] T. P. Burg, A. R. Mirza, N. Milovic, C. H. Tsau, G. A. Popescu, J. S. Foster, and S. R. Manalis, 'Vacuum-Packaged Suspended Microchannel Resonant Mass Sensor for Biomolecular Detection', *J. Microelectromechanical Syst.*, vol. 15, no. 6, pp. 1466–1476, Dec. 2006.

[47] J. Llobet, M. Sansa, M. Gerbolés, N. Mestres, J. Arbiol, X. Borrisé, and F. Pérez-Murano, 'Enabling electromechanical transduction in silicon nanowire mechanical resonators fabricated by focused ion beam implantation', *Nanotechnology*, vol. 25, no. 13, p. 135302, Apr. 2014.

[48] C. A. Volkert and A. M. Minor, 'Focused Ion Beam Microscopy and Micromachining', *MRS Bull.*, vol. 32, no. 05, pp. 389–399, May 2007.

[49] X. Jing, D. Chen, D. Fang, C. Huang, J. Liu, and X. Chen, 'Multi-layer microstructure fabrication by combining bulk silicon micromachining and UV-LIGA technology', *Microelectron. J.*, vol. 38, no. 1, pp. 120–124, Jan. 2007.

[50] T. Betancourt and L. Brannon-Peppas, ‘Micro- and nanofabrication methods in nanotechnological medical and pharmaceutical devices’, *Int. J. Nanomedicine*, vol. 1, no. 4, pp. 483–495, Dec. 2006.
[51] M. Sahli, C. Millot, J.-C. Gelin, and T. Barrière, ‘The manufacturing and replication of microfluidic mould inserts by the hot embossing process’, *J. Mater. Process. Technol.*, vol. 213, no. 6, pp. 913–925, Jun. 2013.
[52] R. K. Jena, C. Y. Yue, Y. C. Lam, P. S. Tang, and A. Gupta, ‘Comparison of different molds (epoxy, polymer and silicon) for microfabrication by hot embossing technique’, *Sens. Actuators B Chem.*, vol. 163, no. 1, pp. 233–241, Mar. 2012.
[53] H. Becker and U. Heim, ‘Hot embossing as a method for the fabrication of polymer high aspect ratio structures’, *Sens. Actuators Phys.*, vol. 83, no. 1–3, pp. 130–135, May 2000.
[54] J. L. Moore, A. McCuiston, I. Mittendorf, R. Ottway, and R. D. Johnson, ‘Behavior of capillary valves in centrifugal microfluidic devices prepared by three-dimensional printing’, *Microfluid. Nanofluidics*, vol. 10, no. 4, pp. 877–888, Apr. 2011.
[55] V. A. Lifton, G. Lifton, and S. Simon, ‘Options for additive rapid prototyping methods (3D printing) in MEMS technology’, *Rapid Prototyp. J.*, vol. 20, no. 5, pp. 403–412, Aug. 2014.
[56] S. D. Gittard and R. J. Narayan, ‘Laser direct writing of micro- and nano-scale medical devices’, *Expert Rev. Med. Devices*, vol. 7, no. 3, pp. 343–356, May 2010.
[57] C. Accoto, A. Qualtieri, F. Pisanello, C. Ricciardi, C. F. Pirri, M. De Vittorio, and F. Rizzi, ‘Two-Photon Polymerization Lithography and Laser Doppler Vibrometry of a SU-8-Based Suspended Microchannel Resonator’, *J. Microelectromechanical Syst.*, vol. PP, no. 99, pp. 1–1, 2015.
[58] C. Sun, N. Fang, D. M. Wu, and X. Zhang, ‘Projection micro-stereolithography using digital micro-mirror dynamic mask’, *Sens. Actuators Phys.*, vol. 121, no. 1, pp. 113–120, May 2005.
[59] A. A. Trusov and A. M. Shkel, ‘Capacitive detection in resonant MEMS with arbitrary amplitude of motion’, *J. Micromechanics Microengineering*, vol. 17, no. 8, p. 1583, 2007.
[60] X. Huang, S. Li, J. Schultz, Q. Wang, and Q. Lin, ‘A Capacitive MEMS Viscometric Sensor for Affinity Detection of Glucose’, *J. Microelectromechanical Syst.*, vol. 18, no. 6, pp. 1246–1254, Dec. 2009.
[61] J. W. Song, J.-S. Lee, J.-E. An, and C. G. Park, ‘Design of a MEMS piezoresistive differential pressure sensor with small thermal hysteresis for air data modules’, *Rev. Sci. Instrum.*, vol. 86, no. 6, p. 065003, Jun. 2015.
[62] L. Zhao, L. Xu, G. Zhang, Z. Jiang, Y. Zhao, J. Wang, X. Wang, and Z. Liu, ‘In-Situ Measurement of Fluid Density Rapidly Using a Vibrating Piezoresistive Microcantilever Sensor Without Resonance Occurring’, *IEEE Sens. J.*, vol. 14, no. 3, pp. 645–650, Mar. 2014.
[63] J. Lee, R. Chunara, W. Shen, K. Payer, K. Babcock, T. P. Burg, and S. R. Manalis, ‘Suspended microchannel resonators with piezoresistive sensors’, *Lab Chip*, vol. 11, no. 4, pp. 645–651, 2010.
[64] D. Fariña, M. Álvarez, S. Márquez, C. Domínguez, and L. M. Lechuga, ‘Out-of-plane single-mode photonic microcantilevers for integrated nanomechanical sensing platform’, *Sens. Actuators B Chem.*, vol. 232, pp. 60–67, Sep. 2016.
[65] W. W. Koelmans, J. van Honschoten, J. de Vries, P. Vettiger, L. Abelmann, and M. C. Elwenspoek, ‘Parallel optical readout of cantilever arrays in dynamic mode’, *Nanotechnology*, vol. 21, no. 39, p. 395503, Oct. 2010.
[66] W. K. Hiebert, D. Vick, V. Sauer, and M. R. Freeman, ‘Optical interferometric displacement calibration and thermomechanical noise detection in bulk focused ion beam-fabricated nanoelectromechanical systems’, *J. Micromechanics Microengineering*, vol. 20, no. 11, p. 115038, Nov. 2010.

[67] D. Karabacak, T. Kouh, and K. L. Ekinci, ‘Analysis of optical interferometric displacement detection in nanoelectromechanical systems’, *J. Appl. Phys.*, vol. 98, no. 12, p. 124309, Dec. 2005.
[68] R. B. Karabalin, S. C. Masmanidis, and M. L. Roukes, ‘Efficient parametric amplification in high and very high frequency piezoelectric nanoelectromechanical systems’, *Appl. Phys. Lett.*, vol. 97, no. 18, pp. 183101–183101–3, Nov. 2010.
[69] A. S. Sadek, R. B. Karabalin, J. Du, M. L. Roukes, C. Koch, and S. C. Masmanidis, ‘Wiring Nanoscale Biosensors with Piezoelectric Nanomechanical Resonators’, *Nano Lett*, vol. 10, no. 5, pp. 1769–1773, 2010.
[70] M. D. LaHaye, ‘Approaching the Quantum Limit of a Nanomechanical Resonator’, *Science*, vol. 304, no. 5667, pp. 74–77, Apr. 2004.
[71] L. G. Villanueva, R. B. Karabalin, M. H. Matheny, E. Kenig, M. C. Cross, and M. L. Roukes, ‘A Nanoscale Parametric Feedback Oscillator’, *Nano Lett.*, vol. 11, no. 11, pp. 5054–5059, Oct. 2011.
[72] S.-H. ”Shawn” Lim, D. Raorane, S. Satyanarayana, and A. Majumdar, ‘Nano-chemo-mechanical sensor array platform for high-throughput chemical analysis’, *Sens. Actuators B Chem.*, vol. 119, no. 2, pp. 466–474, Dec. 2006.
[73] O. N. Tufte, P. W. Chapman, and D. Long, ‘Silicon Diffused-Element Piezoresistive Diaphragms’, *J. Appl. Phys.*, vol. 33, no. 11, pp. 3322–3327, Nov. 1962.
[74] C. A. J. Putman, B. G. De Grooth, N. F. Van Hulst, and J. Greve, ‘A detailed analysis of the optical beam deflection technique for use in atomic force microscopy’, *J. Appl. Phys.*, vol. 72, no. 1, pp. 6–12, Jul. 1992.
[75] D. Karabacak, T. Kouh, and K. L. Ekinci, ‘Analysis of optical interferometric displacement detection in nanoelectromechanical systems’, *J. Appl. Phys.*, vol. 98, no. 12, p. 124309, Dec. 2005.
[76] K. Takahashi, H. Oyama, N. Misawa, K. Okumura, M. Ishida, and K. Sawada, ‘Surface stress sensor using MEMS-based Fabry–Perot interferometer for label-free biosensing’, *Sens. Actuators B Chem.*, vol. 188, pp. 393–399, Nov. 2013.
[77] V. Agache, G. Blanco-Gomez, F. Baleras, and P. Caillat, ‘An embedded microchannel in a MEMS plate resonator for ultrasensitive mass sensing in liquid’, *Lab. Chip*, vol. 11, no. 15, pp. 2598–2603, Aug. 2011.
[78] M. Heinisch, T. Voglhuber-Brunnmaier, E. K. Reichel, I. Dufour, and B. Jakoby, ‘Electromagnetically driven torsional resonators for viscosity and mass density sensing applications’, *Sens. Actuators Phys.*, vol. 229, pp. 182–191, Jun. 2015.
[79] G. Blanco-Gomez and V. Agache, ‘Experimental Study of Energy Dissipation in High Quality Factor Hollow Square Plate MEMS Resonators for Liquid Mass Sensing’, *J. Microelectromechanical Syst.*, vol. 21, no. 1, pp. 224–234, Feb. 2012.
[80] J. Lee and W. P. King, ‘Microcantilever actuation via periodic internal heating’, *Rev. Sci. Instrum.*, vol. 78, no. 12, p. 126102, Dec. 2007.
[81] D. Rugar and P. Grütter, ‘Mechanical parametric amplification and thermomechanical noise squeezing’, *Phys. Rev. Lett.*, vol. 67, no. 6, pp. 699–702, Aug. 1991.
[82] S. A. Miller, K. L. Turner, and N. C. MacDonald, ‘Microelectromechanical scanning probe instruments for array architectures’, *Rev. Sci. Instrum.*, vol. 68, no. 11, pp. 4155–4162, Nov. 1997.
[83] J. Brugger, N. Blanc, P. Renaud, and N. F. de Rooij, ‘Microlever with combined integrated sensor/actuator functions for scanning force microscopy’, *Sens. Actuators Phys.*, vol. 43, no. 1, pp. 339–345, May 1994.

[84] J. P. Davis, D. Vick, D. C. Fortin, J. a. J. Burgess, W. K. Hiebert, and M. R. Freeman, 'Nanotorsional resonator torque magnetometry', *Appl. Phys. Lett.*, vol. 96, no. 7, p. 072513, Feb. 2010.

[85] W. Han, S. M. Lindsay, and T. Jing, 'A magnetically driven oscillating probe microscope for operation in liquids', *Appl. Phys. Lett.*, vol. 69, no. 26, pp. 4111–4113, Dec. 1996.

[86] I. Lee and J. Lee, 'Measurement uncertainties in resonant characteristics of MEMS resonators', *J. Mech. Sci. Technol.*, vol. 27, no. 2, pp. 491–500, Mar. 2013.

[87] T. P. Burg and S. R. Manalis, 'Suspended microchannel resonators for biomolecular detection', *Appl. Phys. Lett.*, vol. 83, no. 13, pp. 2698–2700, Sep. 2003.

[88] T. P. Burg, M. Godin, S. M. Knudsen, W. Shen, G. Carlson, J. S. Foster, K. Babcock, and S. R. Manalis, 'Weighing of biomolecules, single cells and single nanoparticles in fluid', *Nature*, vol. 446, no. 7139, pp. 1066–1069, Apr. 2007.

[89] J. Lee, A. K. Bryan, and S. R. Manalis, 'High precision particle mass sensing using microchannel resonators in the second vibration mode', *Rev. Sci. Instrum.*, vol. 82, no. 2, p. 023704, Feb. 2011.

[90] M. Godin, F. F. Delgado, S. Son, W. H. Grover, A. K. Bryan, A. Tzur, P. Jorgensen, K. Payer, A. D. Grossman, M. W. Kirschner, and S. R. Manalis, 'Using buoyant mass to measure the growth of single cells', *Nat. Methods*, vol. 7, no. 5, pp. 387–390, May 2010.

[91] W. H. Grover, A. K. Bryan, M. Diez-Silva, S. Suresh, J. M. Higgins, and S. R. Manalis, 'Measuring single-cell density', *Proc. Natl. Acad. Sci.*, Jun. 2011.

[92] A. K. Bryan, V. C. Hecht, W. Shen, K. Payer, W. H. Grover, and S. R. Manalis, 'Measuring single cell mass, volume, and density with dual suspended microchannel resonators', *Lab. Chip*, vol. 14, no. 3, pp. 569–576, Dec. 2013.

[93] J. Lee, W. Shen, K. Payer, T. P. Burg, and S. R. Manalis, 'Toward Attogram Mass Measurements in Solution with Suspended Nanochannel Resonators', *Nano Lett*, vol. 10, no. 7, pp. 2537–2542, 2010.

[94] R. A. Barton, B. Ilic, S. S. Verbridge, B. R. Cipriany, J. M. Parpia, and H. G. Craighead, 'Fabrication of a Nanomechanical Mass Sensor Containing a Nanofluidic Channel', *Nano Lett*, vol. 10, no. 6, pp. 2058–2063, 2010.

[95] J. E. Sader, T. P. Burg, and S. R. Manalis, 'Energy Dissipation in Microfluidic Beam Resonators', *J. Fluid Mech.*, vol. 650, pp. 215–250, 2010.

[96] J. E. Sader, T. P. Burg, J. Lee, and S. R. Manalis, 'Energy dissipation in microfluidic beam resonators: Effect of Poisson's ratio', *Phys. Rev. E*, vol. 84, no. 2, p. 026304, Aug. 2011.

[97] I. Lee, K. Park, and J. Lee, 'Note: Precision viscosity measurement using suspended microchannel resonators', *Rev. Sci. Instrum.*, vol. 83, no. 11, p. 116106, Nov. 2012.

[98] G. Blanco-Gomez and V. Agache, 'Experimental Study of Energy Dissipation in High Quality Factor Hollow Square Plate MEMS Resonators for Liquid Mass Sensing', *J. Microelectromechanical Syst.*, vol. 21, no. 1, pp. 224–234, Feb. 2012.

[99] M. F. Khan, S. Schmid, Z. J. Davis, S. Dohn, and A. Boisen, 'Fabrication of resonant micro cantilevers with integrated transparent fluidic channel', *Microelectron. Eng.*, vol. 88, no. 8, pp. 2300–2303, Aug. 2011.

[100] M. F. Khan, S. Kim, D. Lee, S. Schmid, A. Boisen, and T. Thundat, 'Nanomechanical identification of liquid reagents in a microfluidic channel', *Lab. Chip*, vol. 14, no. 7, pp. 1302–1307, Mar. 2014.

[101] G. Vidal-Álvarez, E. Marigó, F. Torres, and N. Barniol, 'Fabrication and Measurement of a Suspended Nanochannel Microbridge Resonator Monolithically Integrated with CMOS Readout Circuitry', *Micromachines*, vol. 7, no. 3, p. 40, Mar. 2016.

[102] M. M. Modena, Y. Wang, D. Riedel, and T. P. Burg, ‘Resolution enhancement of suspended microchannel resonators for weighing of biomolecular complexes in solution’, *Lab. Chip*, vol. 14, no. 2, pp. 342–350, Jan. 2014.

[103] Y. Wang, M. M. Modena, M. Platen, I. A. T. Schaap, and T. P. Burg, ‘Label-Free Measurement of Amyloid Elongation by Suspended Microchannel Resonators’, *Anal. Chem.*, vol. 87, no. 3, pp. 1821–1828, Feb. 2015.

[104] D. Westberg, O. Paul, G. I. Andersson, and H. Baltes, ‘A CMOS-compatible device for fluid density measurements’, in , *Tenth Annual International Workshop on Micro Electro Mechanical Systems, 1997. MEMS ’97, Proceedings, IEEE*, 1997, pp. 278–283.

[105] P. A. Rasmussen, J. Thaysen, O. Hansen, S. C. Eriksen, and A. Boisen, ‘Optimised cantilever biosensor with piezoresistive read-out’, *Ultramicroscopy*, vol. 97, no. 1–4, pp. 371–376, Oct. 2003.

[106] J. L. Arlett and M. L. Roukes, ‘Ultimate and practical limits of fluid-based mass detection with suspended microchannel resonators’, *J. Appl. Phys.*, vol. 108, no. 8, pp. 084701–084701–11, Oct. 2010.

Chapter 2 Design and Simulation of HMB devices

In many engineering areas, finite element analysis constitutes a versatile tool to model the physics involved in a given application. The aim of finite element methods (FEM) is to find an approximate solution of a system by a set of differential equations and boundary conditions. The differential equations involved in the model can be represented by finite elements that mesh the geometry of the application. In simple terms, the model is represented by a linear approximation to obtain a matrix of the form $Ax = b$, where the vector solution x is elucidated using direct solving methods. In the field of MEMS, numerical simulations can substantially aid at early design stages of new sensors to estimate and optimize their response. This is particularly useful for complex designs that conventionally use bending and torsional translations of thin-film structures for mass sensing applications. In this way, the time gap for their design and development can effectively be shorten.

The intention of this chapter is to exploit the benefits of FEM in the design and development of the HMB resonators. To understand the physics of our devices, we start by describing the resonant properties of the devices using lumped parameter modelling. To perform the FEM simulations of HMB devices, we have used Comsol Multiphysics software. Comsol contains several methods to solve differential equations and integrate multiphysics models such as solid mechanics, fluidic behaviours, electromagnetic waves, thermal and acoustic effects, among others. In this way, the characteristic matrix of the problem that involves several physics can be linearized to find an optimum solution. FEM simulations are employed to calculate the structural mechanics behaviour and to know the conditions to determine the frequency response, mass responsivity and elastic constant of the proposed design of resonators according to their dimensions. Specifically, we study the effect of the cross-section area, length and sidewall thickness on the dimensions of the microchannel with the objective of injecting solutions of different densities and viscosities. Next, by integrating additional multiphysics models, we have also analysed the governing flow dynamics inside the microchannels and the effect of the hydrostatic pressure along the sidewalls. Finally, a comparison of 2D and 3D models is performed to evaluate the transport of fluids inside the microchannels through two filling schemes: in-line and H-shaped.

2.1 Physics and dynamic mode response of vibrating structures

2.1.1 Resonant frequency

The most representative parameters when a vibrating structure is under dynamic response are its fundamental resonance frequency and quality factor. The resonance frequency of a beam indicates that the structure is oscillating around its equilibrium point while an external force excites it into resonance. The quality factor is a parameter that shows the ratio of the stored to dissipated energy in one oscillation cycle. The dynamic behaviour of an oscillating micromechanical structure can be generally approach to a damped harmonic oscillator model in which the natural frequency (ω_0) is defined as,

$$\omega_0^2 = \frac{k}{m} \qquad \text{Eq. 2.1}$$

where k is the elastic constant and m is the mass of the resonator. If a time-periodic force $F_0 e^{i\omega_r t}$ with maximum amplitud F_0 and angular frequency ω_r is applied to drive the response of the resonator into resonance, the displacement of the structure can be described by the following differential equation,

$$m\frac{d^2\mathcal{U}_z}{dt^2} + \varsigma\frac{d\mathcal{U}_z}{dt} + k\mathcal{U}_z = F_0 e^{i\omega_r t} \qquad \text{Eq. 2.2}$$

where $\mathcal{U}_z$ is the displacement function with respect to the equilibrium point and ς is the damping factor. Generally, a proposed solution for Eq. 2.2 has the following form,

$$\mathcal{U}_z(t) = \mathcal{U}_0(\omega) e^{i(\omega t - \phi)} \qquad \text{Eq. 2.3}$$

where $\mathcal{U}_0$ is the amplitude of oscillation and ϕ is the oscillation phase. By substituting the proposed solution into Eq. 2.2 we obtain,

$$\mathcal{U}_0(\omega) = \frac{F_0/m}{\sqrt{(\omega_0^2 - \omega^2)^2 + (2\gamma\omega)^2}} \qquad \text{Eq. 2.4}$$

$$\phi = arctan\left(\frac{2\gamma\omega}{\omega_0^2 - \omega^2}\right) \qquad \text{Eq. 2.5}$$

where $\gamma = \varsigma/2m$. From Eq. 2.4, the maximum oscillation amplitude $\mathcal{U}_0$ is obtained when,

$$\omega^2 = \omega_0^2 - 2\gamma^2 \qquad \text{Eq. 2.6}$$

It can be observed that the driven excitation frequency cannot be equal to the natural frequency of the resonator because of the damping force γ. Fig. 2–1 shows the response of Eq. 2.4 to various values of the damping force. The amplitude of oscillation of the system becomes infinite for ideal cases in which damping forces are not considered. However, when the system is subject to real conditions, the amplitude of the system is maximized for frequency values close to the natural frequency of the resonator. Thus the maximum amplitude of oscillation can be defined as:

$$A_{max} = \frac{F_0/m}{2\gamma\sqrt{\omega_0^2 - \gamma^2}} \qquad \text{Eq. 2.7}$$

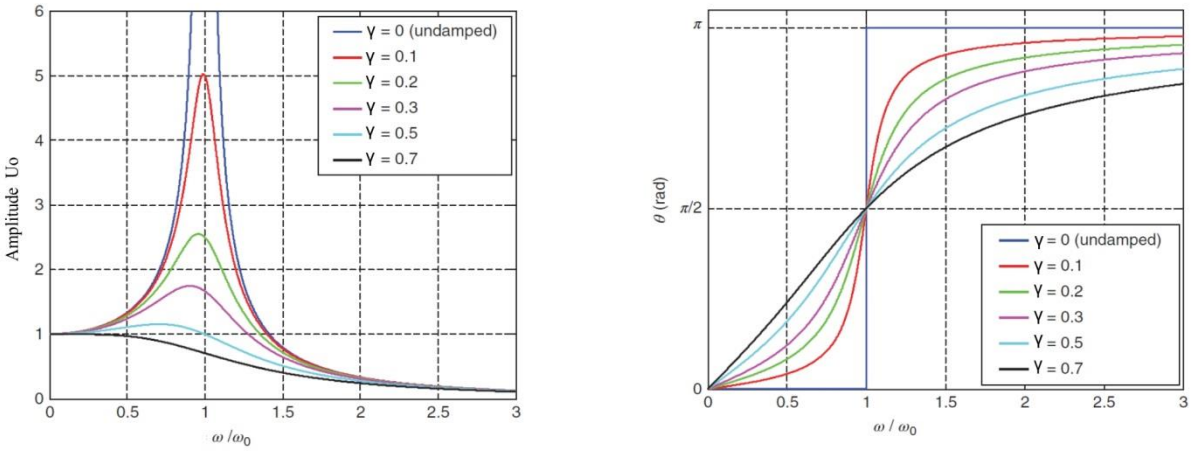

a) b)

Fig. 2–1. a) Amplitude of oscillation of a vibrating system as a function of the ratio ω/ω_0 for different damping coefficients γ. Resonance is exhibited as the frequency of the excitation signal is close to the natural frequency of the system, but is not driven to infinite because of the damping factor. b) The phase response of the system when the system is on resonance for various damping coefficients.

As follows, to obtain the equation of motion of a doubly clamped beam, the method of dynamic equilibrium is applied taking into consideration that the shear forces of the structure are negligible. From the dynamic Euler-Bernoulli theory, the displacement function of a beam with elastic constant (k), Young modulus (E) and second moment of inertia (I) [1], is a differential equation of fourth order given by,

$$EI\frac{d^4\mathcal{U}_z(x,t)}{dx^4}+\mu\frac{d^2\mathcal{U}_z(x,t)}{dt^2}=0 \qquad \text{Eq. 2.8}$$

where μ is the mass per unit length and $\mathcal{U}_z(x,t)$ is the displacement function of the beam in the z-direction, *x* is the spatial coordinate along the length of the beam and *t* is the time. Since the above equation is dependant over time and position, it is not easy to be solved by conventional methods and thus a variable separation methodology is mandatory. The equation can be solved by proposing a solution of the form $\mathcal{U}_z(x,t) = u(x)\,cos(\omega_n t + \theta)$ and by establishing the proper boundary conditions. By substituting the proposed solution into Eq. 2.8 we obtain,

$$EI\frac{d^4u(x)}{dx^4}\pm\mu\omega_n^2\,u(x)=0 \qquad \rightarrow \qquad \frac{d^4u(x)}{dx^4}=\pm\frac{\mu}{EI}\,\omega_n^2\,u(x) \qquad \text{Eq. 2.9}$$

For a doubly clamped beam, the corresponding boundary conditions are:

$$\left[\mathcal{U}_z(x,t)=\frac{\partial\mathcal{U}_z(x,t)}{\partial x}\right]_{x=0}=\left[\mathcal{U}_z(x,t)=\frac{\partial\mathcal{U}_z(x,t)}{\partial x}\right]_{x=L}=0 \qquad \text{Eq. 2.10}$$

Solving Eq. 2.9 to obtain the frequency response of the beam taking into account the boundary conditions of Eq. 2.10, leads to the following result for vacuum resonant frequencies [1],

$$\omega_n=\frac{C_n^2}{L^2}\sqrt{\frac{EI}{\mu}} \qquad \text{Eq. 2.11}$$

where n = 1, 2, ... is the mode order and $C_n$is the n^{th} positive root (eigenvalues) satisfying:

$$-1+cosC_n coshC_n=0 \qquad \text{Eq. 2.12}$$

For mode numbers where $n>1$ [1], the eigenvalues can be well approximated by $C_n\approx(n+1/2)\pi$. Thus, for a doubly clamped beam with uniform rectangular cross section $I=bh^3/12$ and $\mu=\rho bh$, where ρ is the beam density, we have the following first frequency bending mode:

$$\omega_n = \frac{C_n^2 h}{L^2}\sqrt{\frac{E}{12\rho}} \quad \Rightarrow \quad \omega_1 = \frac{4.73^2 h}{L^2}\sqrt{\frac{E}{12\rho}} \qquad \text{Eq. 2.13}$$

2.1.2 Quality factor

The quality factor Q expresses the ratio between the stored energy and the dissipated energy in one oscillation cycle of a mechanical or electronic system as stated by the following equation $Q = 2\pi \cdot E_{stored}/E_{diss}$. The Q-factor can also be defined as the relationship between the natural frequency of the resonator in respect of a frequency bandwidth determined by a 3dB decay of the maximum magnitude of the frequency spectrum, as shown in Fig. 2–2. Besides, the Q-factor determines the quality of oscillation of a vibrating structure. When the Q-factor increases, a higher resolution can be achieved by the system; for this reason, intensive efforts have been dedicated to optimizing this parameter for the design of efficient MEMS devices. Furthermore, energy losses of the system can also be evaluated by the Q-factor regarding both internal and external dissipation mechanisms,

$$\frac{1}{Q} = \sum \frac{1}{Q_i} = \frac{1}{Q_{int}} + \frac{1}{Q_{ext}} \qquad \text{Eq. 2.14}$$

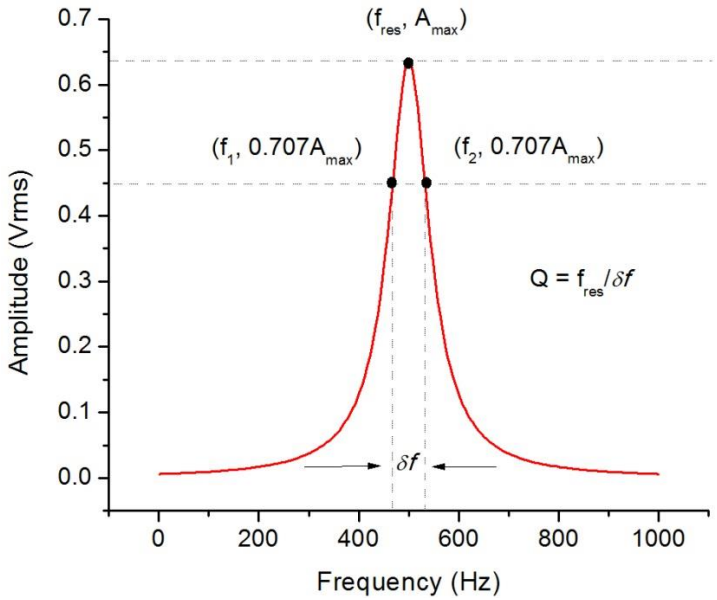

Fig. 2–2. Estimation of the Q-factor of vibrating structures using the driven frequency spectrum response. The Q-factor defines the quality of oscillation as a function of the width of the spectrum around the natural frequency of the resonator. Hence the importance of improving the frequency resolution of systems wherein the frequency shifts are transduced into mass changes for mass sensing applications.

The internal dissipation mechanisms that affect the overall Q-factor of the system are related to intrinsic properties of the resonator such as its structure, fabrication and composition. Meanwhile, the exterior mechanics are basically dominated by viscous drag of the surrounding environment. For instance, the Q-factor of resonators can severely be undermined when working under dynamic operational mode in viscous environments, such as liquids. As a result, the ample Q-factor will affect the frequency resolution of the system.

2.2 Physics and dynamic mode response of HMB devices

2.2.1 Resonant properties

According to the Euler-Bernoulli beam theory, the frequency behaviour of a doubly clamped beam with an embedded microchannel can also be modelled as a lump-parameter resonator. The model is valid under the following assumptions: 1) material composition of resonators is uniformly distributed along the structures, and the cross-section geometry of microchannels is constant; 2) fluid filling of embedded microchannels does not change the elastic constant of resonators; and, 3) shearing deformation of doubly clamped beams is negligible. For low-damping values, the driven frequency response of a resonator (ω_r) can be approximated to its natural frequency (ω_0), as $\omega_r \approx \omega_o$. Then, the bending resonant frequency of a linear resonator with elastic constant (k_b) and effective mass (m_b) is,

$$\omega_r{}^2 = \frac{k_b}{m_b} \qquad \text{Eq. 2.15}$$

Here, the elastic constant is defined as $k_b = 192(EI)/L^3$ where E is the Young Modulus, $I = bh^3/12$ is the moment of inertia with respect to "x" axis being b, h and L the width height and length of the beam, respectively. The total effective mass of the resonator is a contribution of not only the structural material but also of the added mass induced by the sample fluid. For this reason, we modelled the resonators as a multimorph doubly clamped beam constituted by equal length layers in which the effective mass is defined as [2],

$$m_b = \frac{26}{70} L \sum_{i=1}^{n} \rho_i A_i \qquad \text{Eq. 2.16}$$

where ρ_i is the density of the layer "i" with its corresponding cross-sectional area A_i. By substituting the lumped parameter definitions of k_b and m_b into Eq. 2.15 the approximated first bending resonant frequency of a HMB resonator is then,

$$f_{r,b} = \frac{22.736\, h_b}{2\pi L^2}\sqrt{\frac{E}{12[\alpha\rho_f + (1-\alpha)\rho_b]}} \qquad \text{Eq. 2.17}$$

where ρ_b and ρ_f are the structural material and sample fluid densities, respectively. The parameter α is the ratio of microfluidic channel surface to beam cross-sectional area defined as $\alpha = w_f h_f / w_b h_b$, being w_f and h_f, the width and height of the embedded microchannel, and w_b and h_b, the width and height of the beam, respectively. By monitoring the HMB resonant frequency response in the time domain, we correlated the frequency changes as a function of the target fluid density.

2.2.2 Quality factor

In HMB devices, the dissipation of energy is mainly attributed to shearing of the contained fluid that can freely move inside the channel. Besides, as damping is a non-monotonic function of the sample viscosity inside of the resonators with the internal microchannels [6], the Q-factor value can increase or decrease with respect to sample viscosity [7]. In our device, since the embedded microchannel is designed to be centered about the beam neutral axis, the magnitude of the shearing effect can be determined by the dimensionless frequency number,

$$\beta = \frac{\rho_{fluid}\omega h_{fluid}^2}{\mu} \qquad \text{Eq. 2.18}$$

where h_{fluid} is the channel height, μ is the dynamic viscosity, ρ_{fluid} is the fluid density and ω is the resonant frequency. For the first operational mode of resonators, the β number defines two flow transition regimes at the minimum ($\beta = 46$) of the following non-monotonic function [6],

$$F(\beta) \approx 0.152\sqrt{\beta} + 38.7/\beta \qquad \text{Eq. 2.19}$$

As depicted in Fig. 2–3, for $\beta < 46$, there is a low-inertia regime while for $\beta > 46$ fluid inertia dominates. Once the dimensionless frequency number is defined, the shear loss (Q_{shear}) in HMB devices can be modelled according to the β number, the properties of the contained fluid and the dimensions of the microchannels. The energy dissipation of a HMB device can be approximated to that of a cantilever SMR device [6] with length L, thickness h_c, and width w_c containing a microchannel with dimensions h_f and w_f as,

$$Q_{shear} \approx \left(0.152\sqrt{\beta} + \frac{38.7}{\beta}\right)\left(\frac{\rho_c}{\rho_f}\right)\left(\frac{h_c}{h_f}\right)\left(\frac{w_c}{w_f}\right)\left(\frac{L}{h_f}\right)^2 \qquad \text{Eq. 2.20}$$

In this way, the shearing loss for a HMB device with $\rho_c = 2320\ \mathrm{Kg/m^3}$, $\rho_f = 1000\ \mathrm{Kg/m^3}$, $w_c = 12\ \mu m$, $h_c = 6\ \mu m$, $L = 280\ \mu m$, $h_f = 4\ \mu m$ and $w_f = 10\ \mu m$ and operating in the low inertia regime ($\beta = 31.81$) can yield an estimated value of $Q_{shear} = 37649.42$. This indicates that the contribution of the fluid shear in our devices can be ignored given that the shear-limited Q-

factor ($\sim 4 \times 10^5$) is four orders of magnitude higher than the expected Q-factor of HMB devices (up to 600). In practical terms, the major dissipation of energy that can exhibit a resonator with an internal microchannel of any topology is limited by the viscosity of the contained fluid and in the ability to pump inside samples with higher viscosities. By tracking the quality factor of the HMB resonators while streaming different fluids, we analysed the sensor response to the viscosity changes in the low-inertia regime.

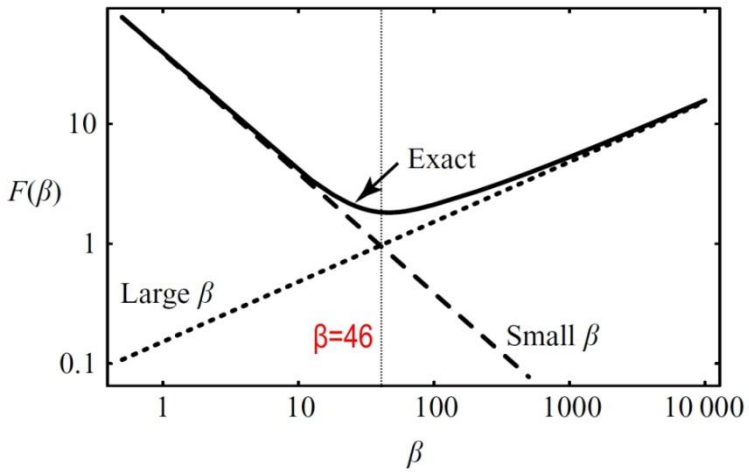

Fig. 2–3. The non-monotonic function F(β) establishes two flow transitions regimes at its minimum to understand the effect of the energy dissipation of SMR devices as a function of the density and viscosity of the sample fluid [6].

2.2.3 Mass responsivity

Similar to the behaviour and response of vibrating microcantilevers, the mass responsivity of a hollowed microchannel can depend on the geometry, resonance frequency and vibrational mode of the resonator. When changes in the elastic constant of the resonator are considered negligible, the mass responsivity of HMB devices can be expressed as a function of the added mass to the total mass of the sensor according to the following expression [3],

$$\frac{\Delta\,\omega}{\omega_0} \approx -\frac{1}{2}\frac{\Delta m}{m_{eff}} \qquad \text{Eq. 2.21}$$

here $m_{eff} = m_f + m_s$ is the effective mass of the sensor that results from the sum of the fluid and sensor masses. In terms of the density change, the Eq. 2.21 can be rewritten as follows [4],

$$\frac{\Delta\,\omega}{\omega_0} \approx -\frac{1}{2}\frac{[\Delta\rho_f HW]L}{[\rho_f HW + 2t\rho_s(H+W+2t)]L} \qquad \text{Eq. 2.22}$$

where H, W, and L are the height, width and length of the microchannel, t is the wall thickness of the resonator and ρ_f and ρ_s the density of the fluid and resonator, respectively. The reduced form of equation Eq. 2.22 is given as follows [4],

$$\frac{\Delta\,\omega}{\omega_0} \approx -\frac{1}{2}\frac{\Delta\rho_f}{\rho_f}\frac{1}{(A_s/A_f)(\rho_s/\rho_f)+1} \qquad \text{Eq. 2.23}$$

A_s and A_f are the cross section surface of the solid structure and fluidic channel, respectively. For the design of HMB devices, we considered long and thin microchannels such that t << W. In here, the microchannel width "W" does not specifically influences on the optimization of the ratio A_s/A_f. Instead, the microchannel width is limited by other factors such as the actuation and acquisition methods to obtain the resonance frequency response of the beams. For instance, if an optical detection method is used, the laser beam that is reflected back from the top surface of the resonator will have fewer diffraction effects if the width of the resonator is higher than the beam spot size. Furthermore, the width of the microchannels determines the rigidity and robustness of the structures. For example, a wider beam will yield higher rigidity and thus will exhibit low dynamic range displacement when driven into resonance. On the contrary, a narrower microchannel will exhibit a higher dynamic range, but it will be more susceptible to mechanical failures because of the higher amplitude displacements.

Thus, to maximize the shift on the resonance frequency response of the HMB devices with respect to the changes in the fluid density of the sample solution, the channel mass per unit length should be minimized to optimize sensitivity [5]. In other words, the ratio of mass per unit length of the fluid to the mass per unit length of the resonator structure should be minimized, A_s/A_f. To better explain this assumption, we considered the two configurations of microchannels shown in Fig. 2–4. In the first configuration, the ratio A_s/A_f is greater than the unity given that the cross sectional area of the structures is higher than that of the fluid. In this case, the sensor is mainly constituted by the structural material and thus sensitivity gains are marginal at this point because the device mass is dominated by the mass of the solid structure. On the contrary, in the second configuration $A_s/A_f < 1$, the sensitivity gain increases given that the mass of the sensor is mainly constituted by the sample fluid. In consequence, to maximize the responsivity of the sensor it is convenient to study the height of the microchannels and also the thickness of the channel walls in terms of the dimensions that can be reproduced during the fabrication of the sensor. For example, layer thicknesses in the range of a few nanometres can be deposited using microfabrication techniques to reduce the depth of the microchannels. However, the fluidic resistance of the microchannels will become higher increasing the chances of clogging.

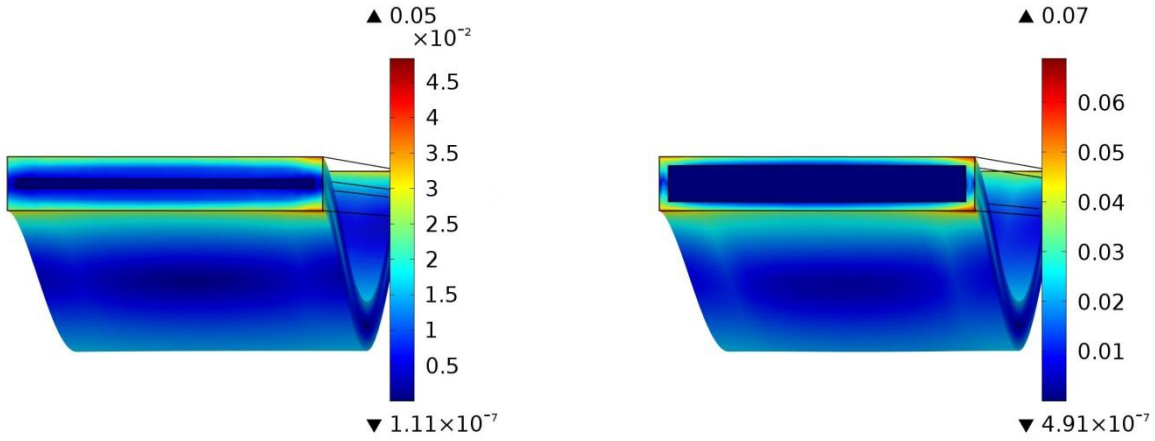

$A_s/A_f > 1$ $A_s/A_f < 1$

Fig. 2–4. The mass responsivity of HMB devices relies on minimizing the ratio of mass per unit length of the contained fluid with respect to the mass per unit length of the resonator structure.

2.2.4 Proposed design of the device

A prerequisite to start the design of the HMB devices was to select the morphology of the microchannels. Conventionally, the fabrication of suspended microchannels can be done based on three different approaches: a) the microchannels can protrude out from the substrate conforming a 3D topology; b) they can be buried into trenches outlined into the substrate and finally c) they can be built by wafer bonding of two silicon wafers in which the former wafer outlines the microchannels and the latter one encloses them. The first two approaches use a strategy in which a sacrificial layer is embedded inside of a structural material to integrate the microchannels, as shown in Fig. 2–5. Devices with protruded out topologies employ surface micromachining processes to yield a three-sandwich-layer topology that contains a sacrificial layer embedded into a structural material. The topology of the channel is patterned by photolithography and dry etching processes of the sacrificial layer. Then the microchannels are undercut to determine the effective length of the resonators. Afterwards, the sacrificial layer is removed by wet etching procedures to conform the hollowed cavities. On the other hand, the second approach buries the microchannels into the based substrate and after that, the cavities are enclosed by subsequent deposition of the structural layer. It is necessary to pattern trenches on the silicon wafers to reproduce this fabrication procedure and also to apply well-known protocols for obtaining planar surfaces to enclose the sacrificial layer. Conventionally, this step is achieved by using the chemical-mechanical planarization (CMP) equipment. Finally, the structures can be released from the substrate by wet etching steps or bulk micromachining processes. As a result, this approach facilitates the integration of large and thin microchannels for deliverying fluidic samples because of the obtained planar surface. Henceforth in this Thesis, we decided to build HMB devices based on the first fabrication approach because of the well-known experience and reproducible protocols for achieving robust protruded out topologies using layer-by-layer coatings. Moreover, in our cleanroom facilities, a CMP equipment was not feasible to be used to implement the second approach.

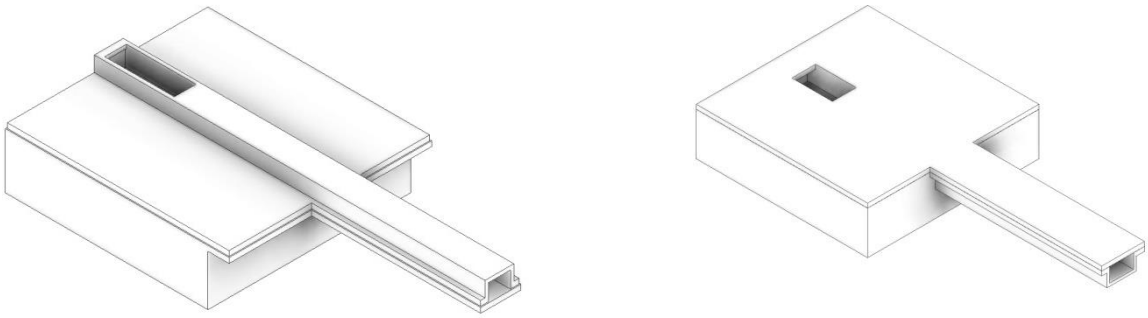

a) b)

Fig. 2–5. Schematics that show two strategies to design resonators with embedded microchannels based on a sacrificial layer strategy: a) a resonator with an embedded microchannel has a topology that protrudes out from the substrate, and b) the microchannel is buried into the substrate and as a result a planar surface is obtained.

Once the topology for the design of HMB devices was established, it was necessary to choose the right combination of the structural and sacrificial materials. Table 2-1 shows a list of the most commonly employed materials to build microelectromechanical devices when using a sacrificial layer. The adequate selection of materials was paramount to determine the mechanical properties of the HMB devices such as good mechanical endurance, high etching selectivity, and low residual stress. For their feasibility, availability and well mechanical properties we used two combinations of materials: silicon nitride (Si_3N_4) and polycrystalline silicon as structural materials, and doped silicon oxide (SiO_2 or PSG) as sacrificial material, respectively.

Table 2-1. Commonly used materials in the fabrication of MEMS devices with their corresponding selectivity [4]

Structural layer	Sacrificial layer	Etching selectivity
PVD or PECVD SiO_2, Si_xN_y	Aluminium	Very high
LPCVD Si_xN_y	Polycarbonate	Very high
	Polysilicon	~ 1000 : 1 (KOH)
	SiO_2	~ 100 : 1 (HF)
	PSG (Phosphorous Silicate Glass)	~ 100 : 1 (HF)
Parylene	Positive photoresist	Very high
Polysilicon	PSG	Very high [8]

Regarding the size of the HMB devices, we must consider that the dimensions of the embedded microchannels are constrained by the size of the resonators. Furthermore, the fluidic resistance of the microchannels is one parameter that should be addressed to facilitate the exchange of fluids inside. In general, the fluidic resistance value highly depends on the dimensions of the microchannels; it directly increases with the length, and it is inversely proportional to the depth of the microchannel. Taking into account these considerations, we proposed a design with straight microfluidic channels, instead of using previously published designs that implemented U-shape microchannels [5]. Our approach is advantageous because of the following reasons: i) by reducing the length of the microchannels, the fluidic resistance can also be reduced avoiding the 90° elbow turns, ii) by locating the microchannels one next to another the sequential or simultenous detection of the out-of-plane displacement of the beams can be simplified and iii) by using resonators with doubly clamped geometry the exhibited natural frequencies, in comparison with those displayed by cantilevers of similar dimensions, will be higher.

Nevertheless, the mechanical motion of the HMB devices will be limited by the doubly clamped configuration of the resonators. As a result, the expected dynamic range for the HMB resonators will be at least an order of magnitude smaller than those devices that use cantilever resonators. Conventionally, the maximum deflection of vibrating structures is imposed by the onset of nonlinearity. For a doubly-clamped beam resonator with an embedded microchannel, the deflection at the onset of nonlinearity is given by [9],

$$\Delta x_{nonlinearity} = \frac{\sqrt{2}}{\sqrt{\alpha Q \sqrt{3}}} \qquad \text{Eq. 2.24}$$

where $\alpha = 0.05A/I$, in which A corresponds to the cross sectional area of the microchannel and I to the second moment of inertia of the hollowed structure, Q is the quality factor. For instance, taking into consideration a HMB device with $\rho_c = 2320\, Kg/m^3$, $\rho_f = 1000\, Kg/m^3$, $w = 12\, \mu m$, $h = 6\, \mu m$, $L = 260\, \mu m$, $h_f = 4\, \mu m$ and $w_f = 10\, \mu m$, $t = 1\, \mu m$ and $Q = 280$ the resulted maximum deflection at the onset of nonlinearity is $\Delta x_{nonlinearity} = 0.5782\, \mu m$.

For the first generation of HMB devices, we considered different design parameters as detailed in

Fig. 2–6. Arrays of resonators were designed with one, two and four microbridges, respectively. The length of the microchannels ranged from 1700 µm, 1500 µm and 1300 µm. These parameters will be useful to optimize the conditions to etch the sacrificial layer properly given that the etching ratio of the etchant solutions depends on the length of the microchannels. Furthermore, the considered length of HMB devices of the first generation was less than 300 µm. By using a trapezoidal frame of 300 µm x 300 µm with a tilt angle at both clamp supports of the beams, we were able to study the effect of the beam length on their natural frequency response. In this way, subtle variations on the length of the beams will render different frequency responses, and thus different mass responsivities. The values for the tilt angle at both clamp supports were 3°, 5° and 7°.

As follows, to study the feasibility to fill the inner cavities with fluidic samples, three different microchannel widths were considered: 10 µm, 20 µm, and 35 µm. The height of these devices varied from 1 µm, 1.5 µm, and 3 µm and the microchannel sidewall thickness was 0.5 µm, 0.75 µm, and 1 µm, respectively. Finally, the distance between each microbridge was set to 10, 15 and 20 µm to facilitate the acquisition of the array response.

Fig. 2–6 shows a schematic overview of a set of four HMB resonators displaying their main dimensions. The size of the fluidic inlets located at both end sides of the microchannels was adjusted to the width of every microchannel with a fixed length of 100 µm. For example, for a microchannel with a 10 µm width, the size of the microfluidic inlet was 8 µm x 100 µm in dimension.

Finally, by embedding a microfluidic channel inside the resonators, we aim to reduce the influence of the damping effects under fluid environment; even such slight modifications in the resonator design can be sufficient to enable the detection of multiple samples. Furthermore, the robustness of the fabrication process for doubly clamped beams and the ability to inject higher driven pressures at the microchannels inlets were important objectives when considering the geometry of the resonators.

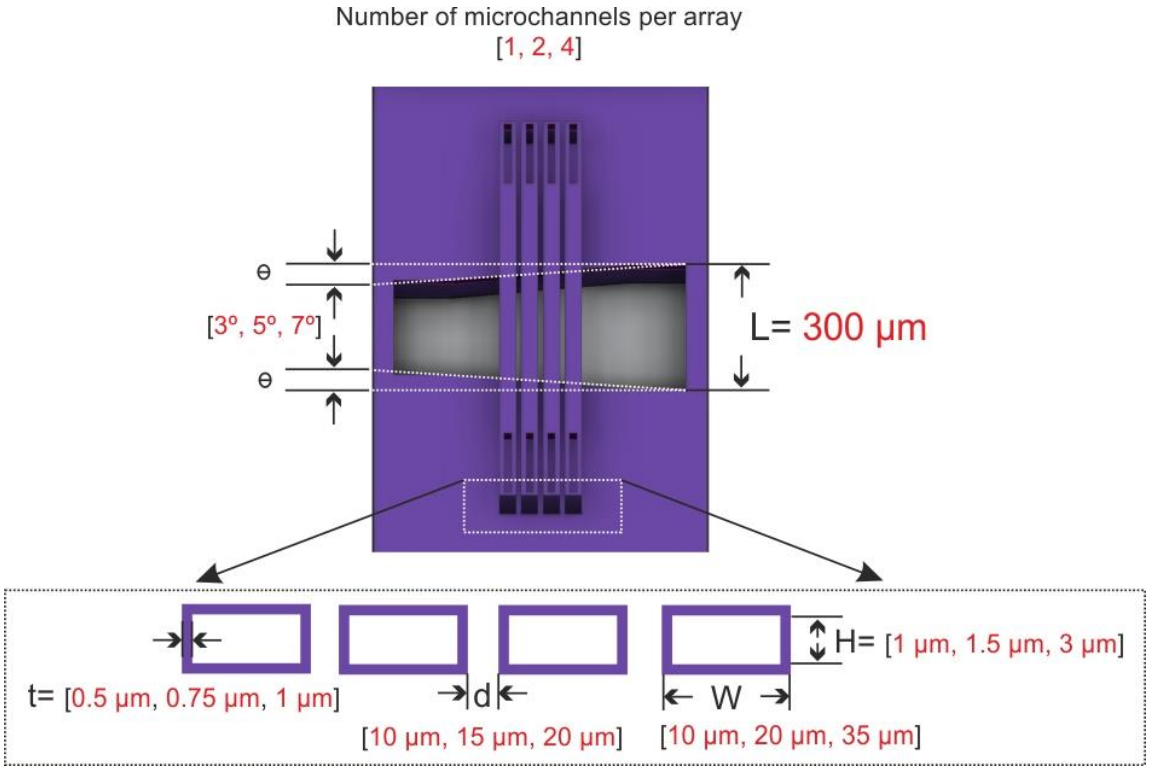

Fig. 2–6. Schematics of the geometry, dimensions, and configuration for the proposed design of the array of HMB resonators.

2.3 Mechanical simulations of HMB devices

The purpose of the FEM simulations consisted of determining the relationship of various parameters such as the length, height, width, material and microchannel wall thickness of the resonators to study their frequency response, sensitivity and elastic constant. The first study consisted of a solid mechanical analysis to compute the existing eigenfrequencies in the array of resonators under vacuum environment conditions. Thereafter, for the calculation of the spring constant of the microstructures, the Cleveland added-mass methodology was employed [10]. Furthermore, to understand the sensor functionality principle, resonant frequency shifts were traced for added masses to the resonators not only to know the equivalent mass of fluids that could fill the inner microfluidic channels such as air, ethanol, water or glycerin but also to obtain the mass responsivity of the HMB devices. All FEM simulations were performed in Comsol Multiphysics software on an Intel Xeon E5520 processor with four cores working at 2.27 GHz and with 24 GB of RAM under a Windows 2008 server.

2.3.1 Eigenfrequency analysis

We used an eigenfrequency analysis to obtain the frequency modes of HMB devices. In this study, the Euler-Bernoulli model was solved for the corresponding domains. To illustrate this simulation, an array of four HMB devices was used with $\rho_c = 2320\ \mathrm{Kg/m^3}$, $\rho_f = 1000\ \mathrm{Kg/m^3}$, $w = 12\ \mu m$, $h = 6\ \mu m$, $h_f = 4\ \mu m$ and $w_f = 10\ \mu m$, $t = 1\ \mu m$ and $\text{tilt angle} = 7^o$. First, the 3D geometry of the structure was drawn in Autodesk Inventor, which is a computer-aided-design (CAD) software that provides a livelink integration to parameterize dimensions. Hence, the list of parameters could be easily tuned for computing sweep mode simulations. In this approach, we employed 3D models of microbridge resonators, instead of using 2D models, which was beneficial for designing purposes and also for increasing the accuracy of the simulation results given that the topology of the structures protruded out from the baseline of the clamped region. Fig. 2–7 shows an example of the 3D scheme for an array of four HMB devices. In here, the structural material was defined as a linear elastic and isotropic material with Young modulus, density and Poisson ratio parameters assigned from the material library of the software. Two materials were taken into account for this simulation, silicon nitride and polycrystalline silicon. For silicon nitride, the following parameters were established: density 3180 kg/m^3, Young Modulus 270 GPa and Poisson ratio 0.27 [11]. Moreover, for the polycrystalline silicon material, the following parameters were established: density 2320 kg/m^3, Young Modulus 169 GPa and Poisson ratio 0.22 [12].

Next, taking into account that a clamp-clamp beam is subject to two constraints, two fixed boundary conditions were assigned at both ends of the resonators. All the remaining boundaries were set as free, as Fig. 2–7 shows. Subsequently, the meshing of the 3D structure was done using fine tetrahedral elements in which the largest element size was set to 0.5 μm to properly mesh the microchannel sidewalls of thickness about 1 μm. These built-in meshes were intended to save computational time and assure analysis precision. Fig. 2–7 shows a fine element size meshing applied to a 3D geometry of four hollow microbridges wherein H1 is the longer resonator and H4

the shortest one. Before running the eigenfrequency study, the user must provide a rough approximation to search around a central frequency peak. This estimation was obtained from the analytical model solution of Eq. 2.17 to search for the first vibrating modes all over the structure. Likewise, this study was implemented for obtaining higher bending modes of the resonators and even longitudinal modes in case they were present. Fig. 2–8 shows the maximum displacement of the four microbridges in free bending mode resulted from the present approach.

As can be noted, the tilt angle introduced subtle variations on the natural frequency of the resonators. For this configuration of resonators, the exhibited range of eigenfrequencies was between 897 KHz and 1030 KHz. In comparison with the analytical solution provided by the Euler-Bernoulli beam theory, the natural frequencies computed from FEM methodology were slightly downshifted by a factor of approximately 4%, as shown in Table 2-2. This can be attributed to the effective length of the resonators introduced by the tilt angle and also because of the protruded out topology of the microchannels. Interestingly only for long beams, as is the case of device H1, higher tilt angles originated another vibration mode. As depicted in Fig. 2–8f, a longitudinal mode with and eigenfrequency of 950 KHz was exhibited. This effect should be taken into account while performing experimental measurements of the HMB devices.

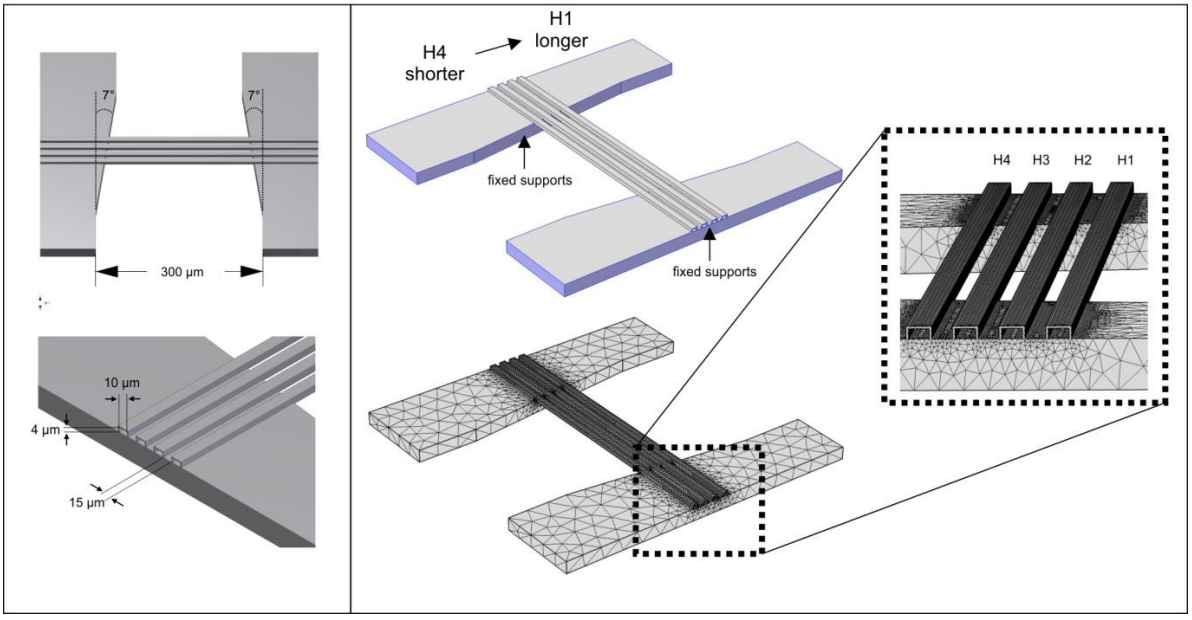

Fig. 2–7. 3D schematic design for an array of four microbridges with embedded microfluidic channels. The image shows the dimensions for a specific design of resonators with a cross-section area of 10 µm x 4 µm, in which the length is provided by a tilt angle of 7° at both clamped sides. For this case, the distance between beams is 15 µm and polysilicon is selected as the structural material. The image also shows the fixed boundary conditions that are designated on the 3D scheme of the HMB devices and the free tetrahedral mesh using a "finer" element size with a minimum element size of 0.5 µm.

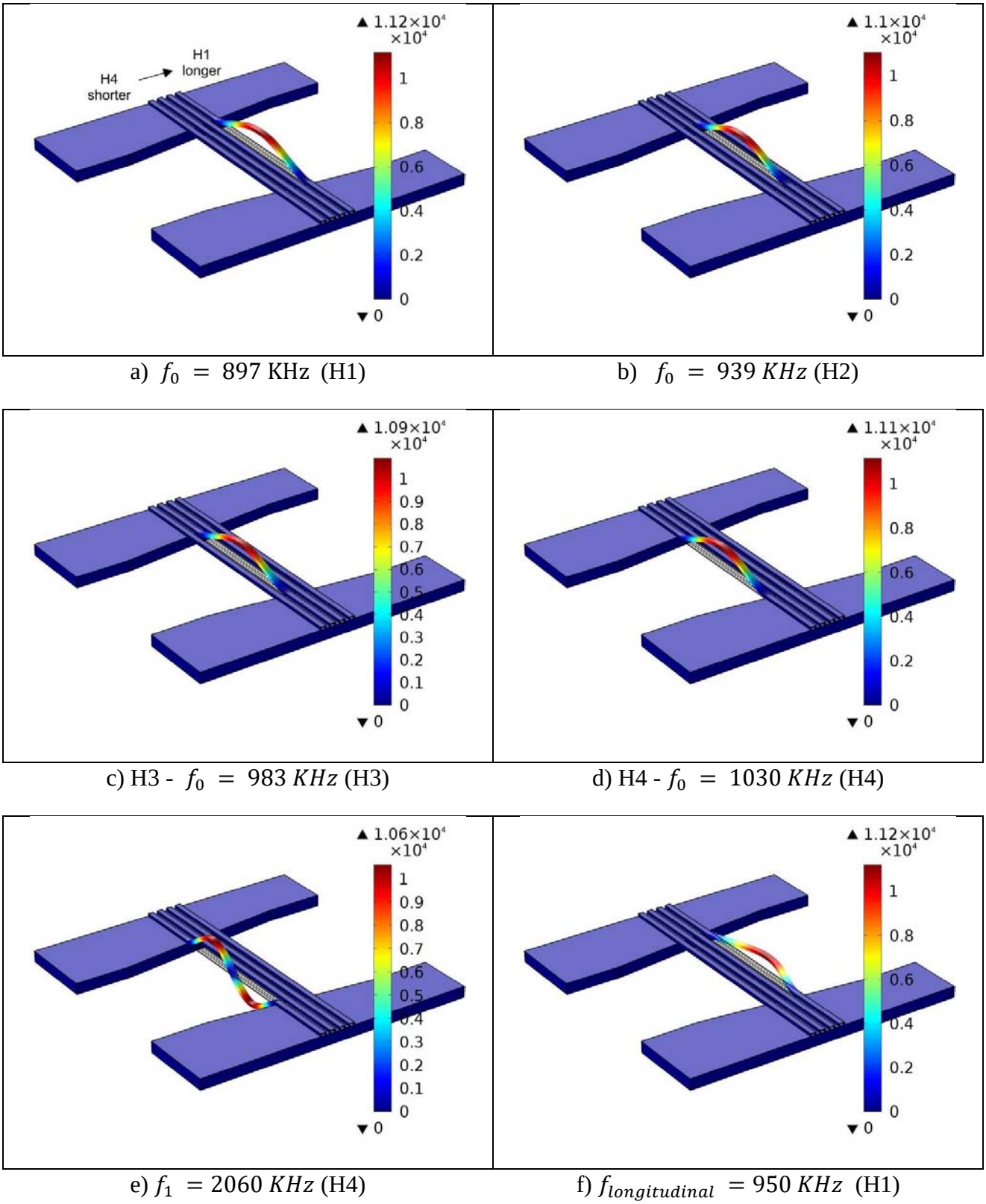

a) $f_0 = 897$ KHz (H1)

b) $f_0 = 939\ KHz$ (H2)

c) H3 - $f_0 = 983\ KHz$ (H3)

d) H4 - $f_0 = 1030\ KHz$ (H4)

e) $f_1 = 2060\ KHz$ (H4)

f) $f_{longitudinal} = 950\ KHz$ (H1)

Fig. 2–8. Results of the eigenfrequency analysis of a 3D structure of HMB devices. From a) - d) first bending modes for an array of HMB devices with a tilt angle of 7^oat both clamped sides, e) second resonant mode for the shortest beam "H4" and f) longitudinal oscillation for the longest beam "H1" as a result of the length shift produced by the tilt angle.

2.3.2 Calculation of the spring constant

The eigenfrequency analysis was also used to determine the spring constant of each resonator based on the Cleveland added mass method. This methodology estimates the elastic constant of a vibrating structure given the resonant frequency shift resulted from the attachment of known masses. Thus, if a series of added masses are attached to each resonator, the slope of the plot of mass versus $1/f^2$ would yield the corresponding elastic constant according to the following equation,

$$\omega^2 = \frac{k}{M_{eff} + \Delta m} \qquad \Rightarrow \qquad [M_{eff} + \Delta m] = k\left[\frac{1}{\omega^2}\right] \qquad \text{Eq. 2.25}$$

The model geometry and composition were defined as in the previous section, but a new boundary condition was incorporated to the physic model. The added mass Δm condition was set on the inner boundaries of the microchannels to gradually change the effective mass of the resonators, as shown in Fig. 2–9. By supporting incremental mass loadings of 1 pg in the range of 1 pg to 10 pg, the eigenfrequency study was computed for each case, and thereafter a linear approximation fitting was performed to find the spring constant by the aforementioned methodology. Table 2-2 shows the calculated elastic constants for the studied array of HMB devices. Regarding the elastic constant, it was demonstrated that shorter devices, as the case of beam H4, are stiffer than larger ones. In particular for this configuration the elastic constant of the resonators ranged approximately between 2420 N/m to 3500 N/m.

Table 2-2. Comparison of the resonant frequencies obtained by analytical theory and finite element simulations for an array of four HMB devices filled with different fluids.

Bridge	Average Length (µm)	Sensor mass (ng)	f_{theory} (kHz)	f_{empty} (kHz)	f_{air} (kHz)	$f_{ethanol}$ (kHz)	f_{water} (kHz)	$f_{glycerol\ 50\%}$ (kHz)	K_{sim} (N/m)
H4	253.79	16.50	1063.81	1030.00	1029.90	874.92	843.30	826.66	3514.3
H3	259.95	16.90	1013.98	983.00	982.47	834.63	804.57	788.59	3091.3
H2	266.09	17.30	967.70	939.00	938.26	797.06	768.30	753.09	2730.5
H1	272.29	17.69	924.16	897.00	896.94	761.96	734.42	719.93	2420.8

2.3.3 Calculation of the mass responsivity

In the previous methodology, a series of mass loads were added to the inner cavities of the HMB devices to shift their resonance frequencies. From these results, it is clearly shown that there is a direct and linear interplay between the added mass and the frequency response of the resonators. If the slope of the plot of frequency versus added mass is obtained, then the mass responsivity of a single device can be computed. Henceforth, the mass responsivity was calculated for incremental mass loads in the range of 1 pg to 10 pg, in a similar way than in the calculation of the spring constant, as Fig. 2–9 shows.

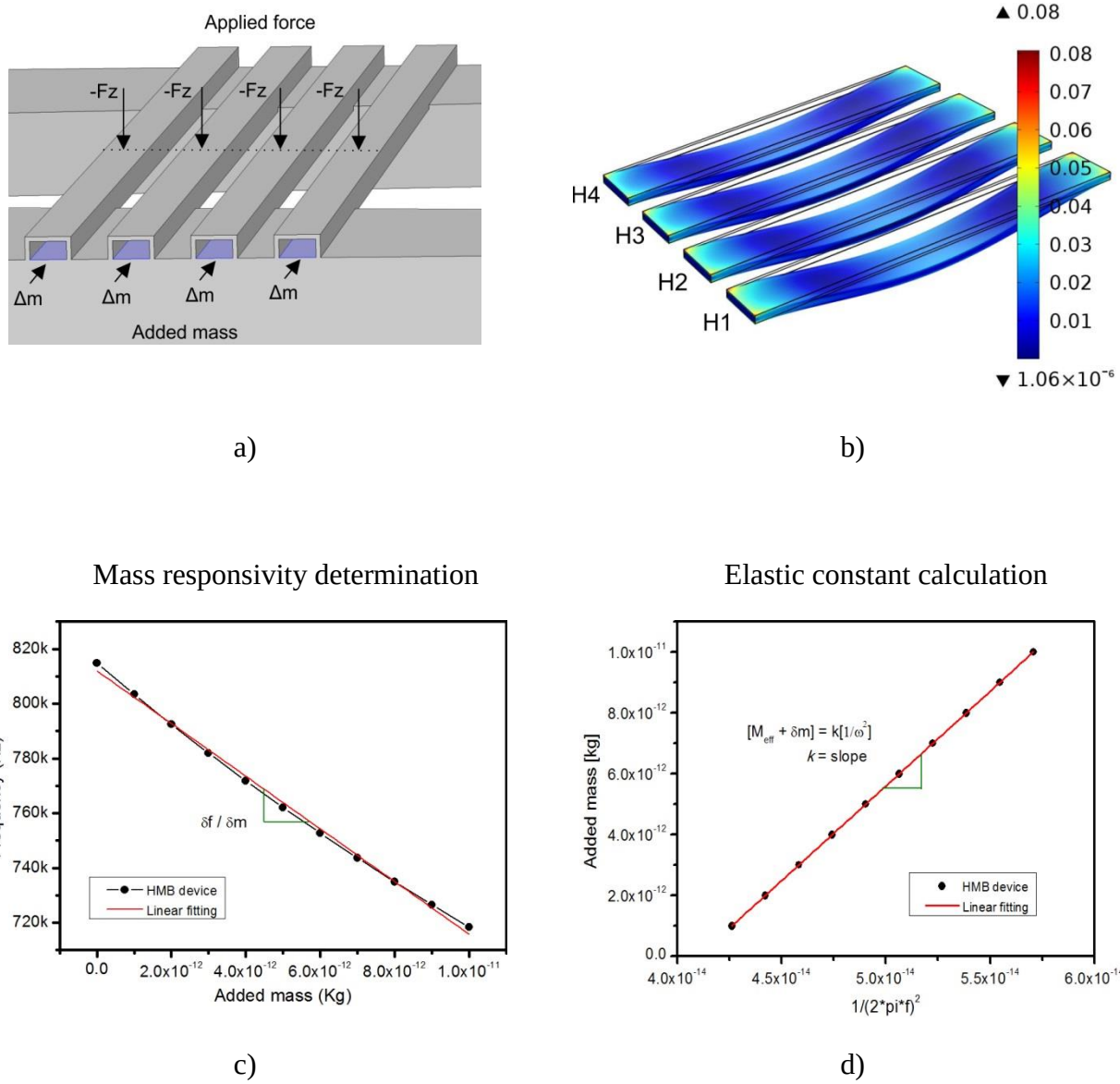

Fig. 2–9. a) Scheme showing the boundary conditions designated for adding mass loads into the embedded microchannels; b) Subtle deformation of the array of resonators due to the effect of added mass; c) Calculation of the mass responsivity of the resonators from the curve fitting of the frequency response versus the added mass and d) Calculation of the elastic constant from the slope of the added mass versus $1/f^2$.

Following the above approach, the study of the added mass was employed to understand the sensor response to different fluid samples. For this reason, the volumetric integral of density was calculated with FEM simulations to find the effective mass of various fluids contained on each microchannel, fluids such as air (1.184 kg/m^3), ethanol (785.22 kg/m^3), water (1000 kg/m^3), and a 50% solution of glycerol (1123.75 kg/m^3). These liquids were chosen because they notably differ in their density values. Table 2-2 shows the frequency response of each microbridge considering the added mass effect of each fluid inside the hollowed structures. From the simulation results, the frequency shift derived from the change in the sample density displays a linear tendency. Liquids with higher densities depicted higher downward frequency shifts than liquids with lower densities. This behaviour was also demonstrated between the elements of the array of HMB resonators for which the H1 device displayed the lowest frequency values for all fluid samples.

2.3.4 Sweep mode analysis

Once the eigenfrequency response, elastic constant and sensor mass values were obtained for a single and specific combination of dimensions. We performed a parametric sweep analysis to study the influence of these parameters on the HMB device response. In this way, the height, width and tilt angle at the clamp supports were modified to carry out the simulations by combining such specific parameters in the Comsol interface.

The first analysed parameters were the response of the resonant frequency and mass responsivity of the HMB devices with respect to the depth and length of the microchannels. From the simulation results, the resonance frequency and the mass responsivity increased as a function of the microchannel height for both materials polycrystalline silicon and silicon nitride, as shown in

Fig. 2–10. This can be explained by the Euler-Bernoulli beam theory, in which the height of the beam is a parameter that directly depends on the frequency response of the resonator.

On the other hand, since the length of the beams was reduced by the tilt angle, the exhibited mass responsivity was higher for devices with shorter effective length. This is because the mass of those devices is lower than that of beams with longer effective length, and thus higher mass responsivities are expected. For instance, the device H4 made of polysilicon with a tilt angle of $7°$ showed a maximum resonance frequency of 1.029 KHz with a mass responsivity of 21.49 Hz/pg. On the other hand, the homologous silicon nitride device H4, depicted a maximum frequency response of 1.083 KHz with a mass responsivity of 18.35 Hz/pg. This represents a frequency shift and mass responsivity change of 4.98% and 14.61%, respectively. Interestingly, the yielded mass responsivity for polycrystalline devices was higher than that for silicon nitride ones. As the density of the polycrystalline silicon material (2320 kg/m^3) is less than the silicon nitride material (2700 kg/m^3), less amount of mass is expected for devices with similar dimensions built from polycrystalline silicon. Another fact that supports this behaviour is that the mass of the fluidic sample becomes higher than the mass of the solid structural material for microchannels with higher depths, and therefore, the resonator can track more adequately the mass changes produced inside the microchannel due to the added mass effect of the sample.

We can now consider the case of a single HMB resonator in which its width and tilt angle are modified to analyse the behaviour of the frequency response, the elastic constant and the mass responsivity. Fig. 2–11 shows plots of these parameters as a function of the dimensions of a single beam. As a result, the computed resonance frequency increased as the width of the beam was narrower. Likewise, devices with reduced effective length, as a result of higher tilt angles (7°), followed a similar interplay displaying higher frequencies. In general, the resonant frequency of the HMB resonators was strongly influenced by the length of the beams which resulted in higher frequencies than those expected by the subtle variations on their widths. Besides, the elastic constant was strongly influenced by the width of the beams; wider HMB devices yielded higher elastic constants and thus stiffer structures. Also, as the effective length of the beams was reduced, their elastic constant also became higher. For instance, the maximum depicted value for the elastic constant value was 4693.8 N/m for a device with 35 µm width and length about 260 µm. Regarding the mass responsivity of the devices, this parameter behaved in a similar way as the frequency response. Resonators with lower mass exhibited higher mass sensitivities. In this way, we can expect that microchannels with short effective lengths and narrow widths are more suitable for mass sensing applications.

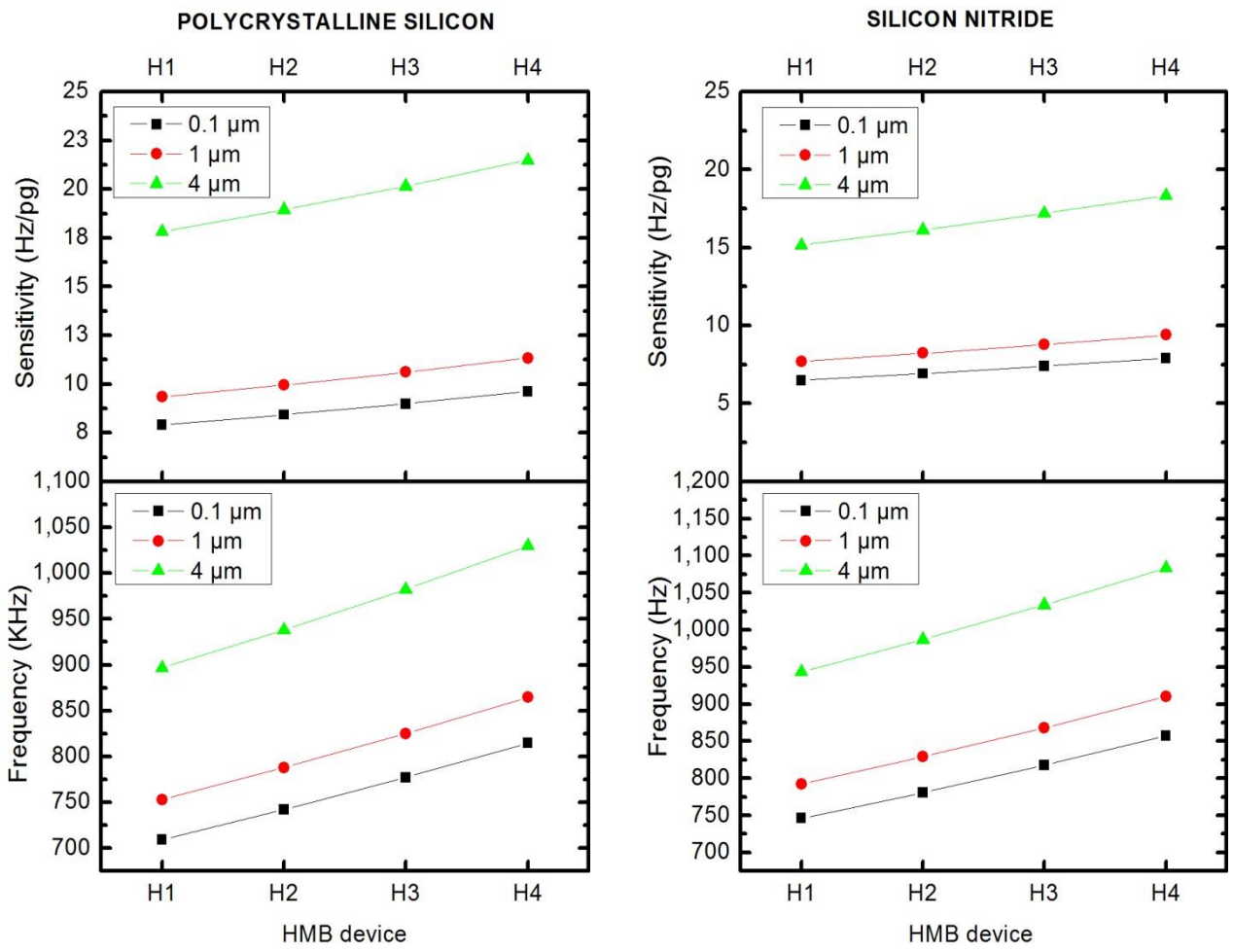

Fig. 2–10. Plots that show the mass responsivity and the fundamental frequency response for an HMB device with $w_f = 10\ \mu m$, $tilt\ angle = 7^o$and $t = 1\ \mu m$. A sweep analysis mode is done in terms of the position of the beams inside the array and with respect to the depth of the inner microchannels. The results are shown for polysilicon and silicon nitride materials.

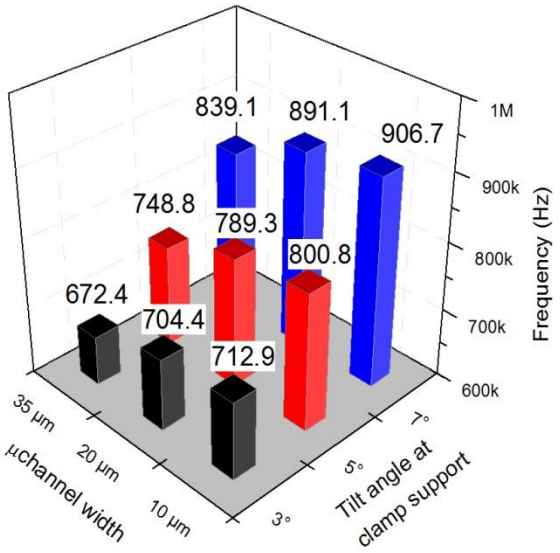

a)

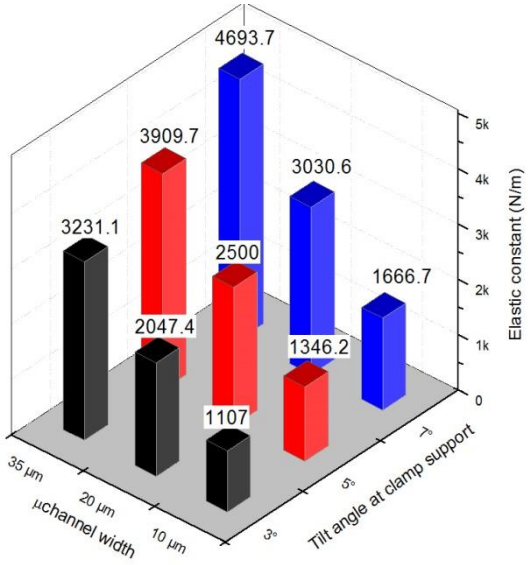

b)

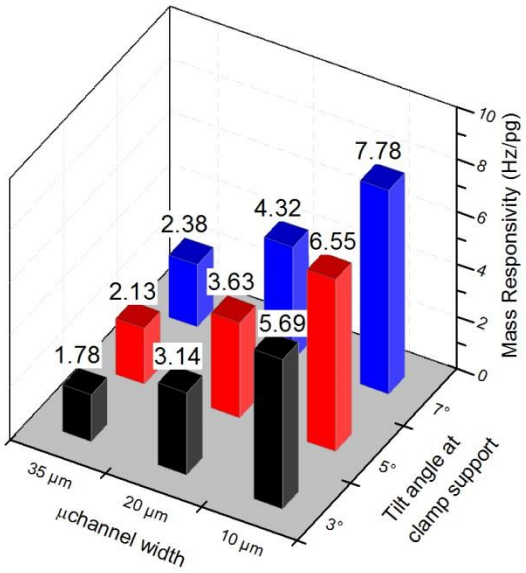

c)

Fig. 2–11. 3D plots that indicate the interplay between the microchannel width and the variation of their length due to a tilt angle at both clamped supports. For this analysis, three parameters are computed: a) resonance frequency response, b) elastic constant and c) mass responsivity.

2.4 Microfluidic simulations of HMB devices

A rough approximation of the microfluidic behaviour of the embedded channels can be provided by using analytical solutions. However, a deeper analysis and studying of the fluidic properties of the microchannels is crucial to understand the transport of the liquids inside the cavities. Henceforth, a complementary study of the governing microfluidics physics involved in our devices was performed using FEM simulations. Firstly, a stationary study is conducted to characterize not only the laminar flow conditions with respect to the microchannel dimensions but also the pressure drop, average flow velocity, and Reynolds number. Likewise, a fluid structure interaction analysis is carried out to investigate the influence of the volumetric flow rate on the stress of the sidewalls of the microchannels. Basically, the motivation relies on whether the present design of HMB devices can withstand pumping of liquids at different volumetric ratios given the reduce thicknesses of their walls. Finally, an exhaustive study based on a Level Set methodology analyses different pathways to fill with liquids the inner cavities of the HMB devices through a microfluidic interface. In-line and H-shaped configurations are proposed as well as various schemes to inject fluids into the resonators. From this approach, the time that it takes to fill completely the microchannels can be determined based on the selected microfluidic configuration and boundary conditions to better understand and predict the flow-through behaviour inside the fluidic channels.

2.4.1 Theory

An important design issue of HMB devices implies the influence of both the inner flow and the generated hydrostatic pressure on the dynamic behaviour of the structures. Resonators with embedded microchannels can cover a wide range of flow rates given the high intrinsic fluidic resistance of the microchannels. In practical applications, however, it is useful to determine the pressure that the resonators can withstand to avoid collapsing of the inner channel walls in operational conditions. While streaming sample fluids inside the cavities at higher flow rates, the internal hydrostatic pressure also increases. The relative change in the microchannel cross-section surface causes a variation in the elastic constant of the resonator depending on the aspect ratio and sidewall thickness of the microchannel as well as in the applied flow rate. When taking into account HMB devices, which consist of hollowed doubly clamped resonators, it can be assumed that the stiffness change in the device is negligible due to their robust topology, and those changes derived from inner hydrostatic pressure do not contribute to increasing the elastic constant of the beams. Hence, it is important to analyse the latter parameter that influences the dynamics of the resonator: the fluid flow behaviour inside the cavities which primarily yields the mass shift of the resonator. Analytically, the pressure decay and flow rates through an embedded microchannel can be modelled as a fluid transported through a rectangular channel using the Hele-Shaw theory [13]. Therefore, a reasonable approximation that introduces a pressure difference in a microchannel with rectangular cross-section is given by [14]:

$$\Delta P\left[1-\frac{6(2^5)}{\pi^5}\frac{h_f}{w_f}\right]=\frac{12\mu L}{w_f\,{h_f}^3}Q_{flow} \qquad \text{Eq. 2.26}$$

where ΔP is the pressure difference along the microfluidic channel, μ is the water viscosity (1 cP), w_f, h_f and L are the microchannel width, length and height, respectively and Q_{flow} defines the flow rate (μL/min). When the ratio $h_f/w_f \ll 1$, the volumetric flow rate expression can be simplified using a parallel plate approach as follows,

$$Q_{flow}=\frac{w{h_f}^3}{12\mu L}\Delta P \qquad \text{Eq. 2.27}$$

This approximation has an error below 7% for aspect ratios $h_f/w_f < 0.1$ and below 50% for $h_f/w_f < 0.5$. Another important parameter is the velocity magnitude profile inside the microchannel. Assuming a laminar inflow, the flow velocity with a parabolic profile is given by [14],

$$v_c=\frac{h_f^2}{8\eta}\frac{\Delta P}{L} \qquad \text{Eq. 2.28}$$

Given the strong influence of the size of the microchannel geometry on the achievable flow rates by suspended resonators, Fig. 2–12 shows the interplay between the microchannel aspect ratio of HMB devices and the spanned flow rates using Eq. 2.27.

2.4.2 Stationary study of microchannels

For this simulation, an array of four rectangular microchannels, with dimensions shown in Table 2-3, was imported from the CAD design software. After setting the geometry, the intrinsic properties of water were selected from the materials model library. For this study water was considered as a non-compressive and Newtonian fluid with no-slip boundary conditions at the microchannel walls. This means that the velocity profile is parabolic and can be determined by using the Hagen–Poiseuille's law [13]. As follows, eight boundaries conditions were selected to establish the inlets and outlets of the microchannels, respectively. Two values of volumetric flow rates were considered for the microchannel inlets (0.1 μL/min and 1 μL/min). Meanwhile the output was set to zero pressure, and the effect of backflow was suppressed. For the meshing conditions, the element size was calibrated to "finer" considering a fluid dynamics mesh, which resulted in a minimum element size of 0.1 μm. This type of mesh settings accurately maps the physics in which fluidic structures are involved by making the element size denser. Thereafter, a stationary study was implemented to provide a suitable approximation of the flow behaviour on each microchannel and

to predict the corresponding pressure decay. A comparison scheme for the analytical approach using Eq. 2.26 and the results of FEM simulation is presented in Table 2-3.

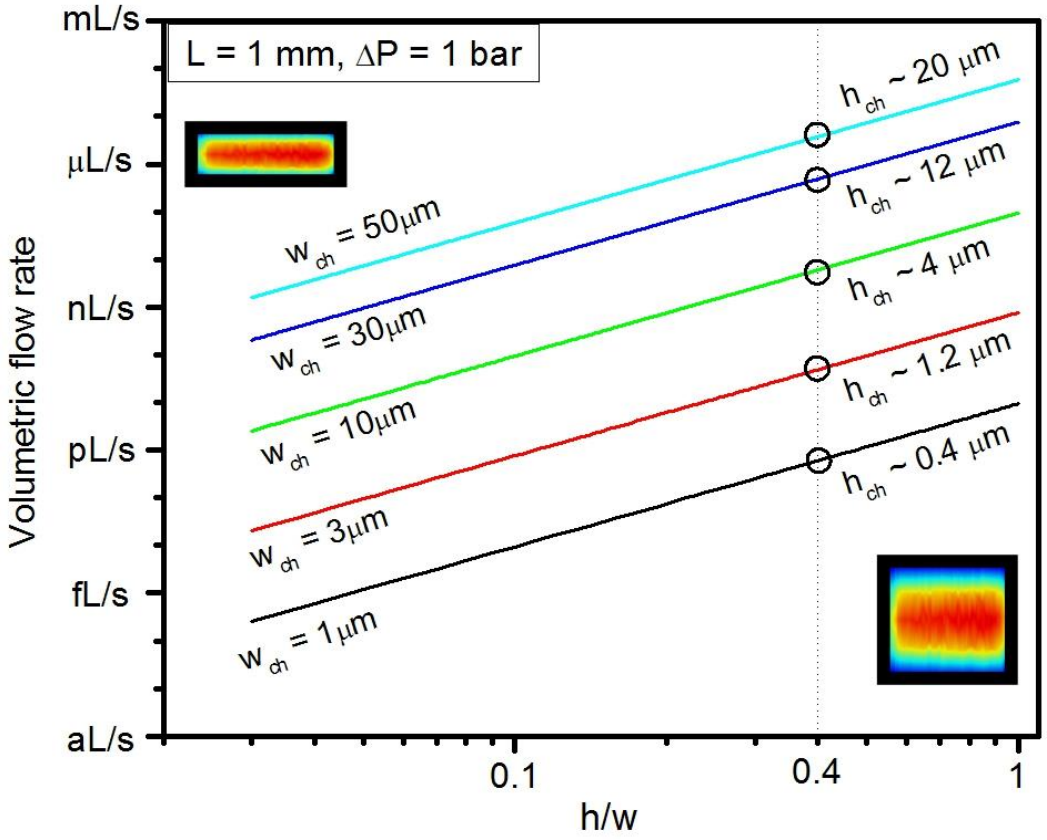

Fig. 2–12. Volumetric flow rate as a function of the aspect ratio of the microchannels. The flow rate proportionally increases as a function of higher microchannels dimensions. For instance, for a device with $w_{ch} = 10$ μm and $h_{ch} = 4$ μm the expected flow rate is in the order of nL/s.

The interplay between the pressure decay at different inlet flow rates was also investigated to complement the results of the previous study. Fig. 2–13 shows two approaches to compare the pressure drop for a single channel compared to an array of four channels. Notably, the pressure proportionally decays as the number of microchannels increases; in the case of four channels, it decreased about 80% with respect to a single channel. This direct relationship was also displayed for narrower channels in which higher flow rates were applied.

Table 2-3. Comparison of analytical and FEM results when filling an array of four microbridges with cross-section area of $w_{ch} = 10$ µm and $h_{ch} = 4$ µm with a tilt angle of 7° at two given flow rates.

		Analytical		Simulation					
		0.1 µL/min	1 µL/min	0.1 µL/min			1 µL/min		
Bridge	Average Length (µm)	Pressure drop (MPa)	Pressure drop (MPa)	Pressure drop (MPa)	Reynolds number	Average Velocity (m/s)	Pressure drop (MPa)	Reynolds number	Average Velocity (m/s)
H4	253.79	0.663	6.63	0.0109	0.0096288	0.040987	0.109	0.096272	0.40987
H3	259.95	0.679	6.79	0.0112	0.0097525	0.040979	0.112	0.097503	0.40979
H2	266.09	0.695	6.95	0.0115	0.0099834	0.040969	0.115	0.099803	0.40969
H1	272.29	0.711	7.11	0.0117	0.0099901	0.040959	0.117	0.099889	0.40959

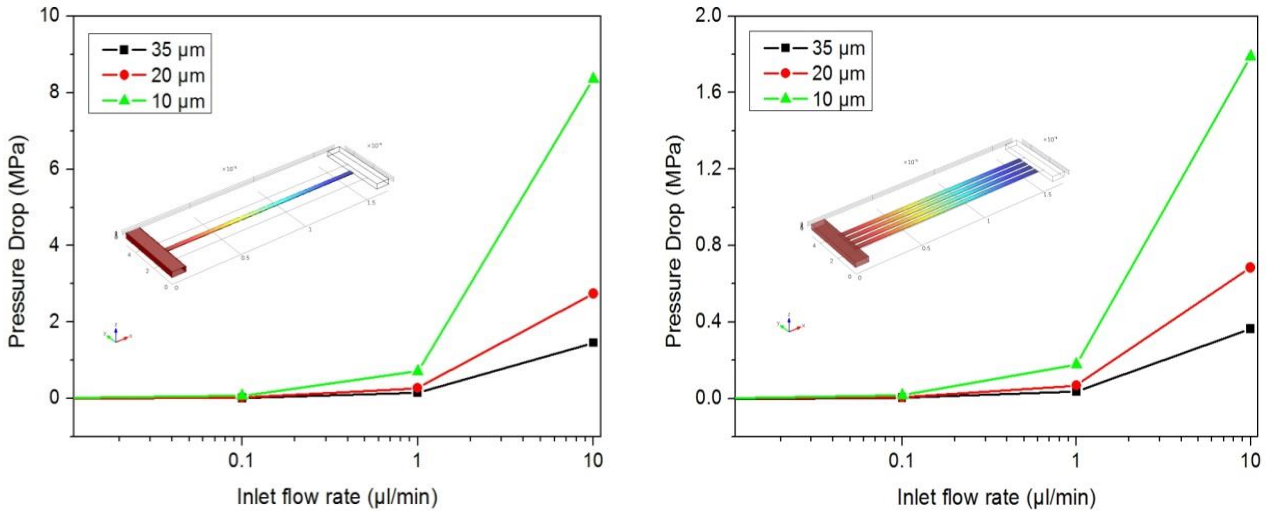

a) b)

Fig. 2–13. Comparison of two microfluidic schemes that study the influence of the inlet flow rate, width of microchannels and pressure drop for: a) a single microchannel and b) an array of four microchannels.

2.4.3 Fluid-structure interaction analysis

Mechanical design of MEMS requires the ability to predict the strength of load-carrying components with stress concentrations. The majority of these microdevices made of brittle materials, such as polysilicon, can exhibit higher fracture strengths when smaller volumes or areas are involved [15]. In engineering applications, Von Mises stress is a widely used methodology to verify whether a structural design can withstand explicit boundary loads. In simple terms, this approach consists of comparing if the maximum value of the Von Mises stress is more than the value of the fracture strength of the structural material. For instance, using Weibull statistics, the fracture strength of the polysilicon material has been found to be (2.9±0.5) GPa in tensile tests and (3.4±0.5) GPa in bending tests [16]. Thus, if a stress study is conducted, the resulted von Mises stress over polysilicon thin-films should be at least higher than 3.0 GPa.

Besides, when using channels with micro- and nanoscale dimensions, the pressure drop along their longitudinal axis can increase or decrease due to some circumstances. For example, the microchannels can be depleted while capturing targeted molecules during biosensing applications. Another common issue is the formation of air bubbles while introducing analyte samples as well as when the properties of the liquid are changed such as its density or viscosity. As a consequence, the fluidic resistance of the microchannels will be modified, yielding pressure differences throughout the cavities. Henceforth, it is important to study the influence of localized areas that exhibit pressure drops when the volumetric flow rate is biased and how this interplay affects the solid structural material of the microchannel.

Hence, the following study complies with the analysis of the structural deformation of the microchannel walls, built from polycrystalline silicon, while streaming water solution. To solve this model, it is necessary to include two different physics as follows. The first part of the analysis consists of a stationary study that computes the stress forces produced along the microchannel sidewalls while streaming a sample solution at a given volumetric flow rate. In the second part of the study, a solid structure analysis is done to find the Von Mises stress produced over the walls based on the stress forces generated from the first injection of water. The simulation is carried out using an array of four polysilicon HMB devices with a microchannel width of 35 μm, a 4 μm depth and an effective length determined by a 7° tilt angle, as depicted in Fig. 2–14. The thickness of the walls is 1 μm. These dimensions correspond to the most robust design implemented for the fabrication of HMB devices.

First, the 3D geometry of the array of HMB devices was drawn directly in the Comsol interface to facilitate the assignment of the boundary conditions for both the fluid and solid structural domains, as described in Fig. 2–14a. Thereafter, all the inner boundaries that belonged to the microchannels were defined as the walls of the fluidic microchannel; these boundaries represent the interface between the two physics to be solved. As follows, it was determined that the inner cavity of the microchannel was composed of water with density of 1000 kg/m^3 and dynamic viscosity of 0.894 mPas. On the other hand, the solid structural material was composed by polycrystalline silicon with Young Modulus of 170 Gpa, density of 2320 kg/m^3 and Poisson ratio of 0.23. Next, it was necessary to establish the boundary conditions for the multiphysics model. Regarding the boundaries of the fluid domain, the interior edges of the microchannels were assigned with no-slip

boundary conditions, and water domain was defined as an incompressible fluid. A volumetric flow rate $Q_{flow} = 0.1\ \mu L/min$ was designated to every microchannel inlet to produce a pressure drop along the longitudinal axis of the resonators, and so the output of the microchannel was set with a pressure equal to zero (P = 0). The entrance length for the volumetric flow rate was 1 mm and the backflow effects were supressed. On the other hand, for the solid structural material, the face edges of the microchannels at both ends were set as fixed supports, as Fig. 2–14a shows. Moreover, for the stationary study of the solid structural domain, it was determined that the interior boundaries of the cavities should support the equivalent boundary loads (force per unit area) produced by the first stationary study on each x, y and z direction.

About the generation of the finite elements to compute the simulation, the whole solid structure was designated with a general mesh type using a "finer" element size in which the minimum element size was 1 μm and the liquid domains were defined using a fluid dynamics mesh. This category of mesh is preferable when using fluidic domains because the ratio of curvature of each element is smoothed. To solve the model, the stationary solution for the fluid domain was first computed to obtain the stress forces along the walls. Finally, the model was completely solved using the results of the first simulation in which the stress values were applied to the solid structural domain over the inner boundaries.

Fig. 2–14 shows the state of the microchannels before and after the injection of water and Table 2-4 displays the results for the computed maximum velocity magnitude, the pressure drop along the cavities and the Reynolds number. The resulted maximum velocity magnitude was very similar for the four microchannels within the range of mm/s. Moreover, since the computed values for the Reynolds number (~ 0.00119) were much lower than 2300, the conditions for laminar flow were accomplished for the proposed design. From the simulation, it can be inferred that the pressure drop is directly proportional to the length of the microchannels, and thus it decreased from beam H1 to beam H4. Likewise, the maximum value for the Von Mises stress (~ 0.34 MPa) was outperformed for shorter microchannels. Interestingly, the maximum computed Von mises stress was located near the entrance of the fluidic channels and then it smoothly decayed across the longitudinal axis. It could also be noticed that sidewalls that conform the top and bottom edges of the microchannels were more susceptible to deformation. Since the ratio h/w is lower than the unity, the deformation of the lateral walls was negligible. When comparing the typical fracture stress of thin films of polysilicon (~2.9 GPa), this value is four orders of magnitude higher than the maximum value depicted by the von Mises stress of HMB devices (0.15 MPa). Thus, we conclude that our devices can withstand flow rates commonly used for bioanalytical applications.

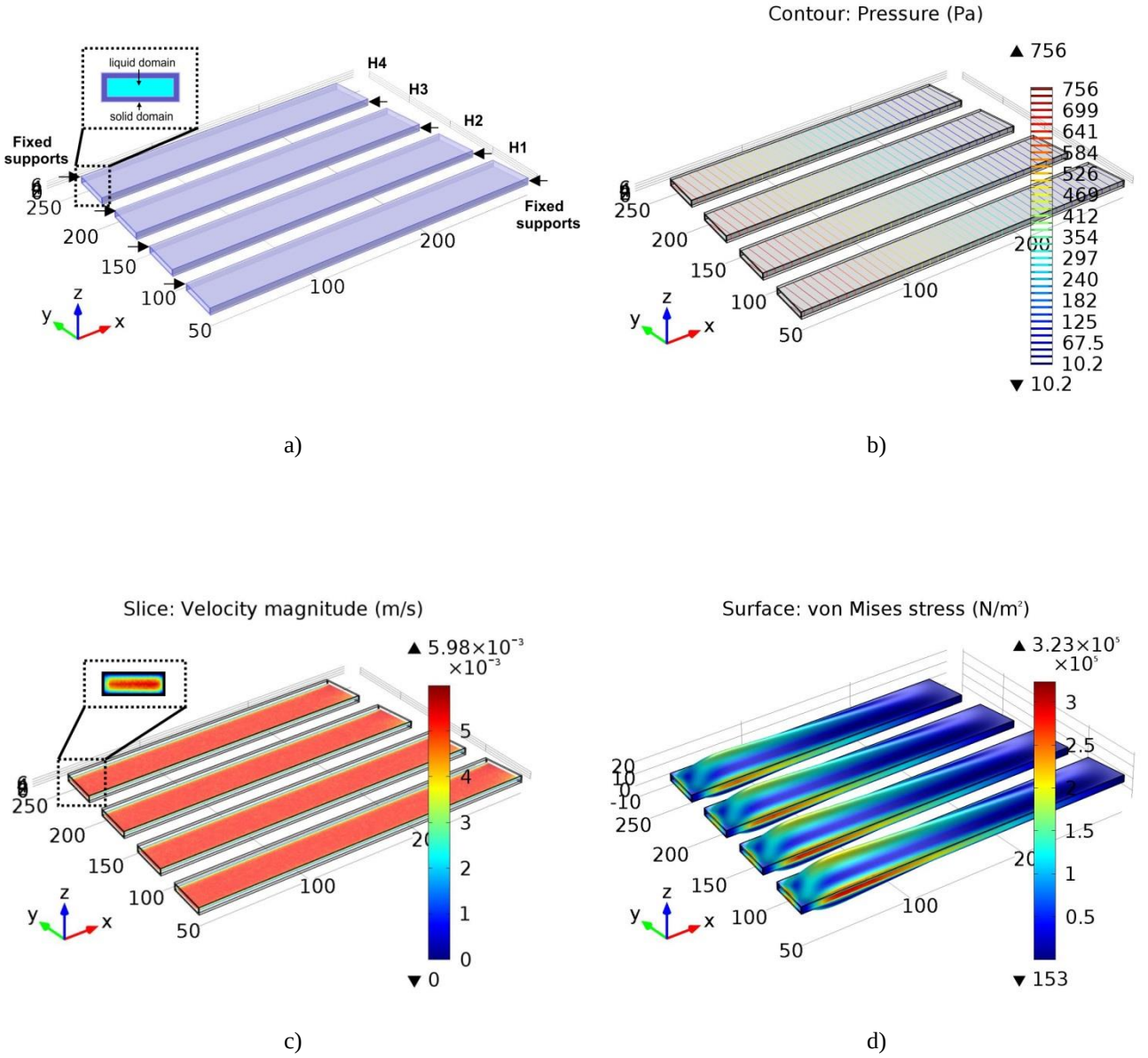

Fig. 2–14. FEM simulation to determine the Von Mises stress of an array of HMB devices for a given flow rate. a) Definitions of the solid and fluid domains in the 3D geometry. b) Pressure drop across the microchannels after solving the first stationary solution of the model. c) Profile of the water velocity magnitude and d) Von Mises stress produced over the microchannels walls after solving the second stationary solution of the model.

Table 2-4. Comparison of the computed parameters for an array of four HMB devices when filled with water at an inlet flow rate 0.1 μL/min and the resulted von Mises stress along the sidewalls of the microchannels.

HMB device	Velocity magnitude (m/s)	Pressure (Pa)	Cell Reynolds number	von Mises Stress (Pa)
H1	0.00598	765.47	0.00119	347840
H2	0.00592	729.58	0.00121	331420
H3	0.00595	693.02	0.00121	314550
H4	0.00595	657.19	0.00117	305410

2.4.4 Filling study of microchannels

One of the advantages of the proposed design of HMB devices is their low sample volume consumption. Given the microscale dimensions of the embedded microchannels, only small amounts of fluid samples, in the order of picoliters, are necessary. However, in real-world applications, liquid samples are dispensed in larger quantities (in the range of microliters) to assure the complete exchange of liquids throughout the measurement device. Therefore, an interface is required to link macroscopic volumes of fluids with on-chip fluidic microchannels of HMB devices. Moreover, depending on the fluidic interface configuration, different systems can be used to handle and dispense such small volume quantities at minimal flow rates such as low-pressure pumps, syringe pumps, and pressure-controlled equipment. For instance, High-Performance Liquid Chromatography (HPLC) systems can stabilize and control the pressure difference along the fluidic microchannels to accurately deliver samples at constant flow rates. Thus, the choice of the suitable fluidic interface network to exchange samples inside the microchannels is determined by several factors such as the foreseen application, the morphology of the microchannels and the structural materials employed.

In the case of resonators with embedded microchannels, there are basically two schemes to fill the inner cavities of the channels. In the first approach, the fluid can easily be displaced by direct injection of the sample insofar the dimensions of the embedded microchannels are large enough. This scheme, named in-line fluidic configuration, is commonly used for direct interconnection of the microchannels with macroscopic size tubes and thus low-pressure pumps can be suitable for transporting samples, as Fig. 2–15a illustrates. On the other hand, if a rapid exchange of sample fluids through the microscale channels is necessary, a fluidic interface with a bypass configuration can be implemented. This approach, named H-shaped configuration, consists of outlining bypass channels with larger cross-sectional dimensions across the fluidic inlets of the embedded microchannels. This scheme avoids the need of directly pump large volumes of liquids through the resonators, as shown in Fig. 2–15b.

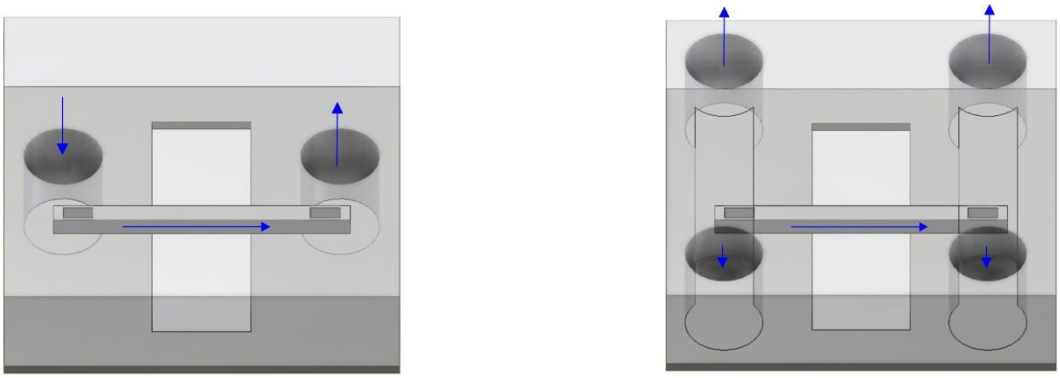

a) b)

Fig. 2–15. Fluid samples can be delivered into the microchannels of suspended resonators using two microfluidic configurations: a) direct in-line injection and b) H-shaped approach in which two bypass channels establish a differential flow inside the resonators.

We have performed FEM simulations to study different pathways for filling the inner cavities of the resonators using either the H-shaped or in-line fluidic configurations. In this way, the feasibility to fill the inner cavities can be verified by using commercial syringe pumps to control the volumetric flow rate to dispense the sample fluid instead of controlling the pressure along the microchannels to generate a constant flow rate. FEM simulations were implemented in Comsol Multiphysics using a Level Set methodology to study the flow dynamics behaviour of water once it enters into the microchannels. Particularly, the simulations are focused on determining the time to fill the cavities completely and to calculate the pressure and velocity profile while the filling process takes place. Finally, a comparison of both 2D and 3D schemes is performed to evaluate the accuracy, time and resources consumption of the models.

2.4.4.1 Level Set method

Level set methods have been used in a wide variety of applications such as image processing, compressible and incompressible two-phase flows, droplets formation and multiphase flow through a porous medium, to mention a few [17]. In general, a level set method consists of tracking the motion of an interface that is moving through two different domains. In the area of MEMS devices, Level set methods can be used to study the transport and position of small amounts of fluids when samples are carried through the microchannels with micro and nanoscale cross-sections [18].

Modelling the transporting of water through a water/air interface can be implemented using FEM simulations in Comsol Multiphysics. In general, the model determines the pressure field, the velocity field, and the position of the water domain using a Level Set Laminar Two-Phase Flow interface. To model this behaviour, the level set method designates a function ϕ that is a distance function, with two main values. We consider the case of a fluid interface that separates two commonly used fluid domains such as water and air. The water is transported through a microchannel, which is originally filled with air. The distance function (ϕ) sets a default value for each domain: for the water domain ϕ =1, and for the air domain ϕ =0. Meanwhile, the contour of the fluid interface corresponds to ϕ = 0.5, as depicted in Fig. 2–16. The motion of the fluid interface through the channel is governed by partial differential equations in which the conservation of mass and momentum transport are expressed in terms of the Navier-Stokes equations [19],

$$\frac{\partial \phi}{\partial t} + \boldsymbol{u} \cdot \nabla \phi = \gamma \nabla \cdot \left(\varepsilon \nabla \phi - \phi(1-\phi) \frac{\nabla \phi}{|\nabla \phi|} \right) \quad \text{Eq. 2.29}$$

where ε is the interface thickness and Υ is the reinitialization function. The Level Set function represents the fluidic interface between the contained air and the transported water by employing a reinitialized level set method. When using FEM simulations, the thickness of the fluid interface is determined by $\varepsilon = h_{max}/2$ where h_{max} represents the maximum size of the elements used to mesh the model. Since the fluid interface is moving through the channel, the distance function ϕ needs to constantly be reinitialized to satisfy the initial conditions for the water and air domain. A good rule of thumb is to equalize the reinitialization parameter to the maximum magnitude of velocity in the channel. Besides, across the fluid interface, the magnitudes of density and viscosity slightly vary according to the following equations,

$$\rho = \rho_{air} + (\rho_{water} - \rho_{air})\phi \quad \text{Eq. 2.30}$$

$$\mu = \mu_{air} + (\mu_{water} - \mu_{air})\phi$$

Finally, the Level Set approach establishes the boundary conditions of the microchannels such as the wall adhesion and surface tension coefficient to provide a better approximation of the flow

dynamics inside the cavities. Fig. 2–16 illustrates the main parameter settings employed in the Level Set method.

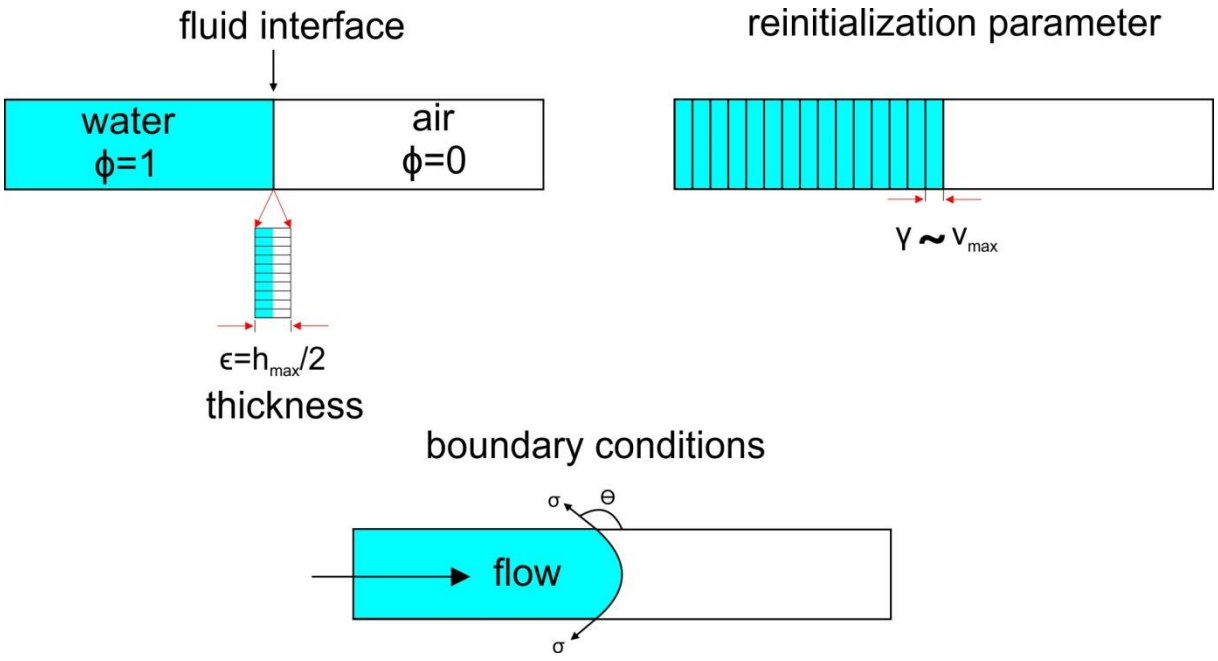

Fig. 2–16. A general overview of the parameters used in the Level Set Method to predict the filling process of a microchannel: the fluid interface thickness ε, reinitialization parameter ϒ and boundary conditions of the sidewalls σ.

2.4.4.2 Filling of microchannels in 2D domain

This model initiates by defining the morphology of the microchannels. Fig. 2–17 shows the 2D scheme drawn directly in the Comsol interface. The fluidic configuration consists of three microchannels and two bypass channels. This configuration differs from the conventionally employed array of four microchannels because the filling analysis was optimized for a third generation design of HMB devices. The dimensions of the microchannels are 16 μm x 790 μm of width and length, respectively, with a separation distance between the microchannels of 500 μm. The bypass microchannels have cross-section dimensions of 300 μm x 1500 μm, and a 500 μm x 100 μm reservoir is placed at one end of the left bypass channel for pumping up water.

Subsequently, the domains for air and water are defined in the 2D scheme, as indicated in Fig. 2–17a. The properties of each liquid are chosen from the materials library in which air has a density of 1.2256 kg/m^3, and a dynamic viscosity of 17.86 μPa s. Whereas water has a density of 1000 kg/m^3 and a dynamic viscosity of 3.94 mPa s. Both fluids are considered as incompressible, and turbulence is neglected. The operational temperature of the model is 293.15 K. By default, the surface tension coefficient is selected according to the properties of the fluids involved in the model; in this case, the surface tension is provided by the water/air interface. The parameters of the Level Set Laminar Two-Phase Flow interface are associated to each fluid domain along with the initial boundary conditions. As shown in Fig. 2–17a, the water domain (ϕ =1) corresponds to the reservoir located at one end of the inlet bypass channel whereas the remaining surface of the fluidic network is comprised by the air domain (ϕ =0). The fluid interface is represented by the boundary located between both domains, with an interface thickness $\varepsilon = h_{max}/2$, where h_{max} is about 0.5 μm. Since the simulation is performed for a direct in-line configuration scheme, water is pumped through the bottom boundary of the reservoir at a constant flow rate of 20 μL/min. Then, water is pumped out of the fluidic network through a boundary located at the top end of the right bypass channel. To facilitate the solution of the simulation, no-slip boundary conditions were preserved for all microchannel walls, except for those boundaries assigned for the fluid interface, the inlet and the outlet flow.

For this 2D configuration, the reinitialization parameter is assigned according to the maximum velocity magnitude of the model such that $\gamma = 1\ m/s$. The entire fluidic configuration is meshed employing two schemes. A mapped distribution of elements is assigned to the microchannels with a fixed number of elements (5 x 150), and free quadrilateral elements are set for the remaining surface with a minimum element size of 0.032 μm, as shown in Fig. 2–17b.

Particularly, the convergence of the solver method is not easy to achieve when computing microfluidic simulations because the convergence strongly depends on the mesh settings and the solver type. Therefore, the settings suggested in [20] served to improve convergence in the nonlinear time-dependent model of the present study according to the parameters shown in Annex 1. By updating the Jacobian on every iteration, the stability of the nonlinear process increased and the maximum number of iterations was limited; a process otherwise controlled by the tolerance factor [20]. Another useful configuration that optimized the processing time of the study and its convergence relied on adjusting the parameters for the Time-dependent solver (BDF). The time-dependent analysis was solved from 0 ms to 400 ms with increments of 5 ms. To solve the study, the model first determines by default the conditions for the Level set function and then the time-dependent analysis is performed. The solution of the model took about 5 hours to be completed. Fig. 2–17 and Fig. 2–18 show the results of the simulation displaying the volume fraction of water, velocity, and pressure drop for increments of 5 ms. The discussion of these results is presented in the next section to compare both the 2D and 3D simulation schemes.

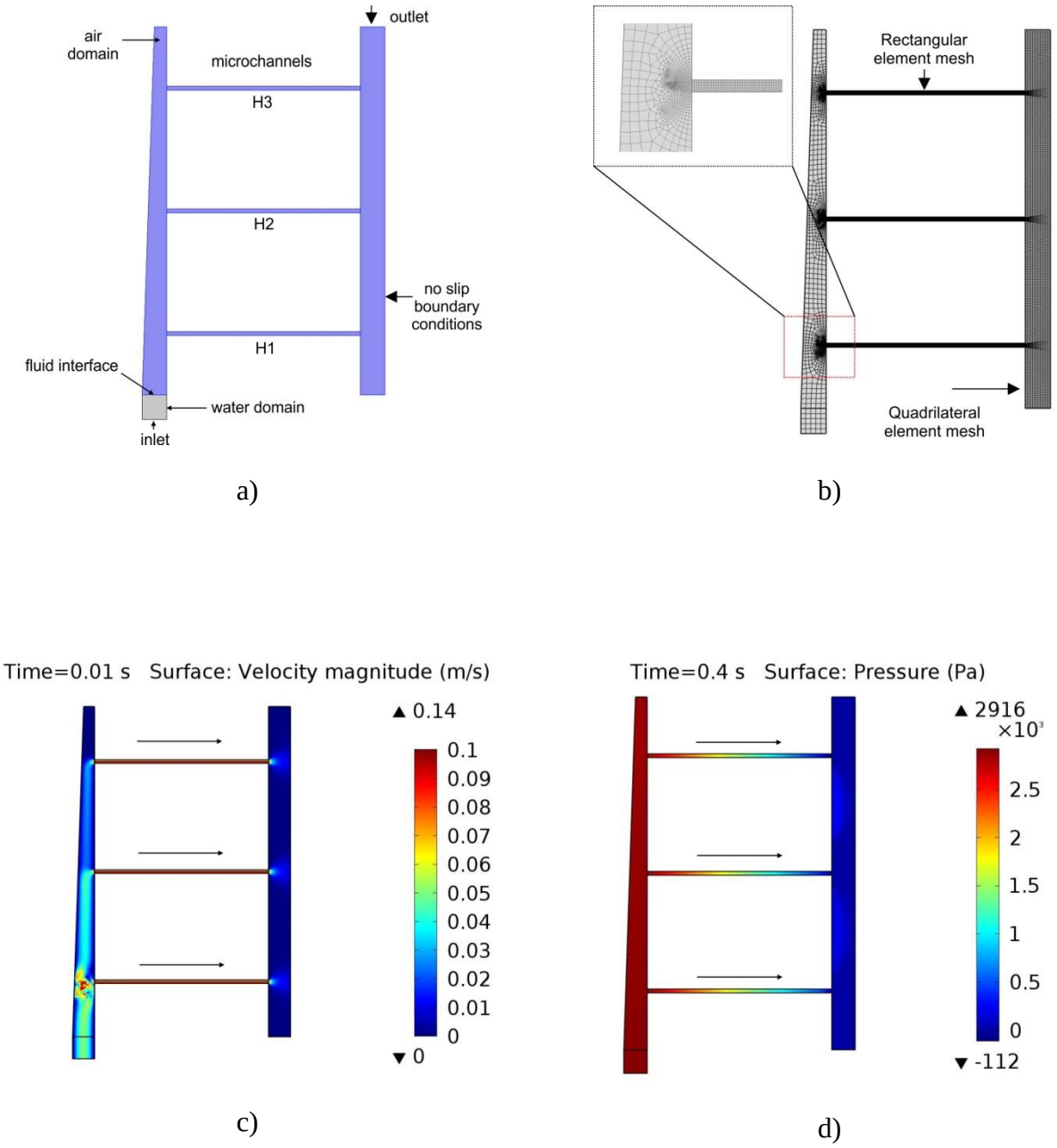

Fig. 2–17. 2D schematics of the in-line microfluidic configuration to transport liquids inside the microchannels: a) fluid domains and boundary conditions settings for the Level Set Laminar Two-Phase Flow interface, b) fluid dynamics mesh type to map the whole fluidic surface. The results of the time-dependent analysis display the values for c) velocity magnitude and d) pressure profile of the filling process of water at time increments of 5 ms.

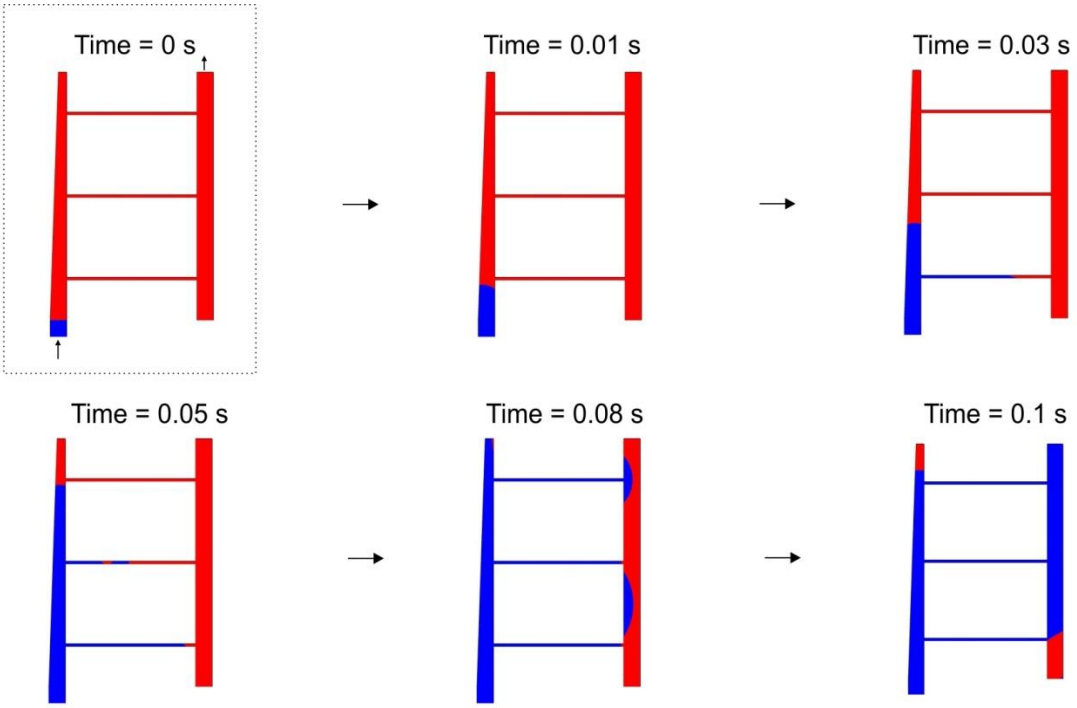

Fig. 2–18. The graph shows the evolution of the fraction of water volume while it is transported throughout the microfluid interface using an in-line filling configuration. Water is pumped at a constant flow rate of 20 µL/min. The microchannel is completely filled after 0.1 s because of the no-slip boundary conditions that facilitated the injection of water.

2.4.4.3 Filling of microchannels in 3D domain

The previous problem in which a 2D fluid interface was studied for driving liquids inside the microchannels was also solved in the 3D domain. This new model incorporates the height of the microchannels (4 µm) and also the depth of the connection bypass channels (35 µm) to provide a better understanding of the filling process. In a similar way than in the previous model, dimensions, materials, fluidic domains and boundary conditions were tuned in the 3D scheme, as depicted in Fig. 2–19. The fluid interface separates both water and air domains. Water is transported through the fluidic network across the array of three microchannels at a constant flow rate of 20 µL/min from the bottom reservoir to the upper side of the second bypass channel. To simplify the resources and save computational time, all the sidewalls of the microchannels were assigned with no-slip boundary conditions.

One of the common issues when working with 3D domains is to define properly the initial meshing conditions of the geometry. Typical errors are derived while meshing small features when domains of higher dimensions need to be linked to smaller ones as is the case of the union between the microchannels and the bypass fluidic channels. To address this drawback, a combination of several mesh styles is carried out to assure the interconnection between all finite elements. Firstly, a sweep of rectangular elements is used to mesh the three microchannels. Secondly, quadrilateral type elements are mapped onto the internal face of the bypass channels following the geometry traced by

the microchannels lateral face, as the Fig. 2–19b shows. Then, a swept mesh is mapped across the width of the bypass microchannels to mesh the 3D geometry completely. Finally, the overall meshed elements are defined as "Fluid dynamics" type.

To start the resolution of the microfluidic model, an iterative solver method with multigrid geometry settings was considered. The multigrid solver in Comsol is an iterative solution method that accelerates the convergence by solving the model on a series of meshes instead of using a single one. The idea is to build coarser meshes automatically from the initial user-defined mesh. For instance, each additional mesh can be twice the size of the original one. In this way, the coarser mesh of the geometry that led to a low number of degrees of freedom to be solved by a direct solver provides the first solution to the problem. Subsequently, the accuracy of the solution can improve when considering finer mesh settings iteratively. Nevertheless, one of the major drawbacks while employing a multigrid solver is that small features included in the geometry typically generate errors. This is because the size of the coarsest mesh is larger than the smallest features size of the 3D geometry. Henceforth, an exhaustive research with an alternative trial and error methodology is implemented in our 3D simulations to find optimum conditions and reliable resources to fill up the microchannels. In this way, specific parameters of the iterative solver were tuned up based on the solution of other microfluidic models [21] when various dimensions are included in their geometry [22]. Annex 1, shows a summary of the optimum parameters used in the 3D microfluidic simulation.

As a result, the level set method obtained the velocity field, pressure field and volume of the fluid profile while transporting water inside the microchannels for a time range from 0 s to 0.4 s with increments of 0.05 s, see Fig. 2–19c-d. The simulation took about 5 days and several hours to be completed. Bearing in account the interplay between these parameters, an estimation of the filling process can be explained as follows. Regarding the filling of the first microchannel H1, the average velocity magnitude inside the microchannel starts decreasing as a function of time when the water domain reaches the fluidic entrance of the microchannel. While water is transported through the microchannel, the velocity magnitude continues decreasing until achieving a minimum value at t = 0.019 s. In this time, the microchannel is filled to a 57% and the minimum velocity magnitude value is maintained until the microchannel is filled.

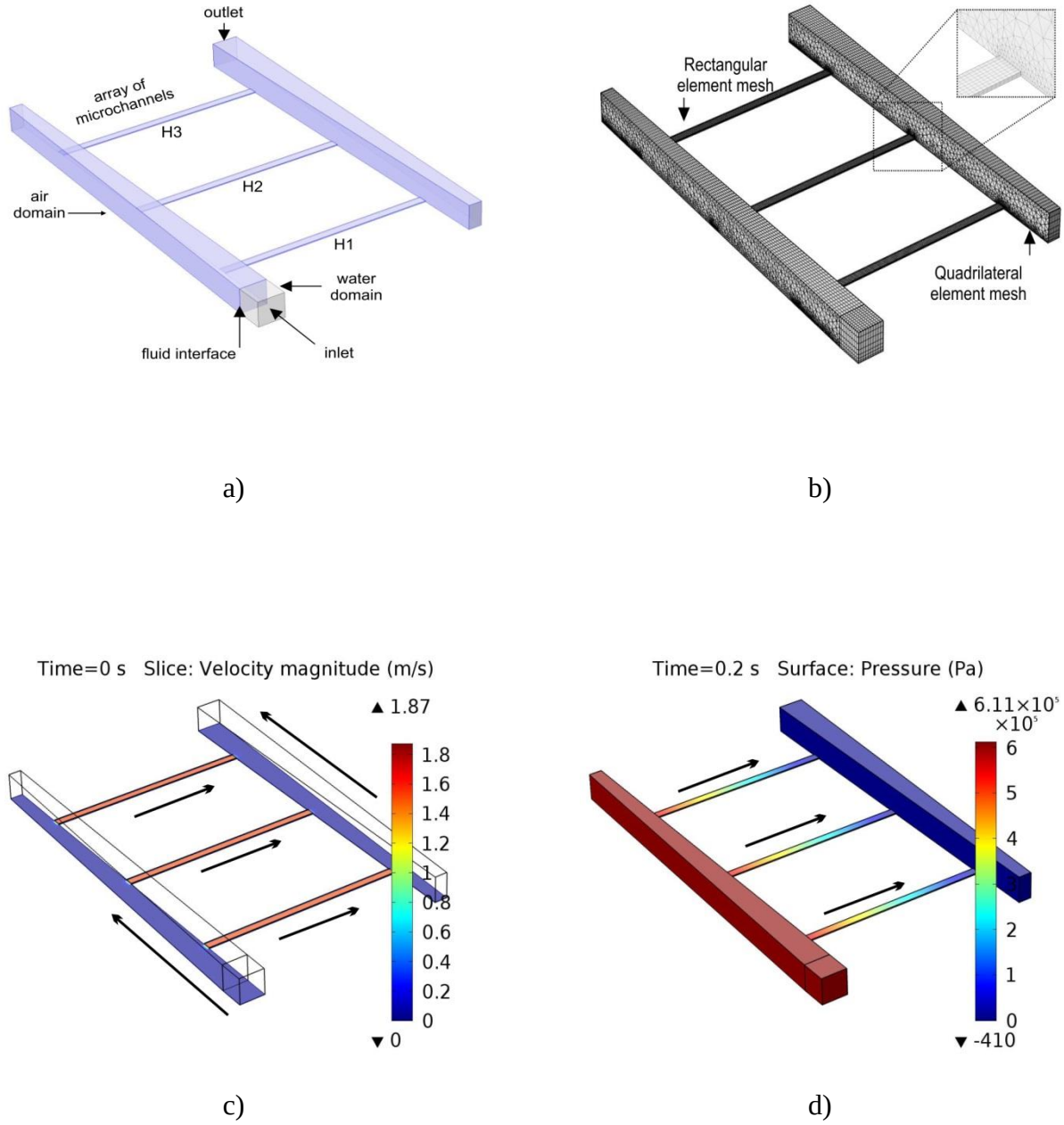

Fig. 2–19. The sketch shows a 3D in-line microfluidic configuration that incorporates the height values for the microchannels (4 μm) and also the depth of the connection bypass channels (35 μm) to analyse the fluid exchange inside the cavities: a) The domains for water and air are defined along with the fluidic interface and boundary condition settings for the Level Set Laminar Two-Phase Flow interface, b) the fluidic interface is mapped using a combination of rectangular and quadrilateral elements to match the fluid domains correctly. The results of the time-dependent analysis display the values for the c) velocity magnitude for a "xy" plane located at z = 2 μm and d) the pressure profile of the water filling process for time intervals of 5 ms.

In contrast, the average pressure difference along this microchannel slightly increased to compensate the loss in the velocity magnitude. When t = 0.0417 s both parameters, the average pressure and the velocity magnitude, abruptly increase indicating that the microchannel is almost filled. Once the cavity is completely filled (t = 0.05 s) the average velocity stabilizes close to its original value and the average pressure maintains a maximum value while water continuously flows through the microchannel. Notably, the fluid exchange inside the microchannels is more easily accomplished after it is totally filled, as shown in Fig. 2–20.

The filling process of microchannel H2 is slightly different from the previous one. First, the average velocity of the microchannel increases to a maximum point (of approximately 1 m/s) when water is transported through the bypass channel. This can be explained in terms of the air initially contained in the cavity. Since the density of air (1.2256 kg/m^3) is lower than that of water (1000 kg/m^3), the velocity magnitude increases until all the air is pulled out. Hence, when water reaches the inlet of the channel H2 (t = 0.025 s), the velocity magnitude abruptly decays. This process continued until achieving a minimum velocity magnitude (0.05 m/s) at t = 0.034 s. At this moment, the microchannel is filled to a 60%. Remarkably, at t = 0.039 s, the average pressure and the velocity magnitude increase when the channel is filled to a 76%. This is because water that is transported through the inlet bypass channel has already reached the entrance of channel H3. As a consequence, the pressure differences across the two bypass channels start to compensate, facilitating the filling process for all the microchannels. When t = 0.0436 s the microchannel is almost filled and the average pressure continues increasing up to its maximum value. Once the microchannel is filled, the average velocity and pressure are stabilized as it occurred for the microchannel H1. Interestingly, the mean time to fill channels H1 and H2 was very close; the volume fraction of water indicates that filling of both channels took 0.045 s, as illustrated in Fig. 2–21.

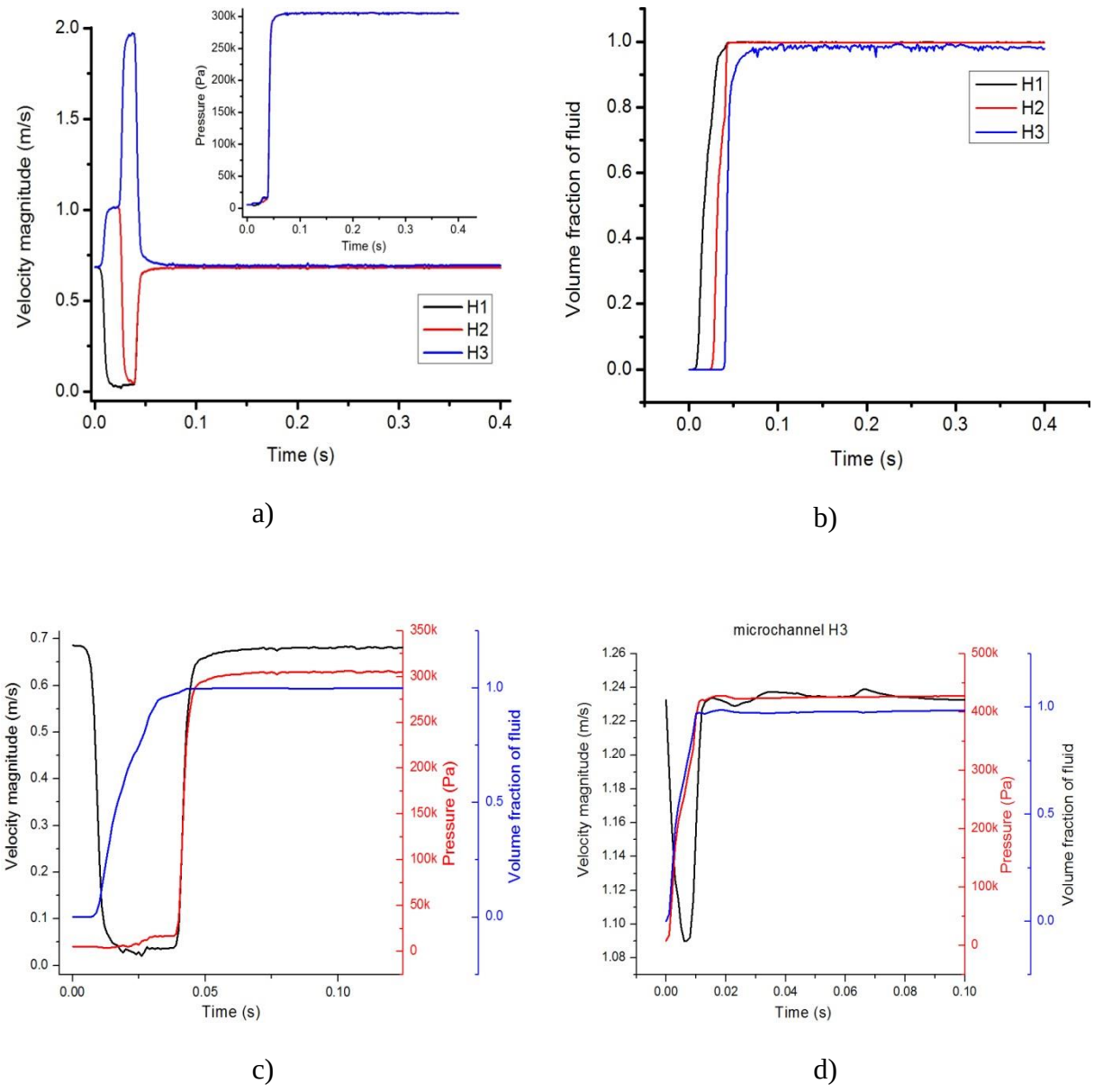

Fig. 2–20. Processing of data after the water filling process of the 3D microfluidic configuration indicates that the average velocity profile inside the microchannels changes while the initially contained air is being displaced. The filling of microchannels occurs very slowly until the pressure across the bypass channels stabilizes. a) Pressure and velocity profile during the filling process of the array of microchannels. b) The volume fraction of water indicates when the filling process is completed. c) The plot shows the interplay between the fluidic parameters while the microchannel H1 is transporting water. d) A comparison of the filling scheme of the array of microchannels when water is simultaneously pumped through them; the process occurs more rapidly achieving higher average magnitudes of pressure and velocity.

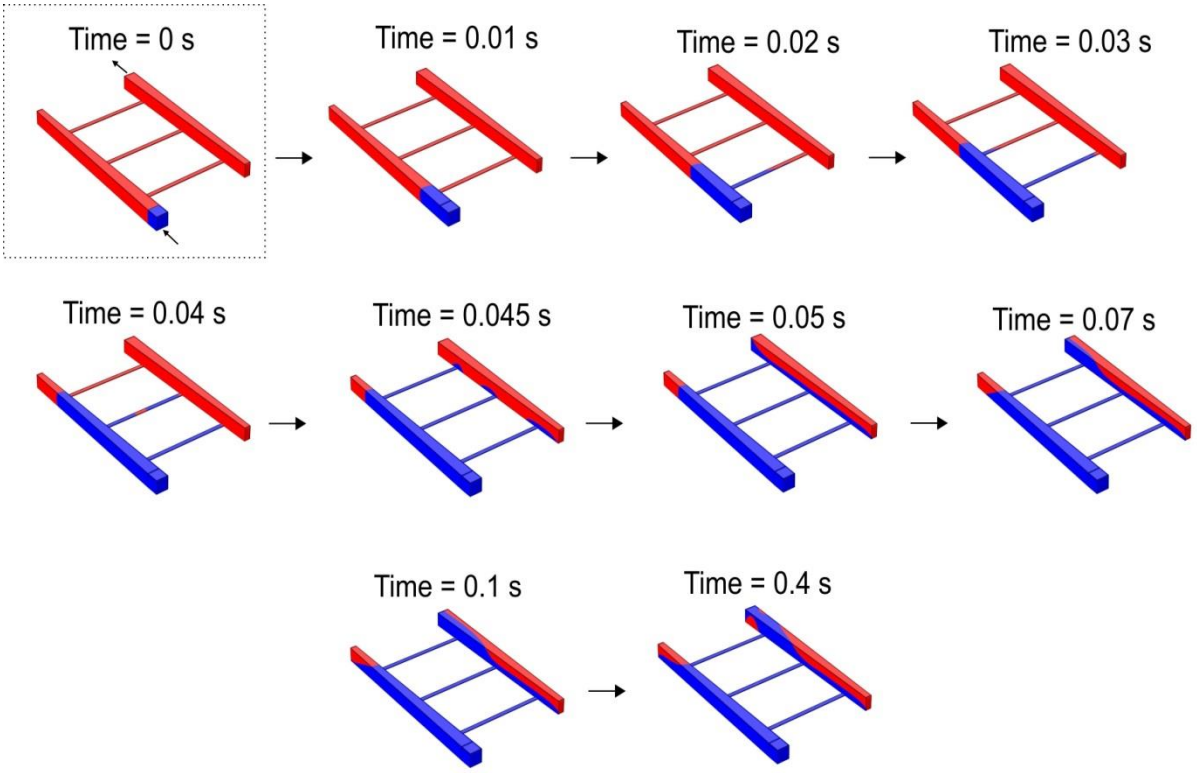

Fig. 2–21. The diagram displays the filling process of an in-line microfluidic configuration wherein water is transported throughout the network at a constant flow rate of 20 µL/min. The volume fraction of water (*zones in blue*) indicates that the filling process is completed after 0.1 s according to the simulation results. Notably, a fraction of air (*zone in red*) is trapped on dead end portions of the bypass channels. When the pressure is stabilized across the bypass microchannels, all the microchannels are already filled.

Finally, regarding the microchannel H3, Fig. 2–20 shows an increase in the average velocity of the microchannel while the initially contained air is pulled out. The velocity magnitude reaches a maximum value of 2 m/s at t = 0.023 s. At this moment, the air can freely flow through the microchannel at a maximum velocity before the water reaches its fluidic entrance. Interestingly, when the water finally enters the cavity (t = 0.039 s) the filling process happens rapidly. The average pressure achieves a maximum value in a short period and thus the water finds its way out of the channel. In contrast to the other microchannels, the velocity magnitude decreases abruptly before the microchannel H3 is filled. Although the filling process occurs rapidly until the channel is filled to an 88% (t = 0.05 s), the complete filling process for this microchannel takes longer. The channel H3 is totally filled after 0.07 s. In sum, the increase in pressure across the microchannel H3 contributed to enhancing the filling process, but as soon as the pressure was stabilized, it took longer to fill the remaining air volume inside the microchannel completely. Thereafter, the pressure difference along the microchannels was maintained to a maximum level so that water could continuously flow at an average velocity magnitude. In practical terms, filling of the three microchannels occurred almost at the same time until the pressure drop along the channels was

equalized. Alternatively, Fig. 2–22 displays the filling process by introducing water laterally across the interface.

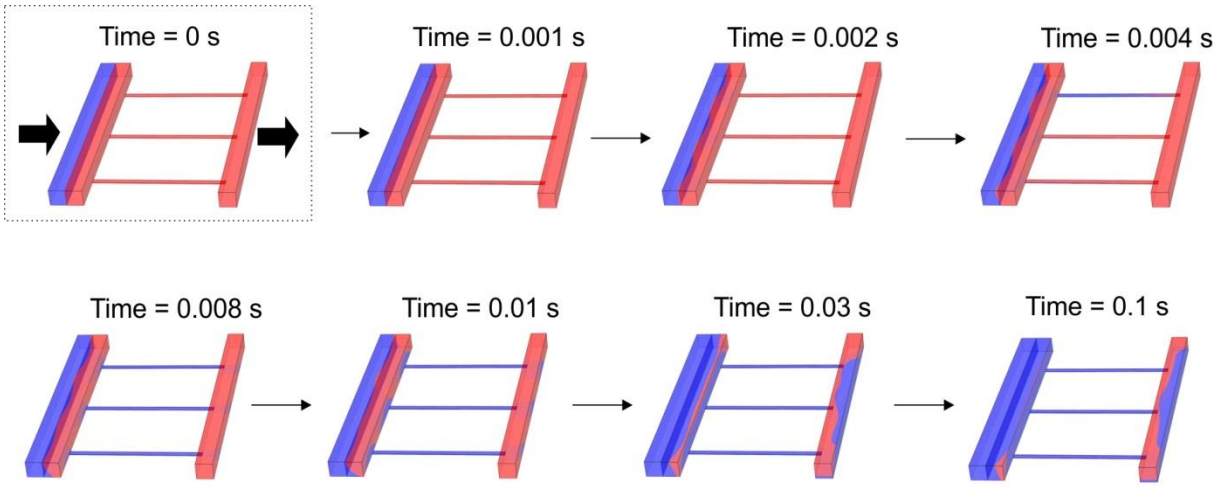

Fig. 2–22. The graphs show the evolution of the volume of fraction of water while it is being distributed throughout the microfluidic interface using an in-line filling configuration. In this case, water is pumped into the configuration through a lateral sidewall of the left bypass microchannel at a constant flow rate of 20 µL/min. Remarkably, the filling process of the array of microchannels occurs more rapidly than in the previous 3D fluidic configuration, and also the water domain replaces most of the air spaces.

The results from the 2D simulation approach provided a rough approximation of the filling process of the microchannels, as depicted in Fig. 2–23. The accuracy of this method could be enhanced by incrementing the size of the mesh elements throughout the surface geometry. In this way, the results of the time-dependent study for the average velocity and pressure profiles can display a smoother behavior and tendency across the microchannels. In general, the filling process demonstrated to be quite similar for the 2D and 3D schemes; in both cases, filling of the microchannels was completed within 0.7 s. However, the computed values for the 3D configuration showed a higher degree of accuracy which complied well with the real dimensions of the microchannels. For example, filling of the individual channels was easily monitored by tracking the changes in the velocity profile. In other words, if the aim of the FEM simulation is to study the flow dynamics of complex geometries, a 2D analysis is suitable to provide a good estimation of the filling process. On the other hand, if a high degree of certainty is required to obtained solid fluidic parameters for the pressure difference and velocity profile, a 3D configuration must be implemented. Regarding computational times and resources, resolving complex and three-dimensional geometries in Comsol is quite time-consuming. A trade-off must be considered for the accuracy of the results and the time needed to learn, optimize, resolve and select the adequate solving method for the specific study. For instance, the computational time required to solve the 3D simulations in this Thesis was 24 times higher than for 2D ones.

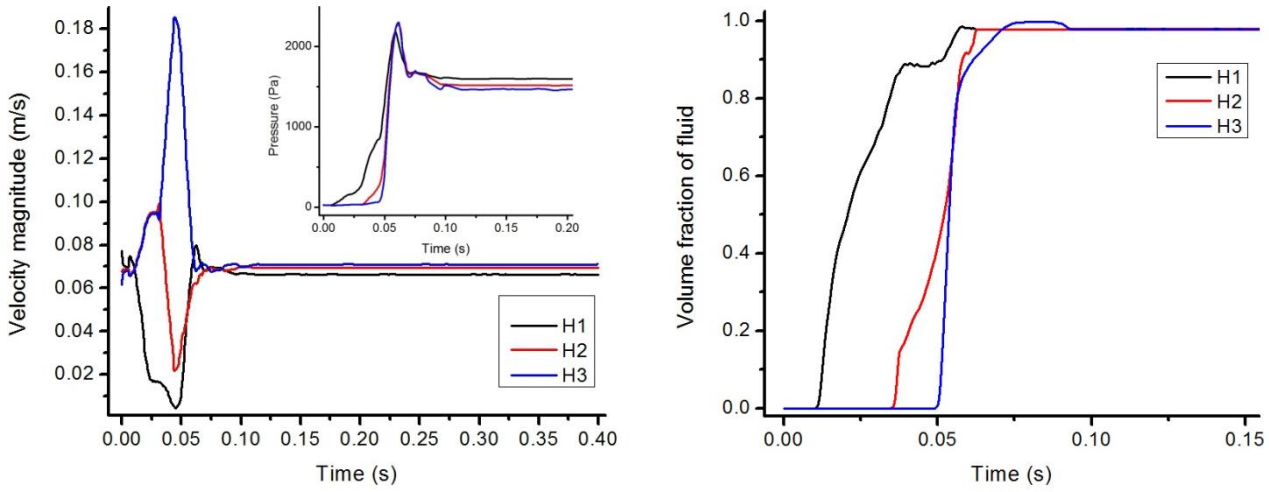

a) b)

Fig. 2–23. The filling process for the 2D microfluidic configuration roughly indicates an initial variation on the average magnitudes of velocity and pressure when waters enters in the microchannels: a) a maximum magnitude of pressure is achieved just right before the filling process is completed and b) the volume fraction of water indicates that the filling of the microchannels almost occurs simultaneously, but it strongly depends on the position of the microchannels along the bypass channels.

2.4.4.4 Comparison of filling schemes: in-line and H-shaped

This last section presents an overview of the in-line and H-shaped configuration schemes using FEM simulations. In this case, a 3D stationary analysis for each configuration is performed in Comsol to predict the flow dynamics once the microchannels are totally filled. The results demonstrate that the transporting of water through the microchannels using a direct in-line configuration is independent of the output settings, see Fig. 2–24. The waste bypass channel at the outlet of the microchannels can either be interconnected or solely linked to the waste reservoir without affecting the flow dynamics. Furthermore, the stationary analysis of the water motion inside the microchannels indicates that the velocity and pressure magnitudes of the three microchannels are very similar and closely interrelated. When all the microchannels are filled, both the average velocity and pressure difference linearly increase as a function of the inlet flow rate. Henceforth, if the application requires higher velocity profiles inside the microchannels, this filling configuration can be useful. Notably, if the number of microchannels is augmented, the maximum depicted magnitudes of velocity and pressure will correspondingly decrement, but the time to gain complete fluid exchange inside the microchannels will be reduced.

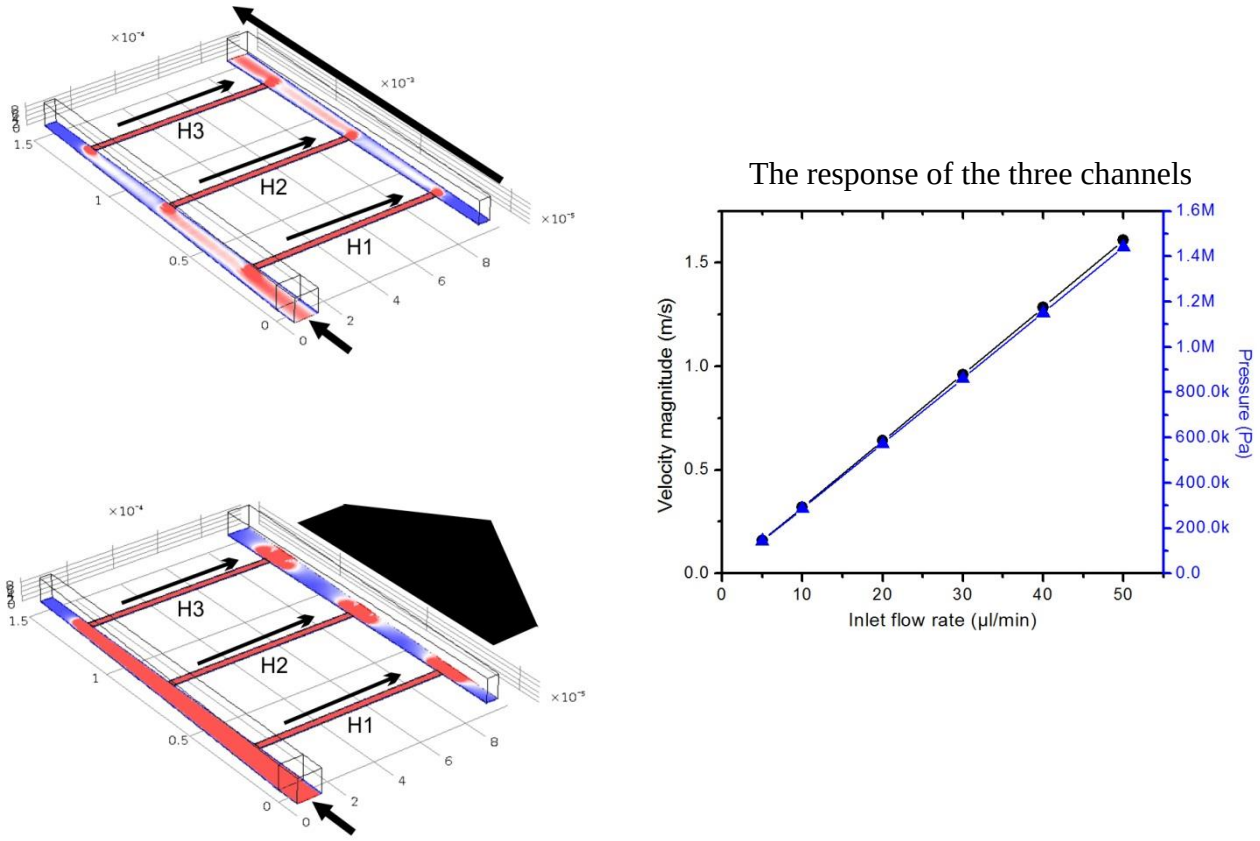

Fig. 2–24. A stationary study of a 3D microfluidic configuration in which the motion of water is based on an in-line approach confirms that the flow dynamics is independent of the outlet configuration of the fluidic network. Also, a direct interplay between the inlet flow rate and both the velocity magnitude and pressure profile is exhibited for the three microchannels.

As follows, using H-shaped filling configuration, both the velocity magnitude and pressure difference maintain a direct relationship with the applied inlet flow rates as can be seen in Fig. 2–25. However, the pressure and velocity decay is of three orders of magnitude with respect to the in-line fluidic configuration. Notably, the majority of water volume is transported through the main bypass channels, and solely a small fraction of the liquid is conducted through the array of microchannels. Particularly, the velocity and pressure magnitudes inside the microchannel H3 are more affected than the other microchannels. This can be explained because the pressure of the main inlet bypass channel proportionally decays along its longitudinal axis. Moreover, if the embedded microchannels are distributed more separately, this behavior will become more pronounced, and the velocity and pressure magnitude will gradually decrement for each microchannel as a function of their position along the bypass channel. Hence, if the microchannels are closely spread, their fluidic parameters will not notably differ, and the filling process can be simultaneous.

The final H-shaped single input/double output filling configuration partially modifies the previous approach by reducing the dimensions of the first bypass channel. As shown in

Fig. 2–26, the width of the channel is reduced by half for every fluidic entrance of the array of microchannels. As a consequence, the fluidic resistance along the bypass channels will increase and thus the expected pressure drop will be less. The stationary study of this configuration confirms the direct interplay of the inlet flow rate for values of up to 100 µL/min. By using this scheme, the pressure and velocity decay is one order of magnitude higher than the previous H-shaped single input/ double output configuration. Also, the flow dynamics for every microchannel have fewer differences by maintaining more stable values of pressure and velocity field despite their position along the main bypass channel.

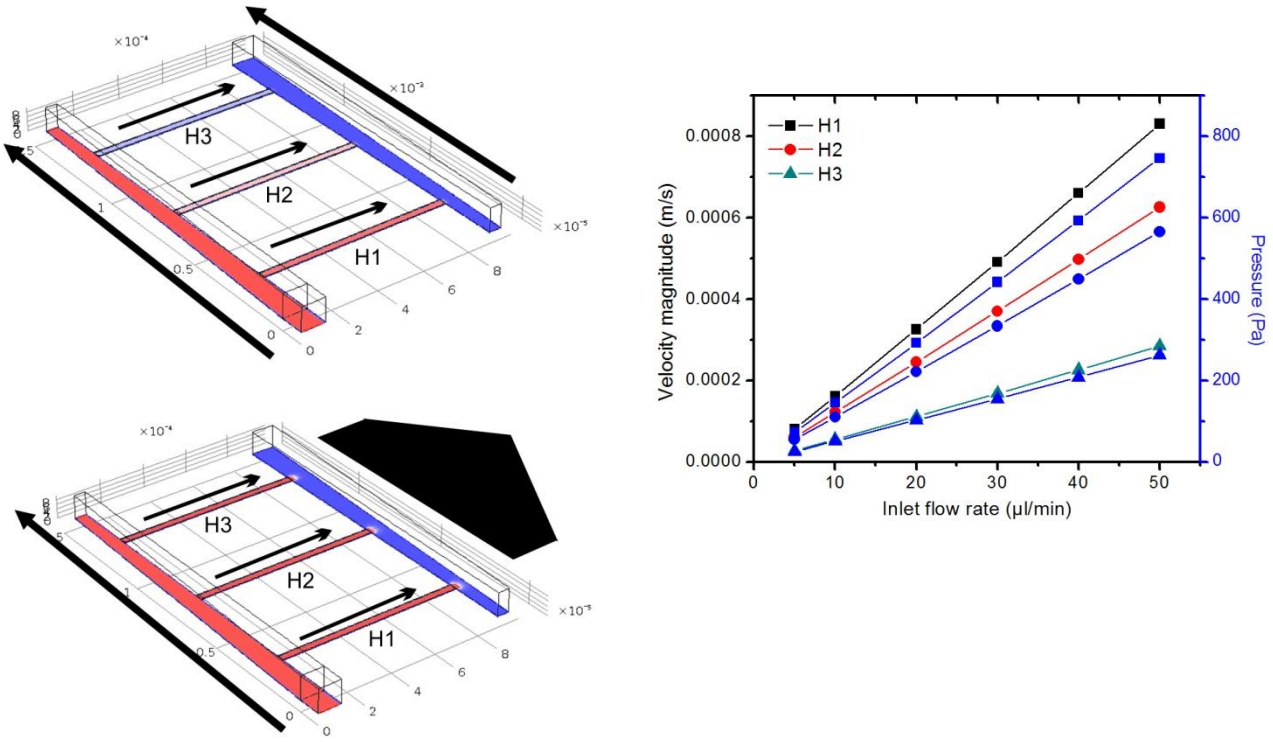

Fig. 2–25. A stationary study reveals that the velocity and pressure profiles when water is transported using an H-shaped microfluidic configuration depends on the distribution and location of the microchannels. In this case, the microchannel H3 will exhibit the lowest pressure profile. Also, in this approach, the outlet configuration of the right bypass channel does not affect the dynamics of water towards the waste reservoir.

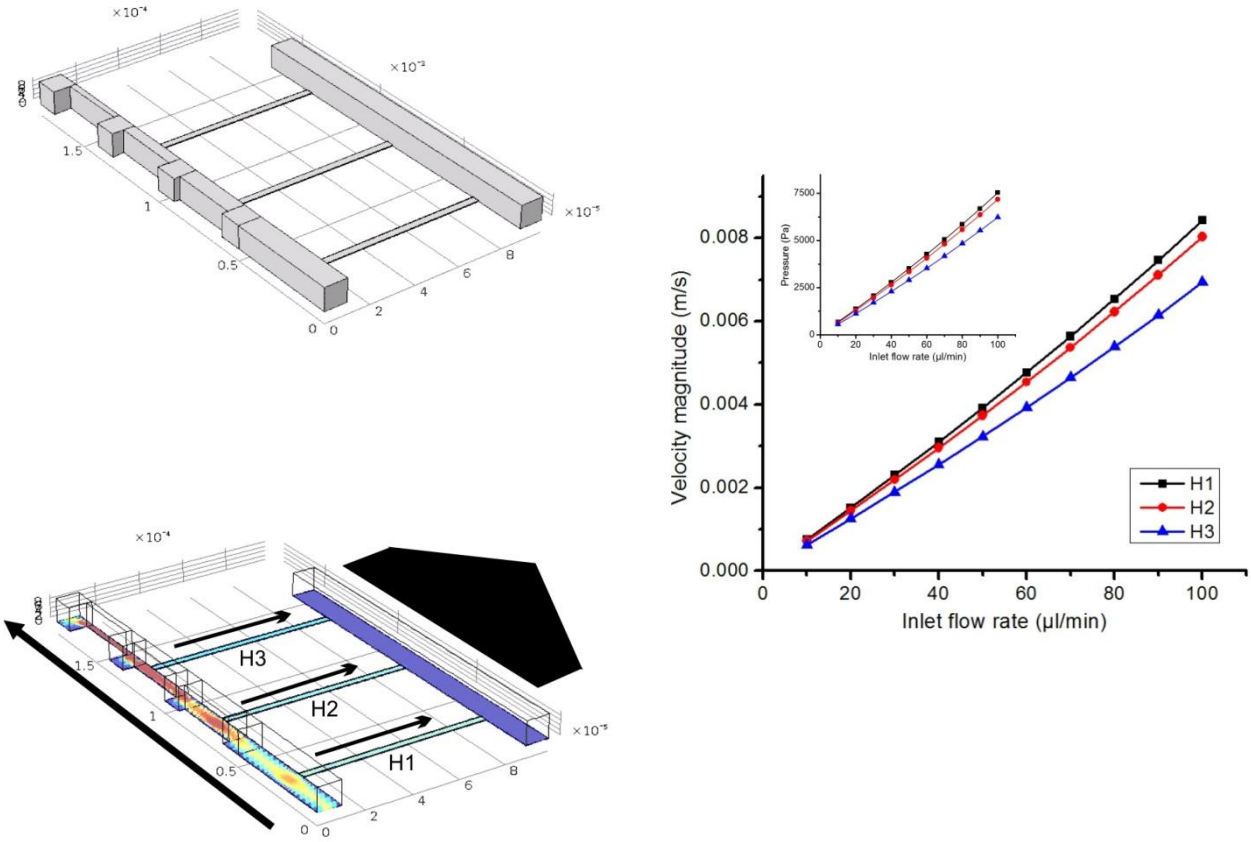

Fig. 2–26. An alternative 3D scheme for an H-shaped microfluidic configuration demonstrates that the decay in both the pressure and velocity magnitudes can be compensated by reducing the dimensions of the inlet bypass channel.

2.5 General conclusions about the design of the HMB devices

In this section, a summary of the principal criteria considered for the design of the HMB devices is presented. FEM simulations aimed to elucidate not only the expected mechanical behaviour of the microstructures but also the interplay of various parameters involved in their frequency response, elastic constant and mass responsivity according to the materials and dimensions established. The investigation also encompassed the evaluation through FEM simulations of the two fluid filling approximations employed to exchange fluids inside the embedded microchannels. The most significant findings of the design of the HMB devices are described below:

- The topology of the HMB devices is chosen to protrude out from the based substrate employing surface micromachining to constitute a three-layer-sandwich structure wherein the sacrificial layer is confined in between two structural layers. This approach tries to skip the usage of CMP equipment since this planarization procedure is not available at the clean room facilities. Instead, the HMB devices will be constituted by a layer-by-layer coating microfabrication strategy.

- For the microfabrication of the HMB devices, silicon nitride and polycrystalline silicon are considered as structural materials because of their excellent mechanical properties and availability. Arrays of HMB devices made of silicon nitride with narrow and profound microchannel dimensions, and short separation distances will exhibit resonance frequencies from 950 to 1100 KHz. The theoretical mass responsivity expected for these devices will be in the range of 15 to 18 Hz/pg. HMB devices made of polycrystalline silicon with the same dimensions will have a frequency response from 900 to 1050 KHz with a mass responsivity range between 18 to 21 Hz/pg. Hence, better resonant frequency responses and higher sensitivities will be displayed for devices with shorter effective length (tilt angles of 7°), short widths (10 µm) and large depths (4 µm).

- The elastic constant of either configuration of arrays of HMB devices will be in the range of 2420 N/m to 3500 N/m. Particularly, short resonators with large widths will have higher stiffness.

- The ratio of mass per unit length of the fluid to the mass per unit length of the resonator structure should be minimized (A_s/A_f) to maximize the shift on the resonance frequency response of the HMB devices with respect to fluid density change of the sample solution. Therefore, microchannel depths of up to 4 µm are proposed with sidewall thickness of up to 1 µm regarding the dimensions that can be reproduced during the microfabrication of the sensor.

- The mechanical motion of the HMB devices will be limited by the doubly clamped configuration of the resonators. As a result, the expected dynamic range for the HMB

resonators will be at least an order of magnitude smaller than those devices that use cantilever resonators.

- Regarding the governing microfluidics of the HMB devices, the hydrostatic pressure will proportionally decay as the number of microchannels increases. For instance, the pressure of a set of HMB devices with four microchannels can decrease about 80% with respect to a single microchannel.

- The expected flow rates inside the microfluidic channels depend directly on the dimensions of the microchannel itself. Considering a constant pressure of 1 mbar, the expected flow rate for thin microchannels with larger depths is in the range of µL/s. The calculated Reynolds number (~ 0.00119) with FEM simulations guarantees a laminar inflow inside each microchannel.

- The proposed design of the HMB resonators will operate in the low-inertia regime based on the frequency response ($f_0 \leq 900$ KHZ) and maximum height for the microchannels ($h_f = 4$ µm). By tracking the quality factor of the HMB resonators while streaming different liquid samples, the sensor will respond to viscosity changes. Moreover, the contribution of the fluid shear effect in the dissipation of energy in our devices can be ignored given that the shear-limited Q-factor ($\sim 4 \times 10^5$) is four orders of magnitude higher than the expected Q-factor of the HMB devices (up to 600).

- The FEM evaluation of the in-line and H-shaped configuration showed good results for the efficient transport of water inside the microcavities. Rapid exchange of samples is guaranteed with the H-shaped configuration but at low-velocities. Higher pressure differences are observed in the in-line configuration, and therefore, more stable fluid flows will be observed.

- Regarding the mechanical performance of the HMB devices made of polysilicon, the fluid structure interaction analysis confirms that the expected deformation of the sidewalls of the microchannels can withstand the range of flow rates normally employed for bioanalytical applications (0.1 µL/min - 10 µL/min). The evaluated von Mises stress was forth orders of magnitude lower than the typical fracture stress of the structural material. This implies that a direct in-line configuration for filling the inner cavities can be directly employed.

References

[1] L. D. Landau, L. P. Pitaevskii, A. M. Kosevich, and E. M. Lifshitz, *Theory of Elasticity, Third Edition: Volume 7*, 3 edition. Oxford England; Burlington, MA: Butterworth-Heinemann, 1986.

[2] N. Lobontiu, *Mechanical design of microresonators: modeling and applications*. McGraw-Hill, 2006.

[3] T. P. Burg, M. Godin, S. M. Knudsen, W. Shen, G. Carlson, J. S. Foster, K. Babcock, and S. R. Manalis, 'Weighing of biomolecules, single cells and single nanoparticles in fluid', *Nature*, vol. 446, no. 7139, pp. 1066–1069, 2007.

[4] O. Brand, I. Dufour, S. Heinrich, et al, *Resonant MEMS: Fundamentals, Implementation, and Application*, 1 edition. Weinheim: Wiley-VCH, 2015.

[5] T. P. Burg, A. R. Mirza, N. Milovic, C. H. Tsau, G. A. Popescu, J. S. Foster, and S. R. Manalis, 'Vacuum-Packaged Suspended Microchannel Resonant Mass Sensor for Biomolecular Detection', *J. Microelectromechanical Syst.*, vol. 15, no. 6, pp. 1466–1476, 2006.

[6] T. P. Burg, J. E. Sader, and S. R. Manalis, 'Nonmonotonic Energy Dissipation in Microfluidic Resonators', *Phys. Rev. Lett.*, vol. 102, no. 22, p. 228103, 2009.

[7] J. E. Sader, T. P. Burg, and S. R. Manalis, 'Energy Dissipation in Microfluidic Beam Resonators', *J. Fluid Mech.*, vol. 650, pp. 215–250, 2010.

[8] K. R. Williams, K. Gupta, and M. Wasilik, 'Etch rates for micromachining processing-Part II', *J. Microelectromechanical Syst.*, vol. 12, no. 6, pp. 761–778, 2003.

[9] J. L. Arlett and M. L. Roukes, 'Ultimate and practical limits of fluid-based mass detection with suspended microchannel resonators', *J. Appl. Phys.*, vol. 108, no. 8, pp. 084701–084701–11, 2010.

[10] J. P. Cleveland, S. Manne, D. Bocek, and P. K. Hansma, 'A nondestructive method for determining the spring constant of cantilevers for scanning force microscopy', *Rev. Sci. Instrum.*, vol. 64, no. 2, pp. 403–405, 1993.

[11] Hugh O. Pierson, '*Handbook of chemical vapour deposition (CVD), principles, technology, and applications*, 1993.

[12] S. D. Senturia, *Microsystem Design*. Springer US, 2005.

[13] K. W. Oh, K. Lee, B. Ahn, and E. P. Furlani, 'Design of pressure-driven microfluidic networks using electric circuit analogy', *Lab. Chip*, vol. 12, no. 3, pp. 515–545, 2012.

[14] A. Folch, *Introduction to BioMEMS*. CRC Press, 2012.

[15] 'What is Von Mises Stress ?. Available: http://www.learnengineering.org/2012/12/what-is-von-mises-stress.html [Accessed: 17-Apr-2016]. .

[16] H. Kapels, R. Aigner, and J. Binder, 'Fracture strength and fatigue of polysilicon determined by a novel thermal actuator [MEMS]', *IEEE Trans. Electron Devices*, vol. 47, no. 7, pp. 1522–

1528, 2000.

[17] E. Olsson and G. Kreiss, ‘A conservative level set method for two phase flow’, *J. Comput. Phys.*, vol. 210, no. 1, pp. 225–246, 2005.

[18] H. Song, Y. Wang, and K. Pant, ‘System-level simulation of liquid filling in microfluidic chips’, *Biomicrofluidics*, vol. 5, no. 2, p. 024107, 2011.

[19] ‘Capillary Filling - Phase Field Method’. [Online]. Available: https://www.comsol.es/model/capillary-filling-phase-field-method-1878. [Accessed: 17-Apr-2016].

[20] ‘Improving convergence in nonlinear time dependent models - 1127 - Knowledge Base’. [Online]. Available: https://www.comsol.es/support/knowledgebase/1127/. [Accessed: 13-Apr-2016].

[21] ‘Droplet Breakup in a T-junction’. [Online]. Available: https://www.comsol.es/model/droplet-breakup-in-a-t-junction-1994. [Accessed: 13-Apr-2016].

[22] ‘Manually setup the geometric multigrid solver - 1213 - Knowledge Base’. [Online]. Available: https://www.comsol.es/support/knowledgebase/1213/. [Accessed: 13-Apr-2016].